CHALMERS
UNIVERSITY OF TECHNOLOGY

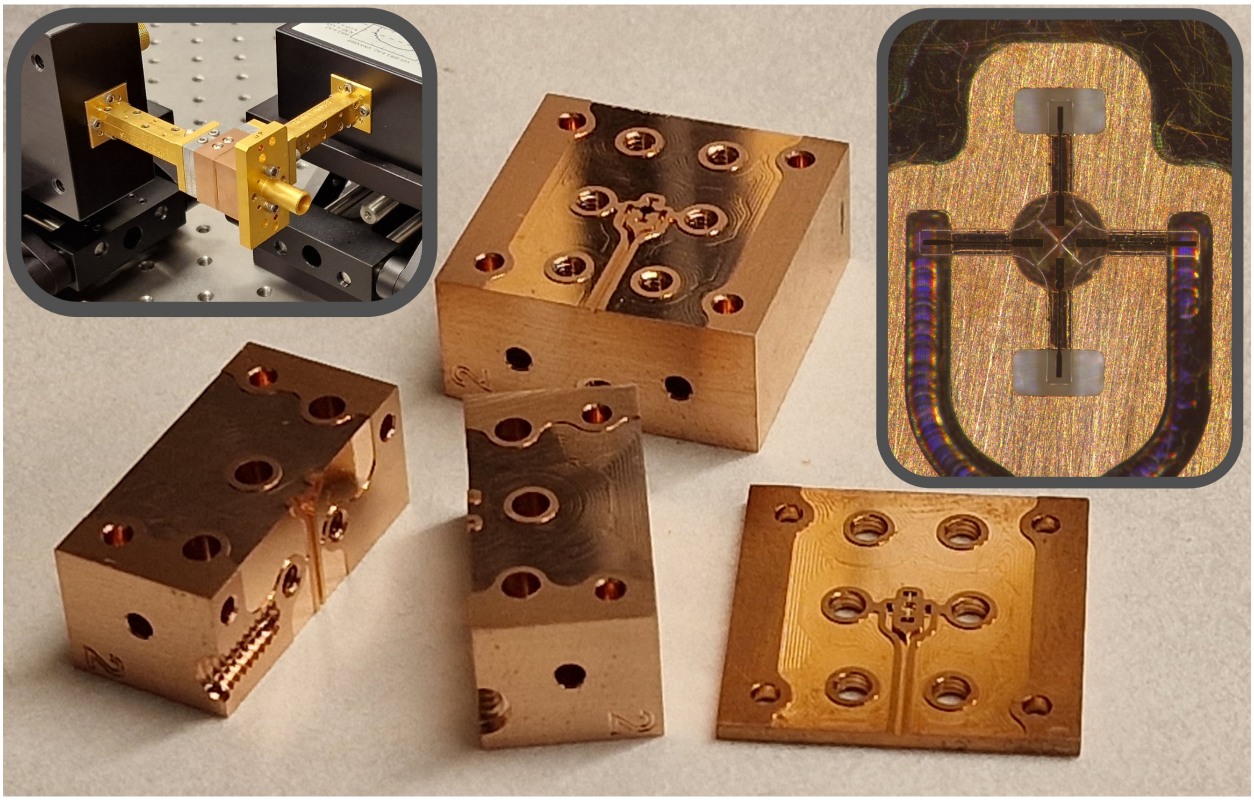

Novel orthomode transducer for millimeter wave and terahertz frequencies

Design, fabrication and characterization of novel probe-based orthomode transducer

Master's thesis in Wireless, Photonics and Space Engineering

NILS PATRIKSSON

Space, earth and environment
CHALMERS UNIVERSITY OF TECHNOLOGY
Gothenburg, Sweden 2023
www.chalmers.se

Master's thesis 2023

Novel orthomode transducer for millimeter wave and terahertz frequencies

Design, fabrication and characterization of novel probe-based orthomode transducer

NILS PATRIKSSON

Department of Space, earth and environment
Division of Onsala Space Observatory
Group for Advanced Receiver Development (GARD)
Chalmers University of Technology
Gothenburg, Sweden 2023

Novel orthomode transducer for millimeter wave and terahertz frequencies
Design, fabrication and characterization of novel probe-based orthomode transducer
NILS PATRIKSSON

© NILS PATRIKSSON, 2023.

Supervisor: Dr. Denis Meledin, Department of Space, earth and environment
Examiner: Prof. Victor Belitsky, Department of Space, earth and environment

Master's Thesis 2023
Department of Space, earth and environment
Division of Onsala Space Observatory
Group for Advanced Receiver Development (GARD)
Chalmers University of Technology
SE-412 96 Gothenburg
Telephone +46 31 772 1000

Cover: Picture of one of the produced orthomode transducers in this thesis and an example of characterization of the device.

Typeset in LaTeX
Printed by Svenskt Tryck
Gothenburg, Sweden 2023

Novel orthomode transducer for millimeter wave and terahertz frequencies
Design, fabrication and characterization of novel probe-based orthomode transducer
NILS PATRIKSSON
Department of Space, earth and environment
Chalmers University of Technology

Abstract

There exist a vast number of orthomode transducer designs for microwave frequencies. At sub-millimeter wave frequencies however, high accuracy requirements are set on the manufacturing techniques. This work seeks to design a novel orthomode transducer combining different manufacturing techniques resulting in low loss, wide bandwidth and a compact design. These are all important parameters for radio-astronomy applications.

Several design ideas from literature are considered. Room for improvement is identified and the novel design is developed using an electromagnetic full-wave solver. Fabrication of two demonstrator devices is done using CNC milling and micro-fabrication in a clean-room environment. Lastly, the demonstrators are characterized.

In summary, an orthomode transducer working between $270 - 385\,\mathrm{GHz}$ (36% fractional bandwidth) was demonstrated. The produced devices work as proof of concept with insertion loss of 2 dB and return loss of 15 dB achieved for both polarizations symmetrically at room temperature. It is concluded that insertion loss of less than 1 dB and return loss of more than 20 dB are possible to achieve with further improvements of the design. The design is in theory scale-able to 1 THz and could be used instead of quasi-optical polarization diplexers. The design is also very compact.

Keywords: orthomode transducer, terahertz, millimeter wave, sub-millimeter wave, orthomode junction, polarization diplexer, polarimetry

Acknowledgements

This project would not have been possible without the help, support, discussions and friendliness of many people. Firstly, I am grateful to my supervisor Dr Denis Meledin for his outstanding help and enthusiasm in every aspect of the project. Secondly, I appreciate my examiner Prof Victor Belitsky for his great ideas, suggestions and feedback throughout the process. Thirdly, I thank Prof Vincent Desmaris for his fruitful discussions, feedback and motivation. Additionally, I want to acknowledge the help from Leif Helldner, Sven-Erik Ferm, Dr Alexey Pavolotskiy, Cristian Daniel López and Igor Lapkin during the design and fabrication of the device. Finally, I want to thank all the people at GARD, previously mentioned but also Magnus Strandberg, Mathias Fredrixon, Erik Sundin and Mohamed Aniss Mebarki for making me feel welcome and creating a friendly work environment.

Nils Patriksson, Gothenburg, June 21, 2023

List of Acronyms

Below is the list of acronyms that have been used throughout this thesis listed in alphabetical order:

ADS	Advanced simulation software, referring to Keysight ADS [1]
CWG	Circular waveguide
FBW	Fractional bandwidth
FEM	Finite element method
HFSS	High frequency simulation software, referring to Ansys HFSS [2]
LP	Longitudinal probe
OMJ	Orthomode junction
OMT	Orthomode transducer
RWG	Rectangular waveguide
TE	Transversal electric
TM	Transversal magnetic
TP	Transversal probe
VNA	Vector network analyser

Contents

1

Introduction

Radio astronomy is a sub-field of astronomy that studies celestial objects at radio frequencies, which are frequencies in the order of terahertz and lower. Ground based radio astronomy makes use of Earths atmosphere's transparency to radio waves which means space can be observed from Earth. In recent years, observatories operating in the millimeter-wave and terahertz frequency range have been built, out of some examples are the Atacama Large Millimeter/sub-millimeter Array (ALMA) [3], the Atacama Pathfinder Experiment (APEX) [4] and the Sub-millimeter Array (SMA) [5], all situated at high altitude deserts to minimize atmospheric absorption from water vapor. Scientific results applying data from these telescopes contribute to our understanding of phenomena such as galaxy [6], star [7] and planet formation [8]. The telescopes have also contributed to understanding objects in our own solar system, ranging from comets, asteroids, moons and planets [9]. A scientific achievement receiving a lot of media attention in 2019 was the first image of a black hole. The imaging of black holes is another application where millimeter-wave radio telescopes such as ALMA and SMA has been used as parts of the Event Horizon Telescope [10].

For millimeter-wave radio telescopes, dual polarization receiver systems are preferred. Simply put, all signals which are observed have some polarization and can be described by two polarization components. A dual polarization receiver detects both these components. Some celestial objects or processes emit radiation where the relative proportions of the two components of the polarization convey information. An example of such a process is synchrotron radiation where charged particles radiate while under the influence of magnetic fields [11]. By measuring the polarization properties of the received radiation new conclusions can therefore be drawn about the observed objects. For instance, polarization sensitive receivers were used to measure the galactic magnetic field in [12], [13]. For observations where proportions of the two polarization components give no information about the observed object dual polarized receivers are still preferred. Some processes such as molecular transitions, radiate with no correlation between the two polarization components [11], called unpolarized. The sensitivity when observing such a source is increased by $\sqrt{2}$ for a dual polarization receiver [14]. This motivates the use of these kind of receivers also for unpolarized sources.

There exist numerous technical solutions to observe both polarization components. The ALMA observatory, which operates at frequencies between $84 - 950\,\mathrm{GHz}$ with eight different receivers [3], is an example of an observatory where two different solutions are used for different frequency bands. Some of the higher frequency bands such as band 7 ($275 - 373\,\mathrm{GHz}$), 9 ($602 - 720\,\mathrm{GHz}$) and 10 ($787 - 950\,\mathrm{GHz}$) use two single polarization horn antennas placed after grids which only let through one polarization component per horn [15]–[17]. Some of the lower frequency receivers, specifically band 3 ($83 - 116\,\mathrm{GHz}$), 4 ($125 - 169\,\mathrm{GHz}$), 5 ($163 - 211\,\mathrm{GHz}$), 6 ($211 - 275\,\mathrm{GHz}$) and 8 ($385 - 500\,\mathrm{GHz}$), use one dual polarization horn antenna and separate the polarization components using an orthomode transducer [18]–[22]. When using only one horn antenna for both polarizations, alignment of the two polarization views of the sky (called beam squint) is simpler [23] which motivates the use of orthomode transducers also for higher frequencies.

Orthomode transducers generally make use of complex geometries to separate the two polarization components if wide-band performance is needed, exemplified by the Bøifot design in [24]–[27], the turnstile design in [28]–[30] and the reverse-coupling design in [31], [32]. Generally, the size of orthomode transducers are proportional to wavelength, meaning, at terahertz frequencies the size of the complex geometry is very small. Fabrication techniques such as CNC milling, commonly used for microwave components, is limited in linear accuracy to some µm. Furthermore, assembly of waveguide components needs to be very accurately done, in some cases in the order of some µm to have acceptable performance [26], [32]. This thesis seeks to combine CNC milling with micro-fabrication techniques commonly used to fabricate integrated circuits at high accuracy. Micro-fabrication has been utilized for finline designs [33], [34] and planar orthomode transducers [35]–[38]. Substrate-based designs can however suffer from extensive losses at millimeter wave and terahertz frequencies. By combining these two manufacturing techniques it could be possible to relax the requirements of CNC milling but still achieve low loss which is an advantage of using waveguide based orthomode transducers.

1.1 Aim of thesis

The aim of this thesis is to investigate design alternatives, design, manufacture and characterize a novel orthomode transducer for use in a radio astronomy receiver system. The design should utilize advantages of both waveguide based solutions and substrate-based as described previously. The frequency band corresponding to ALMA band 7 ($275 - 373\,\mathrm{GHz}$) was chosen for the demonstration of the orthomode transducer which set some design specifications.

The sensitivity of a radio-astronomy receiver is critical, and all components of the system need to minimize their negative influence on sensitivity. The orthomode transducer affect sensitivity mainly by its loss. Because it is a component placed before amplifiers in the receiver chain, its loss is additionally important as described by Friis formula [39]. The insertion loss of the orthomode transducer for ALMA band 8 is about $-1.5\,\mathrm{dB}$ at room temperature and predicted to be $0.4 - 0.5\,\mathrm{dB}$ at temperature of $4\,\mathrm{K}$ [27]. A room temperature insertion loss of lower than $0.5\,\mathrm{dB}$ would therefore be a major improvement.

Another important characteristic of the orthomode transducer is the leakage between the two polarization components, called cross-polarization. This metric will evidently from the previous sections affect polarization sensitive measurements where the proportions between polarizations need to be measured accurately. In [27] a requirement for the cross-polarization is set to $-23\,\mathrm{dB}$, and in this thesis something similar is set, namely, $-25\,\mathrm{dB}$. Another measure is the reflected energy at the inputs and outputs of the orthomode transducer, quantified by return loss. Often a specification of return loss below $-20\,\mathrm{dB}$ is used [27], which is also the aim for the orthomode transducer in this thesis.

1.2 Structure of thesis

The basic working principles of orthomode transducers is reviewed in the theory chapter (chapter 2), after which a study of different design alternatives is carried out (section 2.3.3). The theoretical feasibility of the novel design idea is investigated in section 2.4 and there is also a review of material parameters, because to design the substrate-based components, the permittivity was characterized.

The methods of design, production and characterization is described in the method chapter (chapter 3). The design was carried out in steps, firstly designing the different parts of the orthomode transducer and later combining the parts. The combined orthomode transducer was later changed to fit the measured material parameters of the substrate material. The material parameter measurements are described in section 3.3 after which both production with CNC milling and micro-fabrication are described in section 3.4. Lastly, methods of characterization are motivated and described in section 3.5.

Results from the design phase, material properties measurements and measurement of produced orthomode transducers is presented in the results chapter (chapter 4). Discussion of these results is included in the same chapter. Lastly, conclusions and recommendations for future work is done in chapter 5.

2

Theory

This chapter describes the fundamentals of electromagnetic wave propagation and microwave network analysis, two topics essential to the understanding of orthomode transducers. Also, there is a literature review of design alternatives for orthomode transducers and a theoretical evaluation of the novel design presented in this thesis.

2.1 Fundamentals of electromagnetic wave propagation

Electromagnetic wave propagation is described by Maxwell's equations, which is a set of coupled differential equations. The solutions to these equations are electrical vector-fields and magnetic vector-fields. In every point of space, the electric and magnetic fields are both vectors pointing in some direction. The electric and magnetic fields are also time-dependent, which means all vectors in space can change direction and amplitude during time. This enables waves to propagate. The theory presented in this section is also presented in [40]. A thorough background of electromagnetic field theory can be found in textbooks such as [39]–[41].

2.1.1 Free space propagation and polarization

Free space propagation is electromagnetic wave propagation in some vacuum-like media with no electric charges or currents present. By solving Maxwell's equations in this media, it's possible to show that waves can propagate.

A common mathematical description of the field is by phasor notation. For a plane wave propagating in $\hat{z}$ direction at position (x, y, z) the E-field can be described in phasor notation as,

$$\bar{E}(z,t) = (\hat{x}A_+ + \hat{y}B_+)e^{j\omega t - jkz} \text{ [40].} \tag{2.1}$$

A_+ and B_+ complex amplitude constants, ω angular frequency of the wave, k the wave number, z the position in space and t time. The polarization of this wave is defined by the direction of the E-field. For example with $A_+ = 0$ and $B_+ = 1$ we have

$$\vec{E}(z,t) = \Re\{\hat{y}B_+e^{j\omega t - jkz}\} = \hat{y}\cos(\omega t - kz) \tag{2.2}$$

which means the E-field direction is always in $\hat{y}$ or $-\hat{y}$ direction. This is called linear polarization because the E-field is always directed in a line. An example of

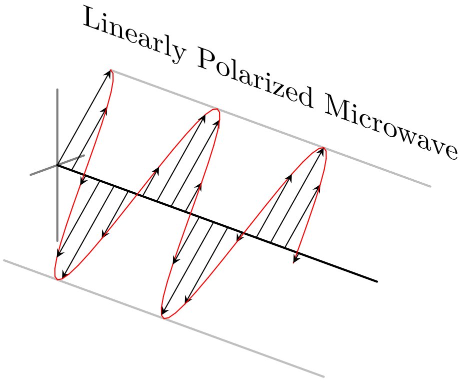

Figure 2.1: Illustration of linearly polarized wave. With time, vectors will point in the same direction or opposite direction.

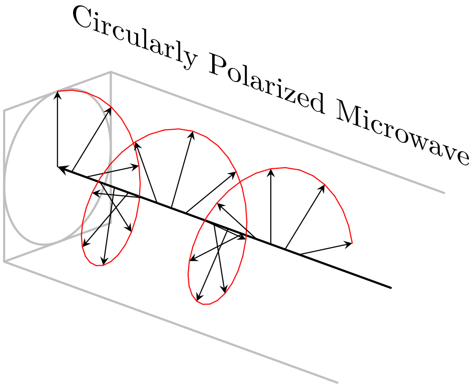

Figure 2.2: Illustration of circularly polarized wave. With time vectors will rotate around the axis of propagation.

linearly polarized wave is shown in figure 2.1. It is also possible to have elliptically or circularly polarized plane waves which would mean that the E-field rotates, either elliptically or circularly, around the axis of propagation. An example of a circularly polarized wave is when $A_+ = -j$ and $B_+ = 1$ which would mean that the E-field is

$$\vec{E}(z,t) = \Re\{(-j\hat{x} + \hat{y})e^{j\omega t - jkz}\} = \hat{x}\sin(\omega t - kz) + \hat{y}\cos(\omega t - kz) \text{ [40].} \tag{2.3}$$

An illustration of a circularly polarized wave is shown in figure 2.2. An important property of elliptically or circularly polarized waves are that they can be described as a sum of to linearly polarized waves. In equation 2.3 this can be seen, when the E-field vector is a sum of a $\hat{x}$ and $\hat{y}$ component.

2.1.2 Waveguides

Free space waves coming from an observable object can, using an antenna, be transferred into a waveguide or some other guiding structure. By solving Maxwell's equations with boundary conditions according to the geometrical dimensions of the guiding structure it is possible to show that the field solution is a sum of field solutions [39]. These particular solutions are called modes.

There are a wide range of guiding structures such as coaxial lines, slotlines, striplines, microstrip lines, and waveguides of different shapes, such as circular, rectangular and square [39]. At millimeter-wave frequencies, waveguides are often preferred, mostly because they present lower loss [39].

In a rectangular waveguide the modes are categorized into transversal electric (TE) and transversal magnetic (TM) modes. They are also given pairs of indices (m, n) where n and m are integers between $0 - \infty$ for TE modes and $1 - \infty$ for TM modes. There is an infinite number of modes, however for a certain signal, or wave, with frequency f, only some modes will propagate. This is governed by the cut-off frequency, $f_{cut(m,n)}$, given by

$$f_{cut(m,n)} = \frac{1}{2\pi\sqrt{\mu\epsilon}}\sqrt{\left(\frac{m\pi}{a}\right)^2 + \left(\frac{n\pi}{b}\right)^2}, \tag{2.4}$$

where μ and ϵ are the permeability and permittivity of the material inside the waveguide. a is the cross-sectional height dimension of the rectangular waveguide, while b is the cross-sectional width.

To illustrate this let us assume we are observing a celestial source which radiates at $f = 300\,\text{GHz}$. For our waveguide to propagate this signal, some mode needs to have a lower cut-off frequency than the signal frequency. A rectangular waveguide of size $0.76 \times 0.38\,\text{mm}$ would have the lowest cut-off for TE_{10} of $f_{cut(1,0)} = 197.2\,\text{GHz}$ which means the signal could propagate. When only one signal, or one polarization, is to be transmitted with a waveguide, it is preferred to have only one propagating mode. For the $0.76 \times 0.38\,\text{mm}$ waveguide, the next two modes start to propagate at $f_{cut(0,1)} = f_{cut(0,2)} = 394.4\,\text{GHz}$ which restricts the bandwidth of the waveguide.

The polarization of a waveguide mode is, as for the free space case, defined by the E-field phasor direction. To transmit dual polarizations in a waveguide, one mode for each polarization needs to propagate. So, if the celestial 300 GHz source is radiating a polarized signal, to receive that signal in a waveguide, a $0.76 \times 0.76\,\text{mm}$ waveguide could be used. The two polarization components would be contained in the TE_{10} and TE_{01} modes with cut-offs of $f_{cut(1,0)} = f_{cut(0,1)} = 197.2\,\text{GHz}$. These modes are plotted in figure 2.3 together with the other modes with cut-offs lower than 385 GHz.

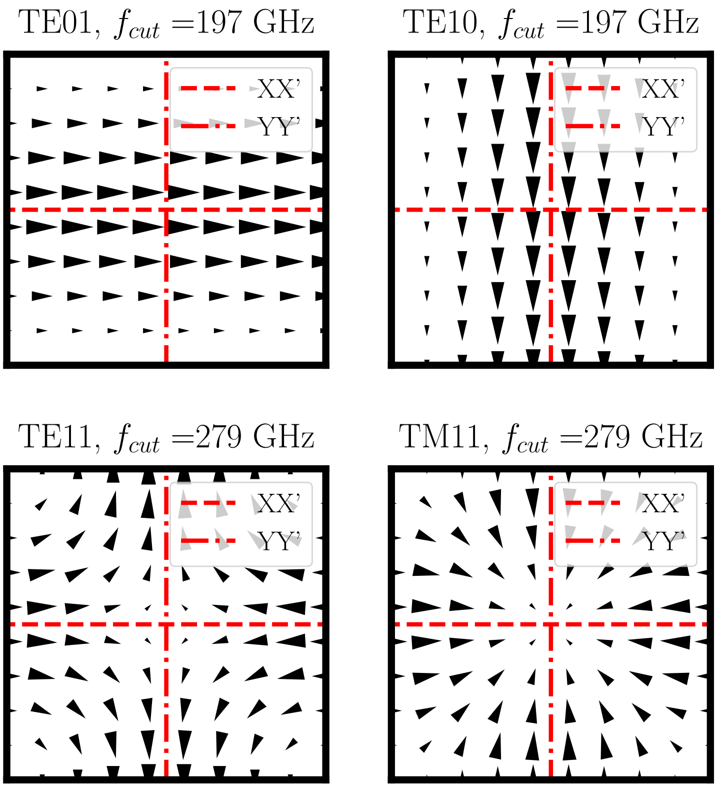

Figure 2.3: The E-field of the first four modal solutions for a quadratic waveguide of size 0.76×0.76 mm. The waveguide size a is in XX' directions and b in YY' direction.

2.2 Microwave network analysis

The purpose of an orthomode transducer (OMT) is, as described earlier, to separate the two components of polarization for a received wave. An OMT is one example of a microwave component. To analyse power flow, losses, reflected power and a component's influence on full system performance, microwave network analysis is often used [39]. In this chapter, a review of microwave network analysis is carried out, in large parts similar to the presentation done in [39].

It is possible to describe a microwave component in terms of a microwave network by assigning terminals or ports to the component's inputs and outputs [39]. A port is simply a point or plane where voltage and current are measured, and the microwave network is a model of the component. An illustration of this is shown in figure 2.4 where a four-port network is shown.

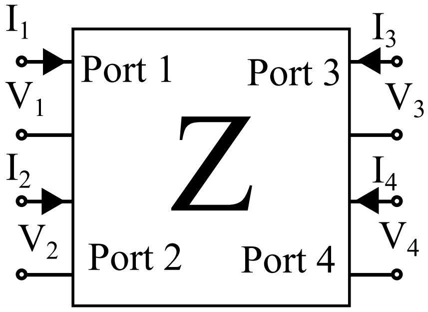

Figure 2.4: Example of a four-port microwave network.

Voltages and currents are related by an impedance matrix, in the general form of

$$\begin{bmatrix} V_1 \\ V_2 \\ \vdots \\ V_N \end{bmatrix} = \begin{bmatrix} Z_{11} & Z_{12} & \cdots & Z_{1N} \\ Z_{21} & Z_{22} & \cdots & Z_{2N} \\ \vdots & \vdots & \ddots & \vdots \\ Z_{N1} & Z_{N2} & \cdots & Z_{NN} \end{bmatrix} \begin{bmatrix} I_1 \\ I_2 \\ \vdots \\ I_N \end{bmatrix} \tag{2.5}$$

where V_N and I_N is voltage and current for port N and elements Z_{ij} are complex numbers.

At lower frequencies, direct measurements of voltages and currents are possible. At millimeter wave frequencies however, those measurements are not possible. To characterize microwave systems scattering parameters are used instead [39]. The scattering matrix relates, instead of voltages and currents, outgoing and incident voltage waves at the ports. The scattering matrix of a N-port network is generally written as,

$$\begin{bmatrix} V_1^- \\ V_2^- \\ \vdots \\ V_N^- \end{bmatrix} = \begin{bmatrix} S_{11} & S_{12} & \cdots & S_{1N} \\ S_{21} & S_{22} & \cdots & S_{2N} \\ \vdots & \vdots & \ddots & \vdots \\ S_{N1} & S_{N2} & \cdots & S_{NN} \end{bmatrix} \begin{bmatrix} V_1^+ \\ V_2^+ \\ \vdots \\ V_N^+ \end{bmatrix}. \tag{2.6}$$

where V_n^- are exiting and V_n^+ are entering voltage waves at port n. Voltage waves are related by the scattering parameters S_{ij} which are frequency-dependent complex valued.

2.2.1 Orthomode transducer scattering parameters

Even though the two polarization components can have some relationship and tell astronomers something about a celestial object [12], they can from a microwave network viewpoint be seen as two different signals [42]. As previously illustrated in equation 2.3 even a circularly polarized wave can be seen as a sum of two independent components.

The polarization components enter the orthomode transducer at the same *physical port*, i.e., the same waveguide opening. However, they enter in two different modal solutions (in other words, two different modes). For instance, in a square 0.76 × 0.76 mm waveguide they would enter through the TE_{01} and TE_{10} mode shown in figure 2.3. For each mode, there is a voltage and current, and therefore, each mode has its own port in a microwave network [39].

The orthomode transducer, which has two input modes, is therefore often represented by a four-port network with a scattering matrix,

$$\begin{bmatrix} V_1^- \\ V_2^- \\ V_3^- \\ V_4^- \end{bmatrix} = \begin{bmatrix} S_{11} & S_{12} & S_{13} & S_{14} \\ S_{21} & S_{22} & S_{23} & S_{24} \\ S_{31} & S_{32} & S_{33} & S_{34} \\ S_{41} & S_{42} & S_{43} & S_{44} \end{bmatrix} \begin{bmatrix} V_1^+ \\ V_2^+ \\ V_3^+ \\ V_4^+ \end{bmatrix}. \tag{2.7}$$

where port 1 and 2 represent the two polarization inputs, while port 3 and 4 represent the two outputs, one for each polarization. The OMT is a passive device most often made by reciprocal materials, which means transmission between two ports does not depend on the direction of propagation [43]. This means $S_{ij} = S_{ji}$ in the scattering matrix (this is also valid for other passive components with reciprocal materials, such as most combiners, waveguides [43]).

Analysing power reflected, dissipated and transmitted at or between ports of the network is easily done once the scattering parameters of the orthomode transducer is known. The main performance measures for the orthomode transducer are, return loss (RL), insertion loss (IL), cross-polarization (X-pol) and isolation (Iso). Return loss is the power lost for a reflected signal and at port n calculated through,

$$RL = |S_{nn}|^{-2} = -20 \log |S_{nn}| \text{ dB}. \tag{2.8}$$

The insertion loss is the power lost between two ports, defined between port i and j as,

$$IL = |S_{ji}|^{-2} = -20 \log |S_{ji}| \text{ dB}. \tag{2.9}$$

Observe the negative sign for RL and IL in the above equations. The reflected and transmitted power would be,

$$R_{power} = |S_{nn}|^2 = 20 \log |S_{nn}| \text{ dB and,} \tag{2.10}$$

$$T_{power} = |S_{ji}|^2 = 20 \log |S_{ji}| \text{ dB}, \tag{2.11}$$

which has no negative sign. Generally for passive networks, all S_{ij} are complex valued with $|S_{ij}| < 1$ which means RL, IL are positive and R_{power}, T_{power} are negative [39]. Isolation between two ports i and j is defined as,

$$Iso = |S_{ji}|^2 = 20 \log |S_{ji}| \text{ dB} \tag{2.12}$$

similarly to the transmitted power. Cross-polarization, also referred to as cross-talk or polarization isolation, quantifies the leakage of one polarization component to the unwanted output port. For instance, an ideal scattering matrix for an OMT could be,

$$\begin{bmatrix} V_1^- \\ V_2^- \\ V_3^- \\ V_4^- \end{bmatrix} = \begin{bmatrix} 0 & 0 & 1 & 0 \\ 0 & 0 & 0 & 1 \\ 1 & 0 & 0 & 0 \\ 0 & 1 & 0 & 0 \end{bmatrix} \begin{bmatrix} V_1^+ \\ V_2^+ \\ V_3^+ \\ V_4^+ \end{bmatrix}, \tag{2.13}$$

where polarization 1 is inputted at port 1 and polarization 2 at port 2. Polarization 1 is fully coupled to port 3 and polarization 2 to port 4. In the non-ideal case, cross-polarization would be the power coupled from polarization 1 to port 4, i.e. the wrong port. This is defined as,

$$X\text{-pol} = |S_{pq}|^2 = 20\log|S_{pq}| \text{ dB}, \tag{2.14}$$

where p is the co-polarization (or wanted polarization) port and q is the cross-polarization output port (port which the co-polarization should not be coupled to).

2.3 Orthomode transducers

As described earlier, an orthomode transducer separates two input polarizations into two different outputs. There are an extensive number of OMT designs. To compare different OMT design's performances in a structured way, some general theory on OMT performance will be reviewed. Major parts of the theory in this section are presented in [44] which is a good reference for further background.

2.3.1 Input waveguide symmetry

Any perturbation in the input waveguide will affect the modal field distribution. In the orthomode transducer input waveguide there are two fundamental orthogonal modes. There will also exist a number of higher order modes depending on the desired bandwidth of the OMT. These modes can be divided into symmetrical and non-symmetrical modes. The symmetrical modes have a symmetrical field distribution with respect to either the XX' or YY' line in figure 2.5. A symmetric mode is defined as a mode which if mirrored through an axis is left unchanged. An anti-symmetric mode is defined as a mode which when mirrored through an axis its field has opposite direction but its field pattern is the same.

A waveguide geometry perturbation will transfer the modes firstly existing in the waveguide to other modes. For a symmetric mode about the XX' axis, a perturbation symmetric about the XX' axis will only generate modes symmetric to XX'. Moreover, for a symmetric mode about the XX' axis, a perturbation symmetric about both XX' and YY' will generate modes symmetric about XX' and anti-symmetric about YY'. For example, this would be the case for the TE_{10} mode in figure 2.5.

If some field coupling aperture or other device is added into the waveguide symmetrically at points X, X', Y and Y' as in figure 2.6 and the input mode is symmetrical about XX' the resulting generated modes would be symmetric about XX' and anti-symmetric about YY' [44]. This means that the fields coupled through apertures at X and X' will have same amplitude and phase (direction). By adding these fields with a 180° it is possible to cancel out the fields. Through apertures at Y and Y' however the field amplitudes will be equal with opposite phase. By adding these fields with 180° phase difference they will add constructively. [44]

By constructing the waveguide perturbations in a symmetric way as in figure 2.6 it is possible to cancel some and add some modes. For instance, all first six modes

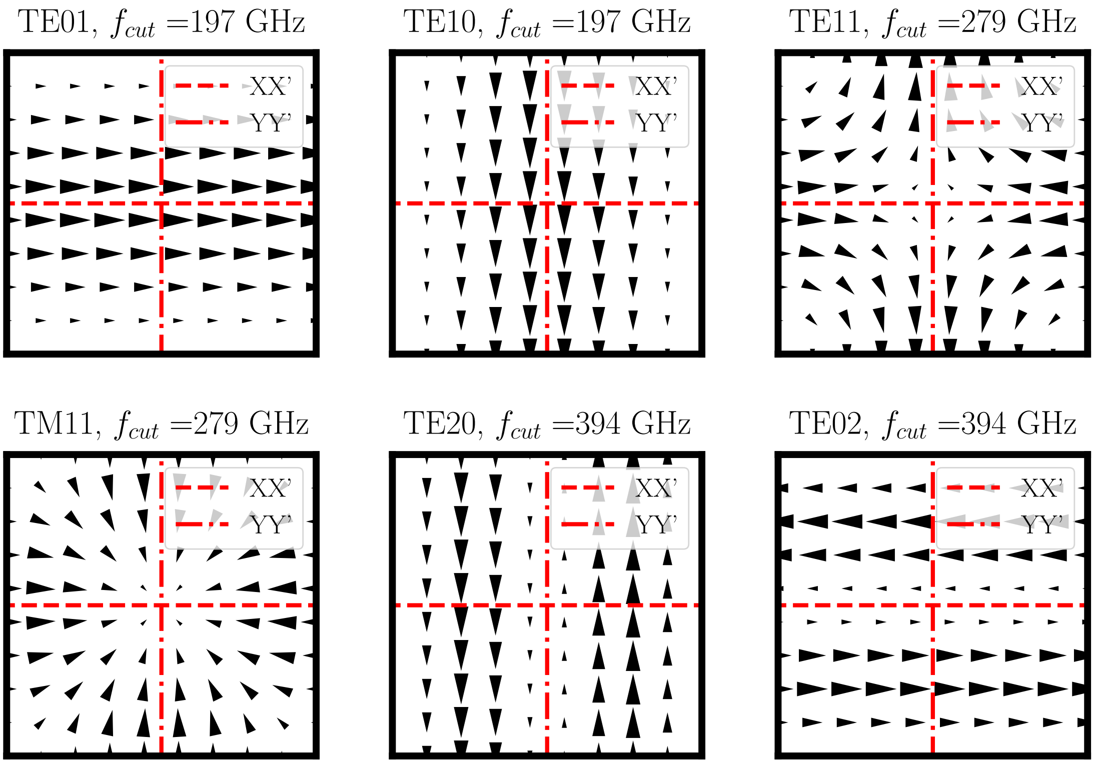

Figure 2.5: The E-field of the first six modal solutions for a quadratic waveguide are shown with waveguide symmetry cuts XX' and YY'. A symmetric mode is defined as a mode which if mirrored through an axis is left unchanged. An anti-symmetric mode is defined as a mode which when mirrored through an axis its field has opposite direction but its field pattern is the same.

except TE_{10} (as shown in figure 2.5) will cancel when combining the fields from Y and Y' with 180° phase difference. When adding the fields from apertures at X and X' with 180° phase difference, out of the six first modes, only TE_{10} will add constructively. This is the working principle for the most wide-band OMTs [26].

It is also possible to use coupling structures with either one symmetry as in figure 2.7 or no symmetry as shown in figure 2.8. In [44] some types of OMTs are categorized according to if the have either no, one or two symmetries in the input multi-mode waveguide.

2.3.2 Waveguide bends and combiners

If an OMT design is using either one or two symmetries it will need some kind of combiner component. A combiner taking two signals and adding them is a three-port device, and often its scattering matrix is represented by,

$$\mathbf{S}_{comb} = \begin{bmatrix} 0 & -\frac{1}{\sqrt{2}} & \frac{1}{\sqrt{2}} \\ -\frac{1}{\sqrt{2}} & \frac{1}{2} & \frac{1}{2} \\ \frac{1}{\sqrt{2}} & \frac{1}{2} & \frac{1}{2} \end{bmatrix}. \tag{2.15}$$

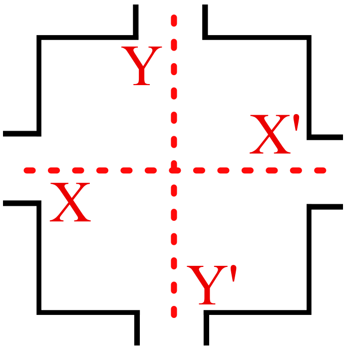

Figure 2.6: Waveguide cross-section with perturbations (coupling slots) symmetrically placed around both XX' and YY'.

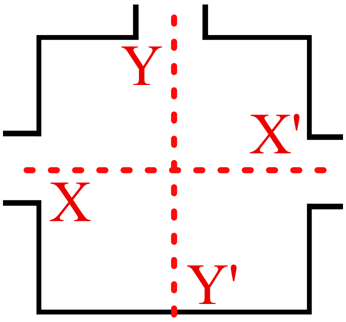

Figure 2.7: Waveguide cross-section with perturbations (coupling slots) symmetrically placed around both YY' but not around XX'.

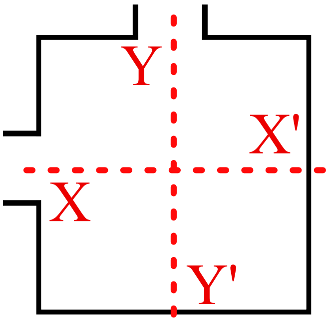

Figure 2.8: Waveguide cross-section with perturbations (coupling slots) not symmetrically placed around XX' nor YY'.

Here, port 2 and 3 are combined equally into port 1 but with 180° phase shift. As described previously, this kind of combiner with 180° phase shift between the inputs could be used in an OMT.

If a waveguide combiner is to be used, often there is a need for waveguide bends. Either E-plane or H-plane bends can be used depending on full layout of the OMT. An E-plane bend is a symmetric discontinuity with respect to the fundamental mode (TE_{10}) in a rectangular waveguide. This means that an E-plane bend will only add symmetric higher order modes. A H-plane bend however is a non-symmetric discontinuity with respect to the fundamental mode which will generate more higher order modes. Therefore, in theory, E-plane bends are easier to match and should be preferred over H-plane bends if applicable [44].

2.3.3 Orthomode junction types

As described earlier, a general input to an OMT is a dual polarized waveguide, for example the square waveguide. The orthomode junction (OMJ) in principle contain some kind of structure dividing the two polarizations. Some common methods used are finlines reported in [33], [45] and probe based OMJ reported in [35]–[38], [46], [47]. Also solely waveguide based designs such as the Bøifot type used in [24]–[27] and the turnstile type used in [28]–[30] are often used. Other simpler designs such as [48], [49] are also existing. There are some designs using waveguide couplers or slots, for example [31], [32], [50], which here are called coupler type. All these different techniques of separating polarizations can implement either a two-fold, one-fold or no symmetry as described earlier. Each type of OMJ, in terms of either waveguide, finline, probe or coupler based OMJ, has some limitations for bandwidth, material losses and use different types of manufacturing techniques. These aspects will be discussed in coming sections.

2.3.4 Waveguide based orthomode junctions

There exist a number of different designs using only waveguide components for the OMT, with one or two symmetries which are shown in table 2.1. The table is sorted so that the design that fulfills the highest number of design specifications for the OMT designed in this thesis is at the top.

FBW	f_0 [GHz]	**RL** [dB]	IL [dB]	X-pol [dB]	**Type**	**Number of symmetries**	**Tested?**	**Ref.**
54%	91.5	23	0.25	-45	Bøifot	2	yes	[25]
49%	93	20	0.8	-40	Turnstile	2	yes	[28]
40%	12.5	20	-	-50	Slot	1	yes	[51]
38%	92.5	17	0.3	-40	Bøifot	2	yes	[24]
27%	90	20	0.15	-	Waveguide	1	yes	[48]
58%	387.5	17	2.5	-35	Bøifot	2	yes	[26]
40%	275	14	0.7	-20	Turnstile	2	yes	[30]
26%	442.5	20	2	-	Bøifot	2	yes	[27]
20%	96	20	-	-	Slot	1	yes	[50]
10%	680	20	4.7	-15	Waveguide	1	yes	[49]
32%	100	17	0.35	-30	Coupler	2	yes	[31]
30%	235	20	0.6	-	Turnstile	2	no	[29]
26%	440	10	1	-30	Coupler	2	yes	[32]

Table 2.1: Comparison of different waveguide OMT designs sorted by how relevant they are to this design. The fractional bandwidth (FBW) referring to the bandwidth with the minimum return loss for both polarizations are shown under RL and maximum insertion loss for both polarizations shown in IL columns. Cross polarization (X-pol) is shown when given. If the device has been tested or not is shown in the "Tested?" column.

One design is the mentioned Bøifot junction [24]–[27] which either uses a septum or ridge to make one polarization continue straight through the junction. The other polarization is divided equally to the sides and then recombined. An example of the Bøifot junction is shown in figure 2.9. On the left side, the square waveguide, which support both polarizations, is shown. The junction will act as a waveguide to ridge waveguide transition and then ridge waveguide to rectangular waveguide for the vertical polarization. For the horizontal polarization it will act as a divider with equal amplitude and negative phase difference. The vertical polarization is bent out by a waveguide bend so the horizontal polarization can be recombined. In this particular configuration it is fully symmetric and only has E-plane bends, from [44] this design could therefore theoretically be one of the most wide-band designs.

Another waveguide based design is based on the turnstile junction reported in [28]–[30] where both polarizations are divided equally and then recombined which is shown in figure 2.10. On the right, the cut-out shows the inner structure of the junction where a pin provide matching. Both input polarizations are divided equally with opposite phase to rectangular waveguide outputs. Each polarization is then

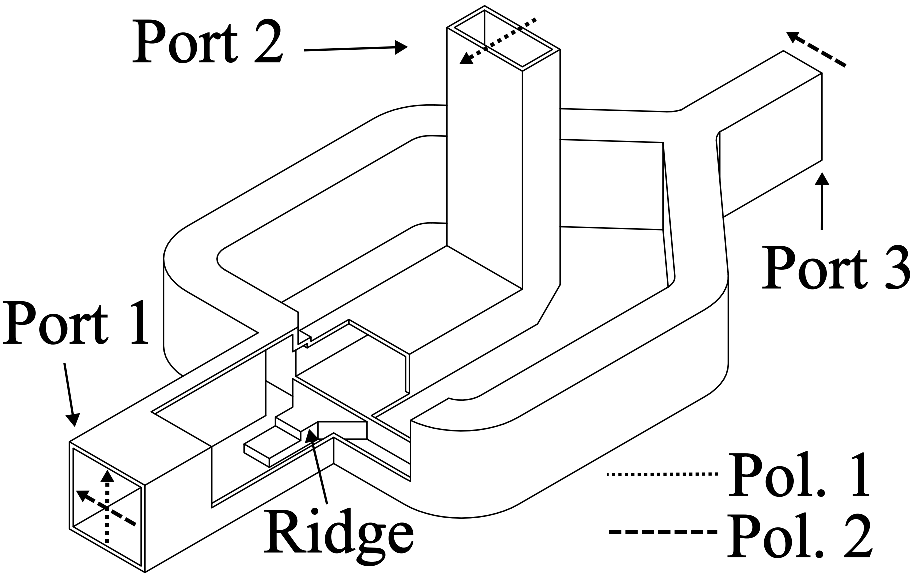

Figure 2.9: Illustration of the design often called Bøifot or double-ridged OMT. Port 1 hosts both polarization 1 and 2 as indicated. For visibility, the waveguide is cut open to reveal the bottom ridge.

recombined as shown on the left in figure 2.10. For both polarizations, the turnstile junction is a symmetric structure and E-plane bends can be used instead of H-plane bends which make the turnstile design one of the most broad-band theoretically [44].

To summarize, both Bøifot and turnstile types are symmetric for both input polarizations which enable these designs to cover wide bandwidths with high return loss. It is possible to achieve bandwidths similar to the whole rectangular waveguide band, shown in [25], [26] with 54% respectively 58% fractional bandwidth.

In table 2.1 the turnstile type is shown to have bandwidth close to the whole waveguide band [28]–[30] with 40%, 49% and 30%. From its layout however it needs more waveguide bends and is not as compact as the Bøifot OMT which also degrade its insertion loss [25], [26].

There are also some simpler waveguide designs only symmetric for one polarization, which in table 2.1 is called waveguide type. An example of a layout is shown in figure 2.11 which is similar to [48]. The vertical polarization will continue straight through the junction while the horizontal polarization is bent out to the side. The junction is symmetric only for the horizontal polarization. Some examples achieve bandwidths of 27% [48], 40% at 12.5 GHz [51] and 20% [50]. These do not need any recombination of separated signals which makes their layouts simpler.

A fourth type of waveguide OMT has also been tested using backward coupling technique to achieve bandwidths of 32% [31] and 26% [32], however the couplers set high requirements on manufacturing and assembly accuracy [32].

Manufacturing of the waveguide OMT has a major effect on OMT performance. The Bøifot and simpler waveguide designs are possible to make in split-block technique

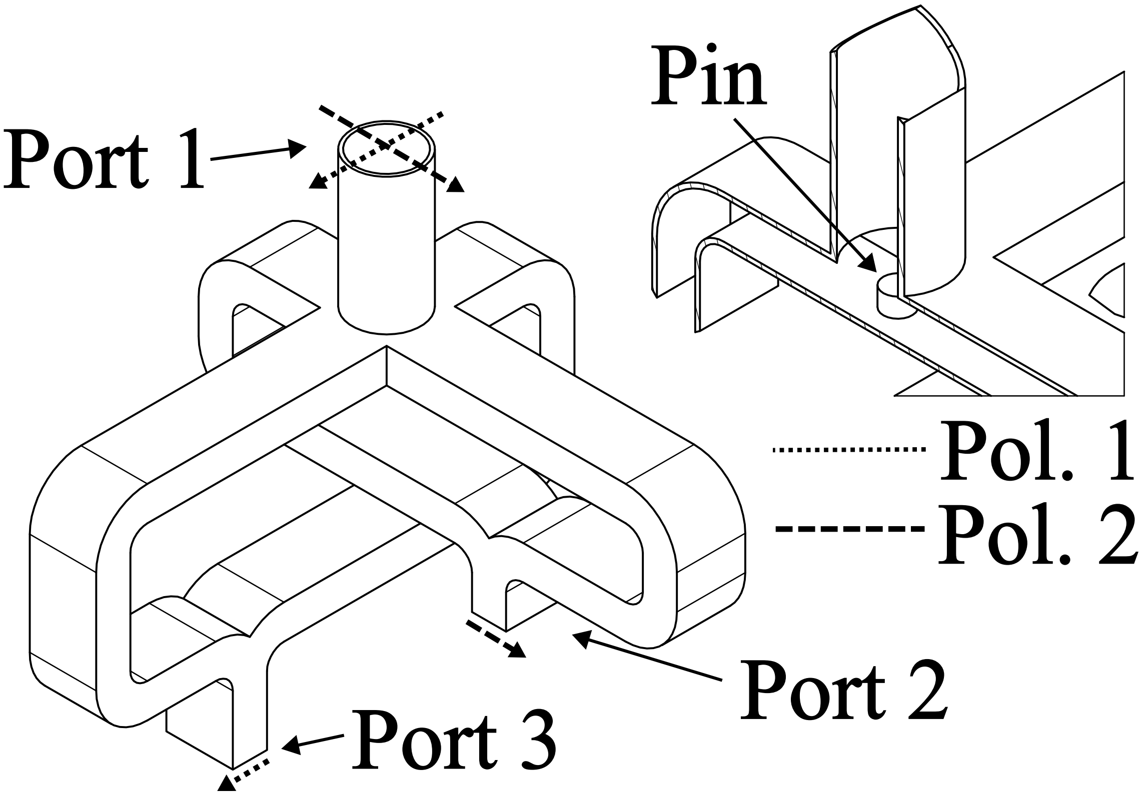

Figure 2.10: Illustration of the turnstile OMT design. The input port 1 hosts both polarizations as indicated. The junction is cut to reveal the turnstile junction, containing a pin.

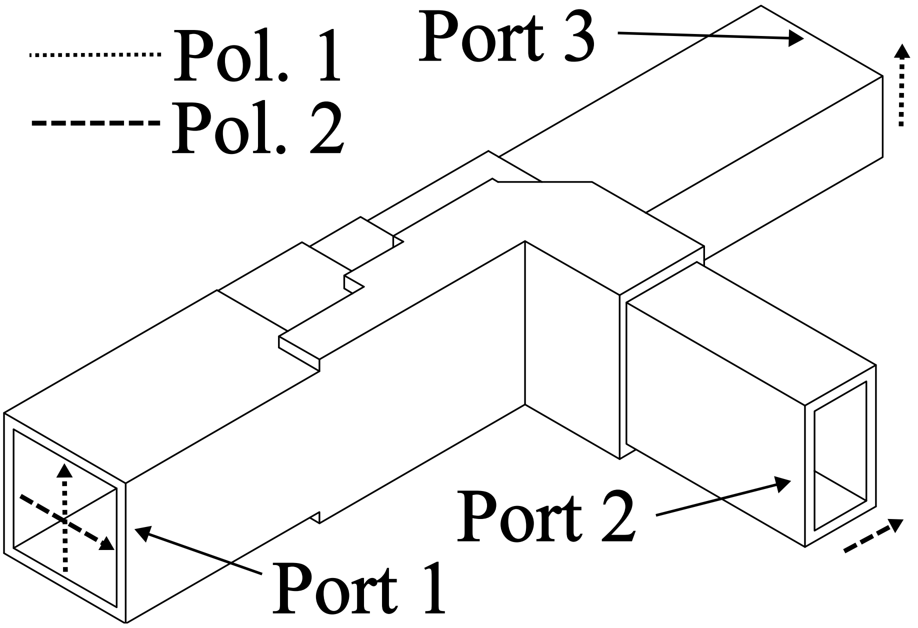

Figure 2.11: An example of a waveguide based OMT with one symmetry (similar to [48]). Port 1 inputs the two polarizations which are then split into port 2 and 3.

with only one split [25], [26], [48], [50], [51], however this also means that at some point one of the output waveguides will have a H-plane cut which degrades the insertion loss for one polarization seen in [26] for example. CNC milling is the most commonly used manufacturing technique for waveguide OMTs which also puts some limitations on scale-ability to higher frequencies.

2.3.5 Probe based orthomode junctions

The probe based OMT designs make use of probes inserted into the multi-mode input waveguide to separate polarizations. A simple design similar to that in [38] is shown in figure 2.12 where a circular dual polarization waveguide is the input from the top. Two probes on a substrate are inserted in the waveguide which couple to each of the two polarizations. A fully symmetric example is shown in figure 2.13 where a quadratic waveguide input supporting the two polarizations enter from the top. Four probes are inserted into the waveguide and each polarisation will be divided into the to opposite probe out-puts. This configuration needs, as the turnstile or Bøifot junctions, some recombining circuitry. In [35], [37], [46] this is done on chip which will require some crossover of the lines.

Some probe-based designs are shown in table 2.2. 36% fractional bandwidth is achieved in [46], 31% in [37] and 26% in [35]. These three examples are symmetric for both polarizations (using two probes per polarization) and combine the signals on chip. Even though a two-fold symmetry is used, the bandwidth is less than for waveguide based designs. The difference between waveguide based and probe base OMTs could be explained by a general review of impedance matching. A component is easier to match to another component if their impedances are similar generally [39]. The waveguide impedance is around 400 Ω and typical microstrip line impedance is

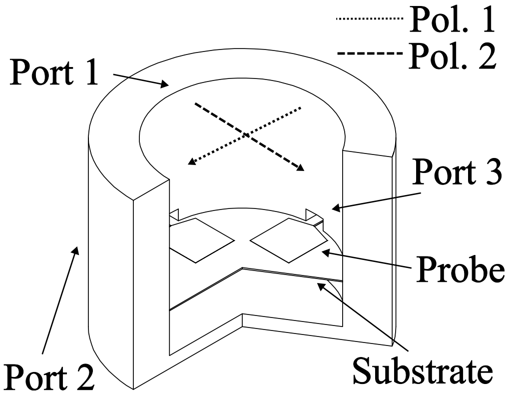

Figure 2.12: Example of a probe based OMT with two probes. The probes are made on a thin suspended substrate. Port 2 and 3 are based on microstrip lines in this example.

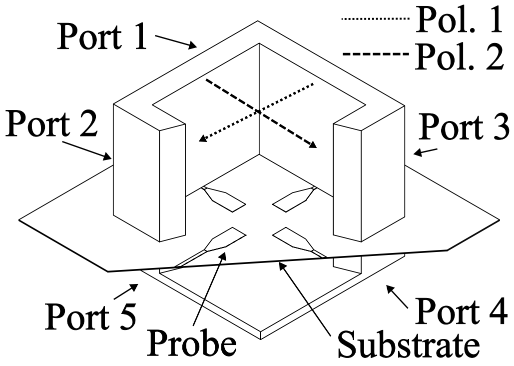

Figure 2.13: Example of a probe based OMT with four probes. The probes are made on a thin suspended substrate. Port 2, 3, 4 and 5 are based on microstrip lines in this example.

around 50 Ω. A fully waveguide based OMT therefore have more similar impedances of the input and outputs to match. The general case of impedance matching can be reviewed in [39]. Non-symmetric probe designs also exist, for example a reported fractional bandwidth of 16% for [38] and 14% for [47].

FBW	f_0 [GHz]	**RL** [dB]	IL [dB]	X-pol [dB]	**Type**	**Number of symmetries**	**Tested?**	**Ref.**
36%	22	13	0.65	-30	Probe	2	yes	[46]
16%	340	20	-	-	Probe	0	yes	[38]
31%	225	20	-	-	Probe	2	no	[37]
26%	144	18	-	-	Probe	2	yes	[35]
14%	600	15	-	-30	Probe	0	-	[47]

Table 2.2: Comparison of different OMT designs sorted by how relevant they are to this design. The fractional bandwidth (FBW) refers to the bandwidth with the minimum return loss for both polarizations are shown under RL and maximum insertion loss for both polarizations shown in IL column. Cross polarization (X-pol) is shown when given. If the device has been tested or not is shown in the "Tested?" column.

The probe based OMTs are easy to implement because there is no need for intricate waveguide matching structures as for the waveguide based OMTs. The accuracy of chip manufacturing is also higher than for waveguide components. If the most important design parameters are part of the chip, tolerance to block manufacturing could be improved. Introducing dielectric loss into the design will degrade insertion loss which is a drawback of these designs.

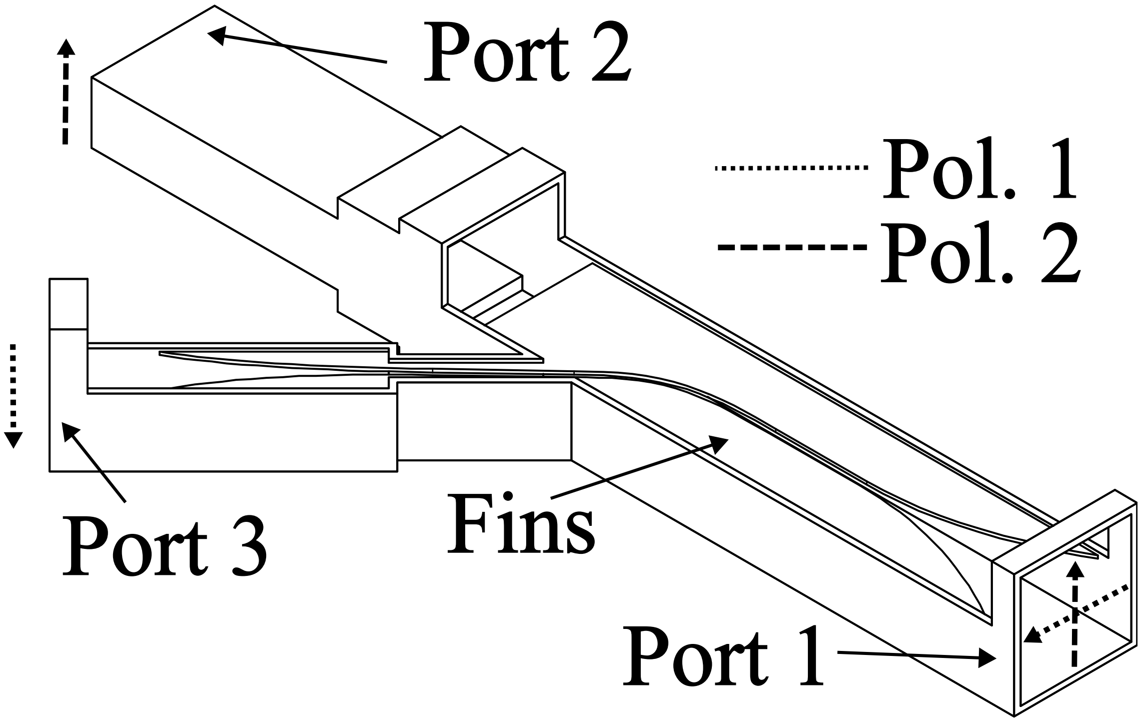

Figure 2.14: Finline OMT example, with common input port 1 for both polarizations. The fins are metal, deposited on a substrate, the substrate is not shown in this figure for simplicity.

2.3.6 Finline based orthomode junctions

Finline OMTs transfer one of the polarizations to a finline [52], after which that polarization can be guided to another waveguide via the finline. An example of a finline design is shown in figure 2.14 where the input quadratic waveguide is on the right. Polarization 1 is transferred straight through the OMJ after which the quadratic waveguide is converted to rectangular waveguide. For this polarization the junction is not symmetric. Polarization 2 is picked up by the finline structure and the field is concentrated in the small gap between the fins. The finline is then bent out of the waveguide and transferred to a rectangular waveguide output which is all symmetric. This OMT therefore has one symmetry.

Some finline OMT designs are shown in table 2.3. Fractional bandwidth of more than 40% is achieved for [33], [34], [45] which is in parity to waveguide designs symmetric to both polarizations. A resistive strip is often added at the end of the finline septum just before the quadratic to rectangular waveguide to suppress the generation of unwanted modes [45]. If not suppressed, these could degrade cross-polarization of this OMT. Generally, a transition from waveguide to finline is more broadband than a waveguide probe transition, which could be explained by the wide range of realize-able impedances for the finline. This could also explain why the fractional bandwidths of [33], [34], [45] are wider than for the probe designs [35]–[38], [46], [47].

The finline production process is often done by depositing a metal on a thin layer

FBW	f_0 [GHz]	**RL [dB]**	IL [dB]	X-pol [dB]	**Type**	**Number of symmetries**	**Tested?**	**Ref.**
40%	10	20	0.3	-20	Finline	1	yes	[45]
42%	950	15	7	-40	Finline	1	yes	[33]
42%	950	20	1.5	-50	Finline	1	no	[34]

Table 2.3: Comparison of different OMT designs sorted by how relevant they are to this design. The fractional bandwidth (FBW) refers to the bandwidth with the minimum return loss for both polarizations are shown under RL and maximum insertion loss for both polarizations shown in IL column. Cross polarization (X-pol) is shown when given. If the device has been tested or not is shown in the "Tested?" column.

of dielectric as in [33], [53]. The distance between the fins has a strong effect on matching and the dielectric layer is needed to achieve required accuracy [34]. The effect of the dielectric layer needs to either be compensated through some extra matching section before the finline [54], removal of dielectric before the finline [53] or having a dielectric layer so thin that it does not affect as much [34]. These extra processes complicate production compared to probe designs.

Thicker metal layers (5 µm) have also been used for finlines [33], [53] than for probe designs [35], [38] (<0.5 µm). The thicker metal also complicates the microfabrication process compared to probe designs.

2.3.7 Comparison of OMT designs

There are a vast number of publications on OMT designs and production. The focus in this thesis is on wide-band ($>$ 30% fractional bandwidth) and with millimeter wave (30 GHz-300 GHz) or sub-millimeter wave (300 GHz-3 THz) operating frequencies. Also, OMTs that have been produced and tested are preferred because it is expected that simulated values are not representative because of uncertainties in the manufacturing processes.

The designs already mentioned are summarized for comparison in table 2.4 and sorted according to how many design specifications they fulfill. Both the Bøifot and turnstile types perform well with wide bandwidths and good return loss. Their insertion loss is also low, the Bøifot type having somewhat lower loss probably because of the shorter waveguide lengths. The most wide-band design presented is [26] which also has a center frequency close to the desired one. In this case the high insertion loss is due to the wide bandwidth of the OMT because at the lower frequencies, the waveguide cut-off has a large effect on loss. This means with a smaller band of operation [26] could have resulted in insertion loss and return loss consistent with the specifications. A drawback of the Bøifot not presented in the table is that it requires very fine machining of the matching sections. It also introduces a part of waveguide cut in H-plane and therefore needs to be assembled with high accuracy and especially good electrical contact between the blocks at the part cut in H-plane.

One finline design fulfill all design specifications in table 2.4, however with a central frequency of 10 GHz in [45] where a substrate was not used to support the fins. At 327.5 GHz some substrate would be needed which make the design more complicated as seen in [33], [34] where the return loss is too low but especially the insertion loss too high.

A design simpler to produce is the probe design even though it is not as wide-band as the finline or waveguide based designs in table 2.4. Only [46] of the probe designs present a wider bandwidth than the design specifications, and that is with a return loss of 13 dB and center frequency of 22 GHz. However [46] uses coaxial cables as lines and only use simple probes in the input waveguide which could be improved upon. The insertion loss could probably also be improved by reducing the length of coaxial lines. In simulation, [37] reaches a bandwidth and return loss that almost achieve the design specifications. If the bandwidth could be improved, then maybe the design parameters could be fulfilled. Also [36] reaches a reasonable bandwidth. There could be room for improvement in the probe based designs which would meet the design specifications.

FBW	f_0 **[GHz]**	RL **[dB]**	IL **[dB]**	X-pol **[dB]**	**Type**	**Number of symmetries**	**Tested?**	**Ref.**
54%	91.5	23	0.25	-45	Bøifot	2	yes	[25]
40%	10	20	0.3	-20	Finline	1	yes	[45]
49%	93	20	0.8	-40	Turnstile	2	yes	[28]
40%	12.5	20	-	-50	Slot	1	yes	[51]
38%	92.5	17	0.3	-40	Bøifot	2	yes	[24]
27%	90	20	0.15	-	Waveguide	1	yes	[48]
58%	387.5	17	2.5	-35	Bøifot	2	yes	[26]
42%	950	15	7	-40	Finline	1	yes	[33]
42%	950	20	1.5	-50	Finline	1	no	[34]
40%	275	14	0.7	-20	Turnstile	2	yes	[30]
36%	22	13	0.65	-30	Probe	2	yes	[46]
26%	442.5	20	2	-	Bøifot	2	yes	[27]
20%	96	20	-	-	Slot	1	yes	[50]
16%	340	20	-	-	Probe	1	yes	[38]
10%	680	20	4.7	-15	Waveguide	1	yes	[49]
32%	100	17	0.35	-30	Coupler	2	yes	[31]
31%	225	20	-	-	Probe	2	no	[37]
30%	147.5	13	1.8	-	Probe	2	yes	[36]
30%	235	20	0.6	-	Turnstile	2	no	[29]
26%	440	10	1	-30	Coupler	2	yes	[32]
26%	144	18	-	-	Probe	2	yes	[35]
14%	600	15	-	-30	Probe	1	-	[47]
Design specifications:								
35%	327.5	20	0.5	-25	-	-	-	-

Table 2.4: Comparison of different OMT designs sorted by how relevant they are to this design. The fractional bandwidth (FBW) refers to the bandwidth with the minimum return loss for both polarizations are shown under RL and maximum insertion loss for both polarizations shown in IL column. Cross polarization (X-pol) is shown when given. If the device has been tested or not is shown in the "Tested?" column.

2.4 Theoretical evaluation of novel design

From the comparison of some orthomode transducer designs in section 2.3.7 there are some positive and negative aspects for all design alternatives, waveguide, finline and probe-based designs. The probe-based design is appealing because of its simple production and scale-ability to higher frequencies. Its main drawback being bandwidth and increased losses of microstrip transmission lines compared to waveguide. The design specifications would require a bandwidth of 36%, return loss of better than 20 dB, insertion loss better than 0.5 dB and cross polarization less than −25 dB which none of the probe designs in [35]–[38], [46], [47] achieve. This section aims at investigating if it is possible to achieve these specifications with a novel probe design. The idea is to transition into waveguide after the probe type orthomode junction, as shown in figure 2.15 as a non-symmetric variant or figure 2.16 as a symmetric variant.

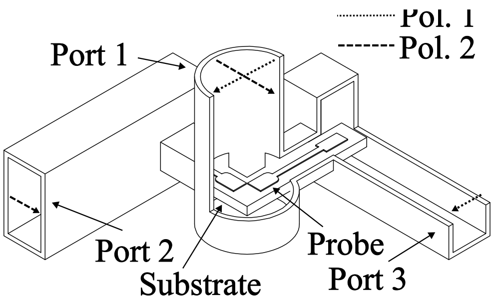

Figure 2.15: Non-symmetric variant of the novel orthomode transducer idea. The polarizations are extracted from circular input waveguide via probes and re-launched into waveguides.

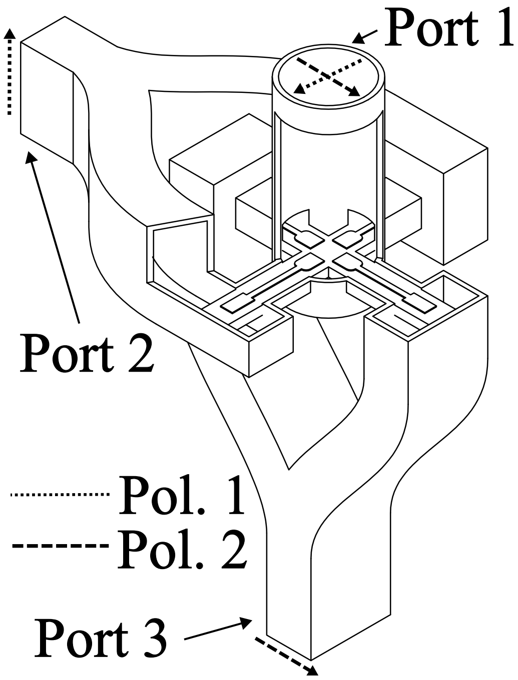

Figure 2.16: Symmetric variant of the novel orthomode transducer idea. The polarizations are extracted from circular input waveguide via probes and re-launched into waveguides.

To make some prediction of return loss and bandwidth, the full OMT was divided into orthomode junction (OMJ), microstrip transmission line, microstrip to waveguide transition and waveguide combiner. Only the fully symmetric probe designs in [35]–[37], [46] come close to the desired bandwidth of 36%. If the bandwidth of [37] could be improved from 31% then it would be possible to have an OMJ with the desired bandwidth.

The next transition that could limit bandwidth and return loss is the transition from microstrip to rectangular waveguide. In [55] a bandwidth of 37% with return loss of 18 dB is reported which if improved upon could be used in the OMT.

Lastly the combiner needs to be broad-band enough. In [56]–[58] return losses of better than 20 dB are achieved over 38%, 32% and 38% fractional bandwidths. The conclusion is that it could be possible to put together OMJ, microstrip to waveguide transition and combiner and fulfill the design specifications.

To make a prediction of the expected insertion loss also line losses can be taken into account. A loss model presented in [59] were used to estimate the losses for waveguides via,

$$\alpha(\omega) = \frac{\lambda_0}{b\lambda_g}\left(\frac{\pi\Psi}{\lambda_0\eta\sigma}\right)^{\frac{1}{2}}\left[1+\left(\frac{\lambda_g}{2a}\right)^2\cdot\left(1+2\frac{b}{a}\right)\right]\cdot 8.686\,\mathrm{dB/m}. \tag{2.16}$$

λ_0 is the free space wavelength, η the free space impedance, σ the waveguide metal conductivity, λ_g the guided wavelength, a and b waveguide dimensions and Ψ a constant to account for surface roughness and other effects. For a waveguide with dimensions $a = 0.76$ mm and $b = 0.38$ mm and material parameters from [59] the maximum loss in the band would be about 0.02 dB/mm. If for example a waveguide length of 5 mm is used, then the loss will be approximately 0.1 dB.

For the microstrip loss Keysight ADS [1] can be used to estimate the loss by the *Linecalc* feature. A gold microstrip line on 65 µm quartz substrate can be simulated to have 0.17 dB/mm loss, which, using a 0.5 mm line would result in about 0.09 dB of loss. A gold microstrip line on 30 µm silicon substrate can be simulated to have about 0.3 dB/mm of loss which would result in 0.15 dB. Another effect that will appear as loss is reflected power at all transitions from waveguide to probe and back. A 20 dB return loss corresponds to about 0.05 dB of insertion loss which, if assuming at both probe interfaces give about 0.1 dB of insertion loss. The sum of these losses become about 0.3 dB which is lower than the design specification of $IL = 0.5$ dB. A measurement supporting this is [60] where the back-to-back insertion loss of about 0.3 dB for a waveguide to microstrip on 65 µm quartz substrate was reported at 100 GHz.

2.5 Permittivity modelling and measurement

Some alternative materials could be used as substrate out of which Gallium Nitride (GaN) initially was simulated as the most promising. To design probes with substrate material of Gallium Nitride (GaN) a reliable value of GaN permittivity is needed. Permittivity describes the polarizability of a material, specifically a dielectric and it affects the field distribution in the material [40].

There is uncertainty about the permittivity of GaN at about 300 GHz. In some sources describing design of millimeter wave active components, $\epsilon' = 9.5$ is used in [61]–[63]. The low frequency limit is therefore rather well-known to be about $\epsilon' = 9.5$. For the design of a receiver device for 1300 GHz permittivity was estimated by [64] as $\epsilon' = 4.9$ by measuring a resonator using GaN. This agrees with time-domain spectroscopy measurements done by [65] which also have measurements as low as 500 GHz. There is some disagreement with other reported values being [66] where $\epsilon' = 9.5$ is reported at 1300 GHz. This suggest that the dielectric properties of GaN have a strong dependence on frequency, especially in the band of operation and raises the need for characterizing the GaN sample being used for the OMT at the frequency of operation.

In figure 2.17 an illustration of the complex permittivities dependence on frequency is shown as also shown in [67]. A more detailed review of dielectric theory is given in appendix B. Four different effects are indicated in figure 2.17, which are, ionic, orientation, atomic, and electronic effects. In GaN at sub-millimeter frequencies atomic and electronic effects are most important. GaN is a crystal, which means orientation effects are not present and ionic effects are mostly present at lower frequencies [67]. The atomic effect and electronic effect will create resonances in ϵ', and at the corresponding frequencies, peaks in ϵ''. The material losses increase with ϵ'' which means the material losses are high at the atomic and electronic resonances in a material. If a resonance is in the frequency band of operation, losses could increase drastically. This also motivates the characterization of GaN for $270 - 385$ GHz.

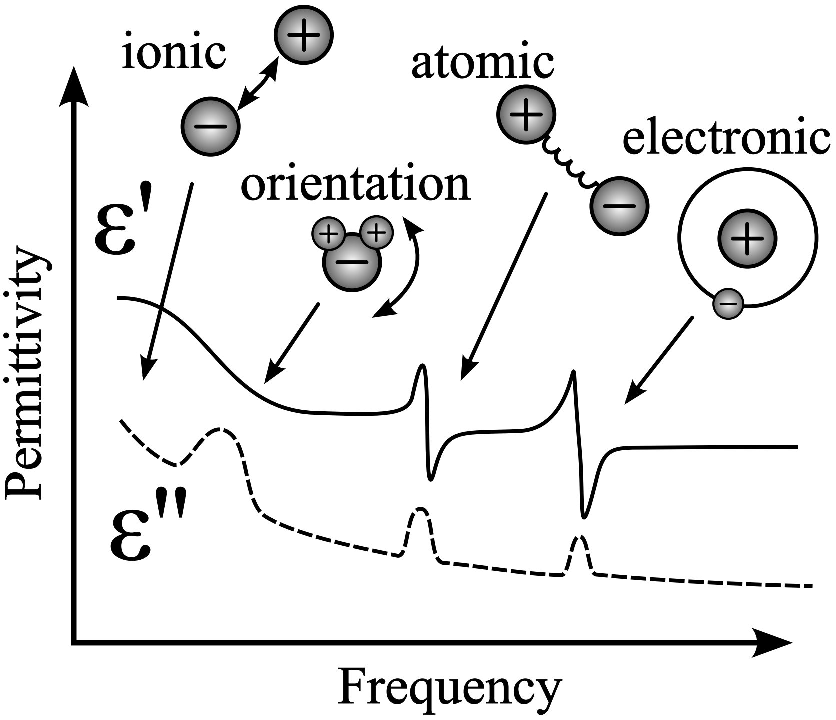

Figure 2.17: Illustration of how the real part ($\epsilon' = \Re(\epsilon)$) and imaginary part ($\epsilon'' = -\Im(\epsilon)$) of the complex permittivity are dependent on frequency. The different phenomena are indicated.

3

Methods

The aim of this thesis was to design, manufacture and characterize a novel orthomode transducer. The method chapter describes and motivates the methods used. The design contained substrate of gallium nitride which as described in section 2.5 motivated a characterization of dielectric properties of gallium nitride. Initially the design assumed the electrical properties of GaN but was later modified for measured properties. The manufacturing processes are described in separate sections then followed by characterization and measurement methods used.

3.1 Orthomode transducer design

The orthomode transducer design (OMT) process was divided into some steps described by the coming sections. Firstly, the orthomode junction (OMJ) part of the OMT was designed for optimum bandwidth. In the case of the probe design, the OMJ includes only what is shown in figure 2.13, the input waveguide, several probes and a short line. Using the full-wave solver software Ansys HFSS (HFSS) [2] the OMJ scattering parameters were simulated. The impedance of the output microstrip lines was not decided at this stage to be able to find the best probe input impedance.

Secondly, after the initial OMJ design, rectangular waveguide probes were designed to transfer the microstrip lines into rectangular waveguide. The microstrip dimensions and therefore impedance was set after the initial step of OMJ design.

Lastly, the combiners were designed separately. The OMJ and rectangular waveguide probes were assembled and simulated together in HFSS, some adjustments were done and then all three components were put together to create the full OMT. Coming sections describe the process in more detail.

3.1.1 Orthomode junction design

3.1.1.1 Design comparison

Some alternative substrates and probe geometries were investigated first. Simple 3D models were modelled in HFSS for the different types of probes and substrates. In HFSS it is possible to run a large number of simulations and try many different geometries of probes. It is also possible to optimize the geometrical dimensions to achieve optimum return loss and insertion loss for example [2]. For these first models the optimizer was run to get an indication out how promising the different alternatives were.

The investigated substrates were quartz of thickness 65 µm, silicon (Si) of thickness 65 µm or 5 µm and gallium nitride (GaN) of thickness 65 µm or 5 µm. The thinner substrates are what [35]–[38] all used. The probe shapes tried were radial probes as in [36] and rectangular probes as in [35], [37], [38] which all are OMTs with two symmetries, meaning that they use four probes.

After the initial simulation runs, it was decided that the results for thin substrates of Si and GaN and probes of rectangular shape were most promising. Another positive prospect is that Si or GaN can be etched into shapes other than rectangular, this could in theory enable for some self-alignment of the substrate within the block. For quartz, the substrate needs to be diced, which means four pieces are needed for the four probes.

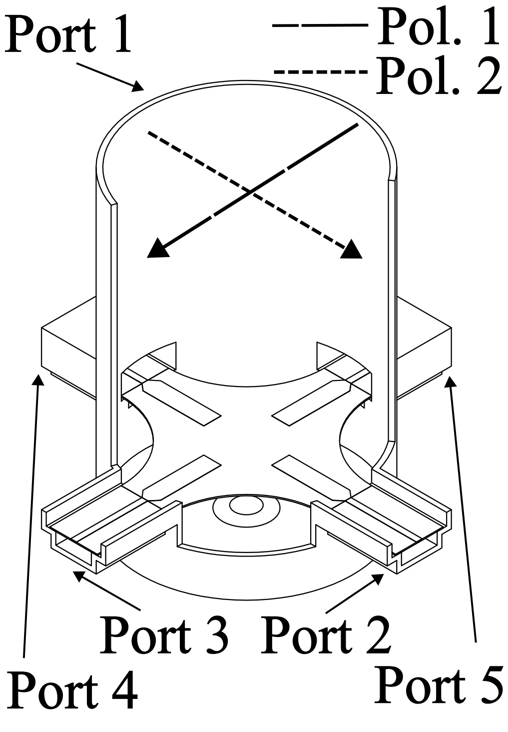

Figure 3.1: Illustration of model of OMJ with GaN thinfilm (5.5 µm thick) and four probes. Simulation ports (*wave ports*) are indicated and the two input polarizations.

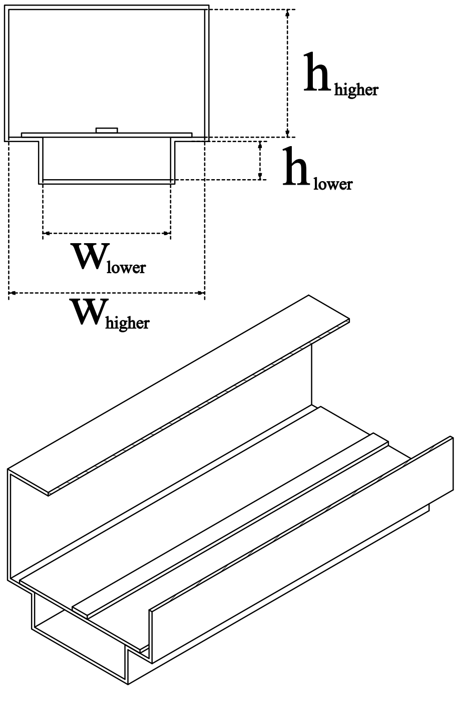

Figure 3.2: Illustration of simulated the channel with GaN substrate and a microstrip-like or stripline-like transmission line.

3.1.1.2 Optimization of OMJ

The optimization of the OMJ served to find the optimum shape and dimension to transfer the two modes in the circular waveguide to the four output lines. For the GaN substrate a more detailed model was created similar to the model in figure 3.1.

The figure contains the thinfilm substrate of GaN with four probes extended into the waveguide input circular waveguide.

Before optimization of the whole OMJ, some limits were put on the dimensions. The four channels shown in figure 3.2 were simulated in HFSS. For visibility some waveguide walls are cut in figure 3.2. The simulation was to ensure that only one mode existed in the channels at these frequencies and investigate what line impedance was possible to realize. A wide range of impedances were needed to be realizable to allow the probe shape not to be constrained by the line impedance. In [35]–[38] the output lines are constrained to low impedance values of around 50 Ω. This constraint is not needed for the design in this work because the line will lead to a probe which does not need a 50 Ω line impedance to work. In HFSS, *wave ports* were used as port definitions. Then, the HFSS solver solves for a specified number of modes the propagation constant and wave impedance for those modes [2]. Wave ports with four modes were used at the two sides of the channel to simulate the scattering parameters of the channel. No higher order modes were found to exist in the band for channel width $w_{higher} < 200\,\mu\text{m}$ and channel height $h_{higher} < 150\,\mu\text{m}$.

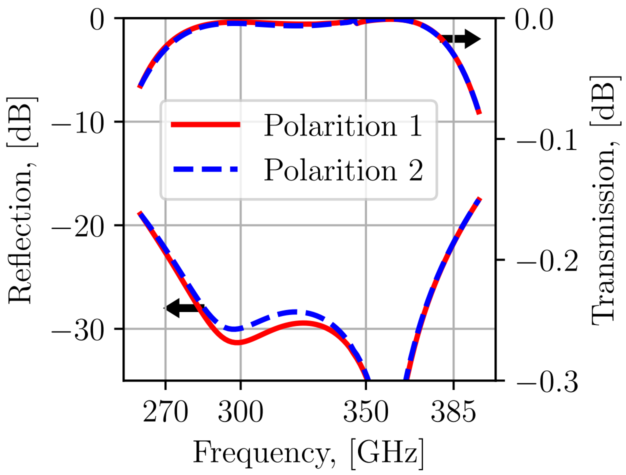

Figure 3.3: Power reflection and transmission for the two polarizations after optimization of OMJ.

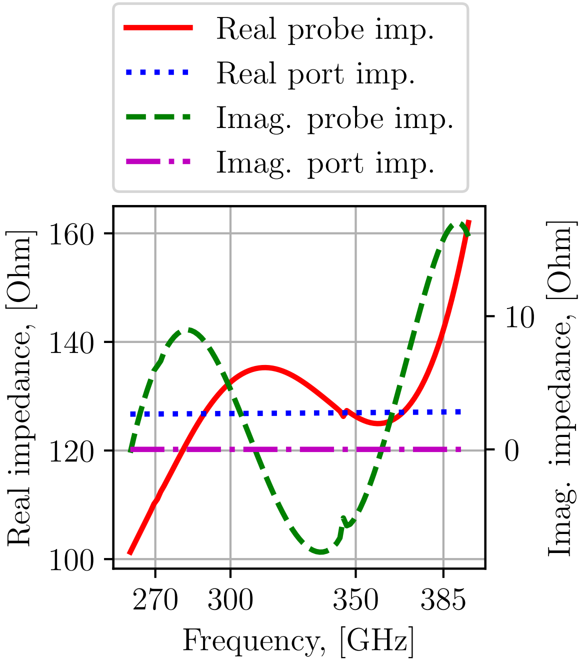

Figure 3.4: Real and imaginary probe impedance of the optimized OMJ as function of frequency. Also, real and imaginary port impedance of the output ports (port 2, 3, 4, 5 in figure 3.1).

After the simulations of just the channel the model shown in figure 3.1 were parameterized, meaning the modelling was done so that all relevant dimensions of the model could be changed by the program HFSS itself. This is needed for HFSS to run optimization of the dimensions. The dimensions first brought into the model were the ones shown in figure 3.2 for the channel and backshort distance d_{bsOMJ}, probe width w_{OMJP}, probe length l_{OMJP}, probe chamfer length l_{OMJcut}, pin height h_{pin} and pin radius r_{pin}. The backshort distance d_{bs} is the distance from bottom of the thinfilm to the bottom of the circular waveguide and the pin is visible in figure 3.1 in the bottom of the circular waveguide bottom.

The optimization was run firstly with the *Multi-Objective Genetic Algorithm* (genetic algorithm) and then the *Adaptive Single-Objective* (gradient algorithm) which are both built-in optimization features in HFSS [2].

The optimized results for the orthomode junction only are shown in figure 3.3. The resulting probe impedance is shown in figure 3.4 together with the simulated port impedance of the channel.

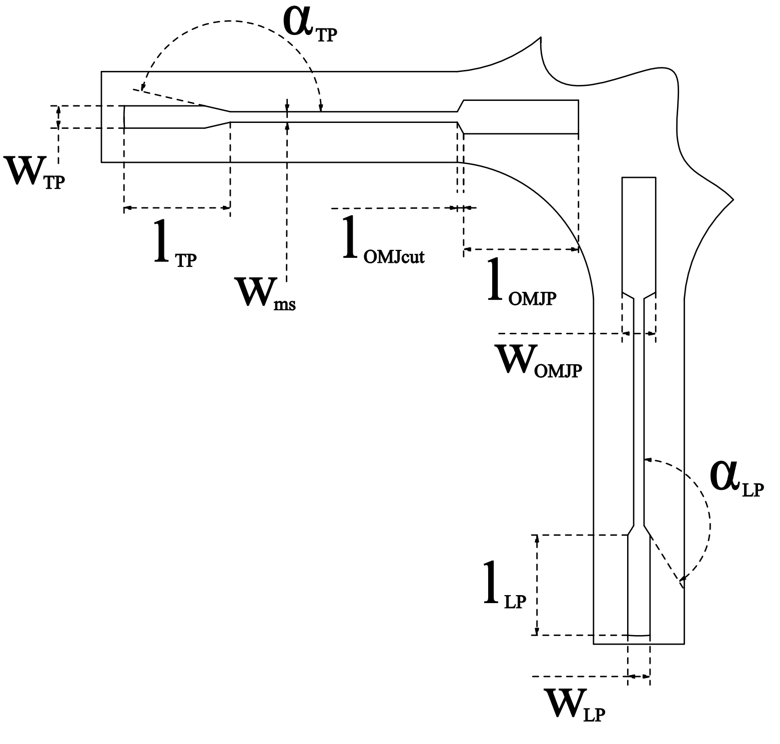

Figure 3.5: Probe dimensions for the OMJ probes, longitudinal probes and transversal probes are shown. The chip is symmetric for each of the arms and for visibility half of the chip is cut away in this figure.

3.1.2 Rectangular waveguide probe design

The next components of the orthomode transducer are the two microstrip or stripline to waveguide transitions, here called rectangular waveguide probes (RWG probes). The transition where the substrate is in the transversal plane (TP) of the waveguide is shown in figure 3.6 and the transition where the substrate is in the longitudinal plane (LP) of the waveguide is shown in figure 3.7. Similarly to the OMJ model, *wave ports* were used in the channels and waveguides. The resulting channel and strip-line dimensions were input into the model and probe length l_{TP}, l_{LP}, probe width w_{TP}, w_{LP}, probe chamfer angle α_{TP}, α_{LP} and backshort distance d_{bsTP}, d_{bsLP} were parameterized. These are shown in figure 3.5. Optimization was run with the genetic algorithm first and then the gradient algorithm as for the OMJ.

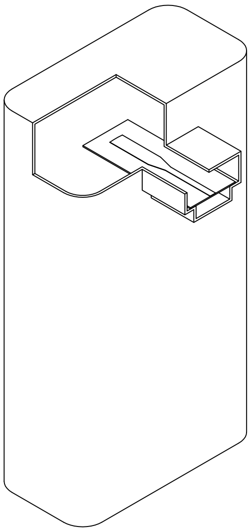

Figure 3.6: Illustration of the optimized model for the transversal probe (TP) with same input port dimensions as was optimized for the OMJ.

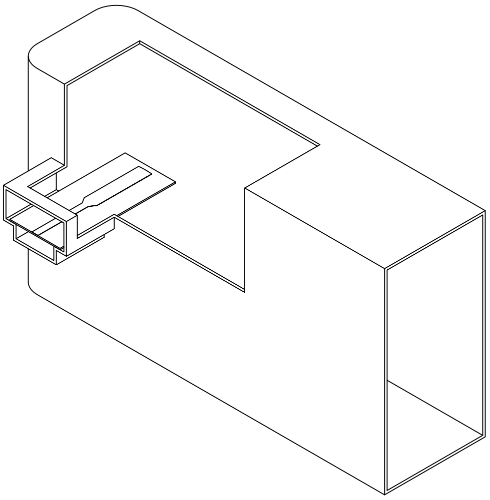

Figure 3.7: Illustration of the optimized model for the longitudinal probe (LP) with same input port dimensions as was optimized for the OMJ.

Resulting reflected and transmitted power for the initially optimized RWG probe dimensions with plain wave ports at all ports are shown in figure 3.8 and 3.9. Figure 3.8 corresponds to the longitudinal probe (LP) (figure 3.7). For the transversal probe (TP) in figure 3.6 the results are shown in figure 3.9.

To add the effect of the OMJ into the optimization of the RWG probes without the need to simulate both OMJ and probes in the same model post-processing functions in HFSS were used. From the OMJ model, active impedance parameters, plotted in figure 3.4, for the channel ports were exported. The channel wave ports for the two RWG probe models (figures 3.6 and 3.7) were then re-normalized for this impedance. A second iteration of optimization was then run for the two probe models in figures 3.7 and 3.6.

After re-optimization of the probe dimensions the results shown in figure 3.10 and 3.11 were acquired for the longitudinal respectively transversal probes.

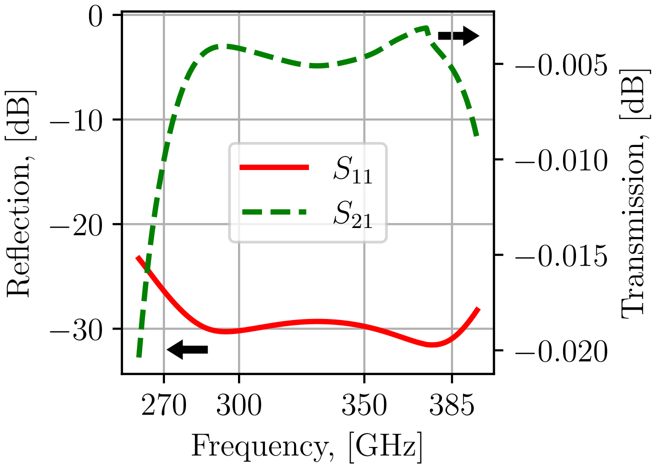

Figure 3.8: Power reflection and transmission after initial optimization of the longitudinal probe.

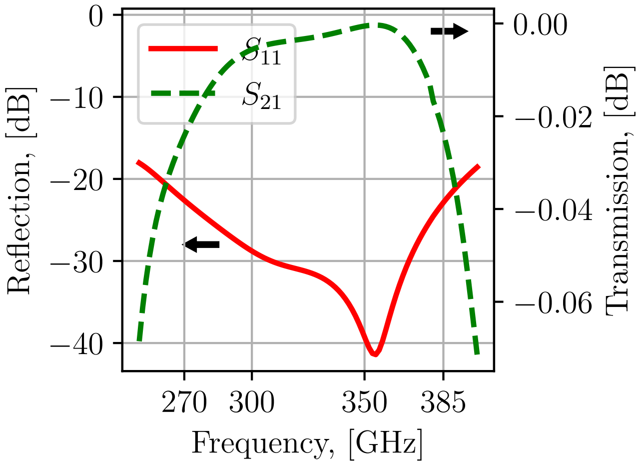

Figure 3.9: Power reflection and transmission after initial optimization of the transversal probe.

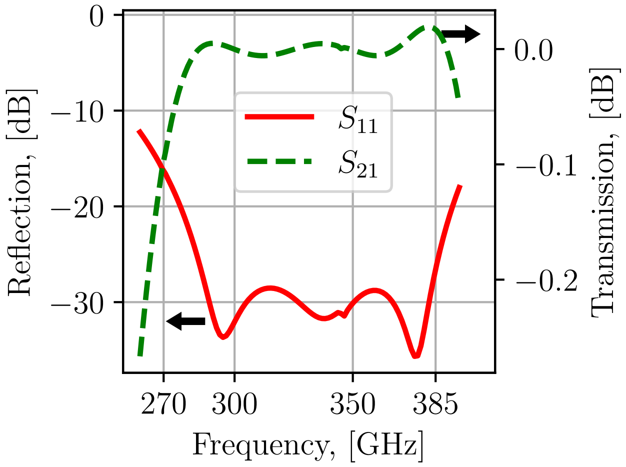

Figure 3.10: Power reflection and transmission after re-optimization using a re-normalized port impedance for the longitudinal probe.

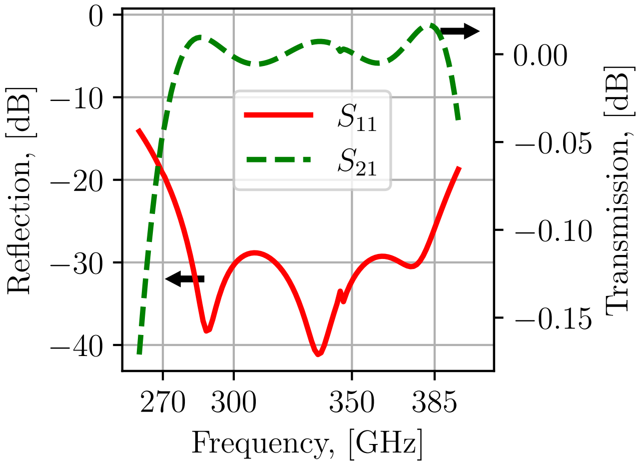

Figure 3.11: Power reflection and transmission after re-optimization using a re-normalized port impedance for the transversal probe.

3.1.3 Combiner design

The third component of the OMT is the combiners for the two outputs. From the theoretical considerations in section 2.4 there exist several designs that could work. For its simplicity and bandwidth, a model similar to the one in [57] was created, which is originally for 75 – 110 GHz. The model was then scaled by approximately 92.5 GHz/227.5 GHz $\approx$ 0.28. An illustration is shown in 3.12. The model was parameterized with the most important dimensions shown in figure 3.12 where there are three milled waveguide steps. The distance between the output ports were set to match the OMJ and RWG probe outputs. The model was parameterized with the angle of the outputs, α_{SWG}, the step lengths l_{s1}, l_{s2}, l_{s3} and the step widths b_{s1}, b_{s2}, b_{s3} shown in figure 3.12. The return loss at port 1 and the insertion loss from port 1 to ports 2 and 3 was optimized with the genetic algorithm and then a gradient algorithm in HFSS [2].

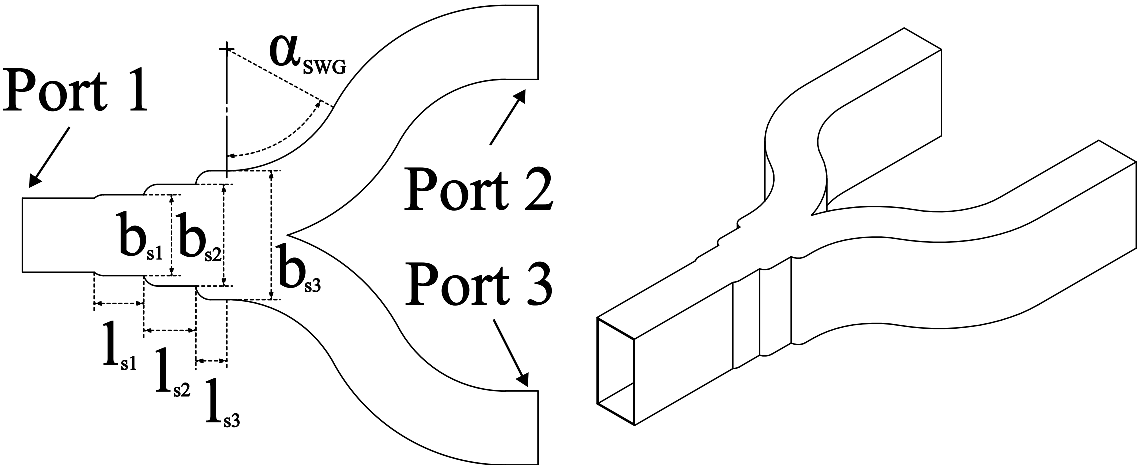

Figure 3.12: Combiner 3D model and inner top view. Its most important dimensions are annotated.

For the simple combiner optimized results for reflection and transmission are shown in figure 3.13. The return loss for the common port (port 1) is below −30 dB over more than the whole band and simulated insertion loss very low because of this. Reflection coefficients for port 2 and 3 is about −6 dB which is expected for this kind of combiner. In figure 3.14 the port isolation between port 2 and 3 is shown together with the transmission from the common port (port 1) to the other ports 2 and 3. The isolation is expected −6 dB and a close to equal power split is simulated.

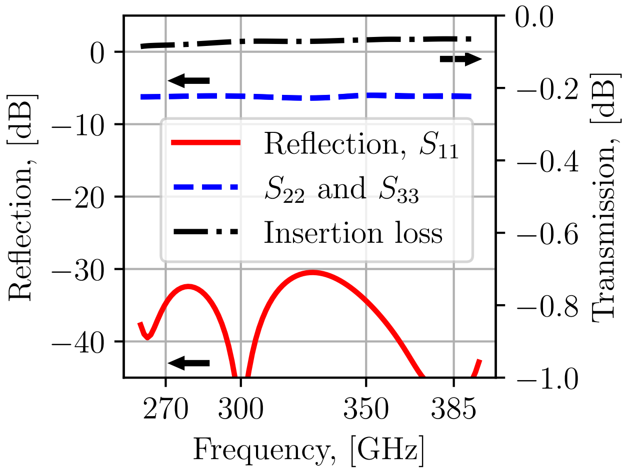

Figure 3.13: Optimized combiner power reflection and transmission results. The transmission is calculated as the total power transmitted 180° out of phase from port 1 to both port 2 and 3. This corresponds to the actual simulated insertion loss that this device would have if used in an OMT.

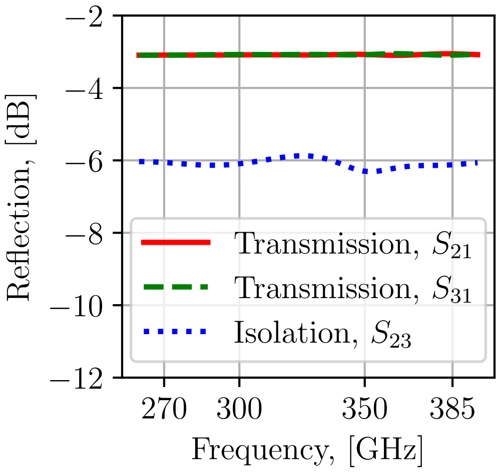

Figure 3.14: Optimized combiner power isolation and and transmission results.

3.1.4 Full orthomode transducer design

To assemble the full OMT consideration to the effect the different components have on each other needs to be taken into account. This was done by simulating the parts together in HFSS. The models obtained after the optimization of the OMJ and RWG probes were assembled as shown in figure 3.15. Dimensions were parameterized as shown in figure 3.5 where half of the thinfilm is shown. The probes laying in the transversal plane of the rectangular waveguide have the same dimensions and the two laying in the longitudinal plane have the same dimensions. All four probes in the circular waveguide have the same dimensions. The backshort distances in the circular waveguide (d_{bsOMJ}), waveguide leading to port 2 and 4 (d_{bsLP}), and waveguide leading to port 3 and 5 (d_{bsTP}) were also parameterized. These model dimensions were optimized with the genetic algorithm to maximize the return loss for polarization 1 and 2 in port 1, minimize the insertion loss from port 1, polarization 1 to port 3 and 5, and minimize the insertion loss from port 1, polarization 2 to port 2 and 4. The ports and polarizations are indicated in figure 3.15.

After an initial optimization, to center the design over the specified band-width, a feature called *Tune reports* in HFSS was used. The FEM solver of HFSS can be configured to calculate derivatives of scattering parameters with respect to the parameterized dimensions of the design [2]. In *Tune reports* it is possible to change the value of a dimension and view how the scattering parameters changes according to a interpolation using the derivative. The optimizer needs to simulate the whole geometry for each set of parameter values but with *Tune reports* it is possible to

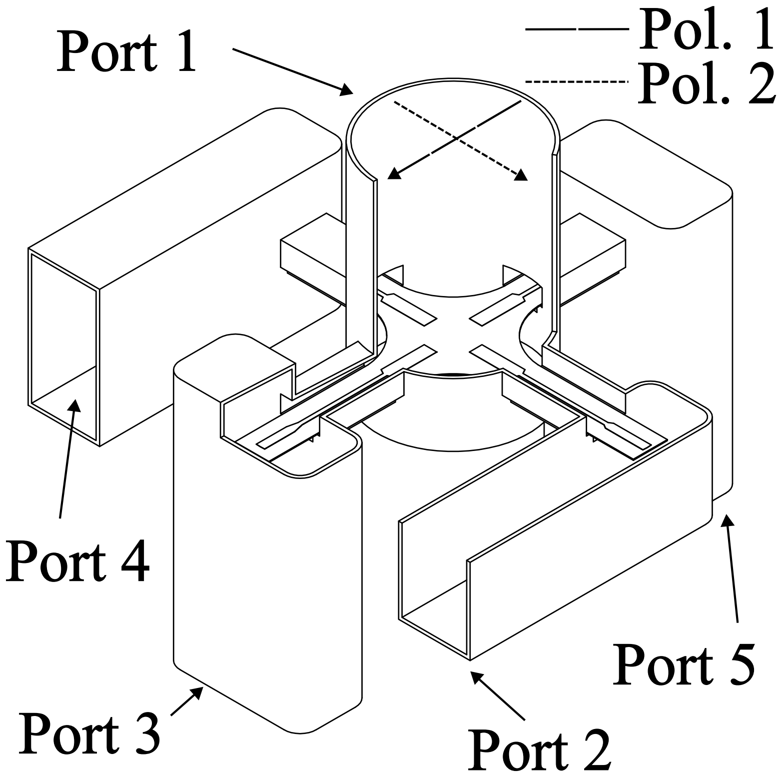

Figure 3.15: Model of the orthomode junction and RWG probes together. The direction of polarization 1 and 2 is indicated in port 1. Polarization 1 should couple to port 3 and 5 while polarization 2 should couple to port 2 and 4.

change the parameter values manually and approximate the change in scattering parameters. Because the optimizer had found parameter values close to the optimum *Tune reports* was used to center the design over the specified bandwidth.

An example of the tuning is shown in figure 3.16 where all parameters were changed by some small value. The solid lines are both polarizations reflection coefficients as simulated in HFSS. The dashed lines are the extrapolated results after a small change of one design parameter. For figures 3.16a-3.16c the lengths of orthomode junction, transversal probe and longitudinal probe have been increased by 10 µm. For figures 3.16d-3.16f the widths have been changed by 4 µm and for figures 3.16g-3.16i the backshort distances have been changed by 10 µm. One parameter was changed per figure and for the figures where only longitudinal probe dimensions change (figures 3.16a, 3.16d, 3.16g) the dimension only affects one of the polarizations as expected. When the dimensions of the orthomode junction probes or backshort is changed (figure 3.16c, 3.16f, 3.16i) both polarizations are affected.

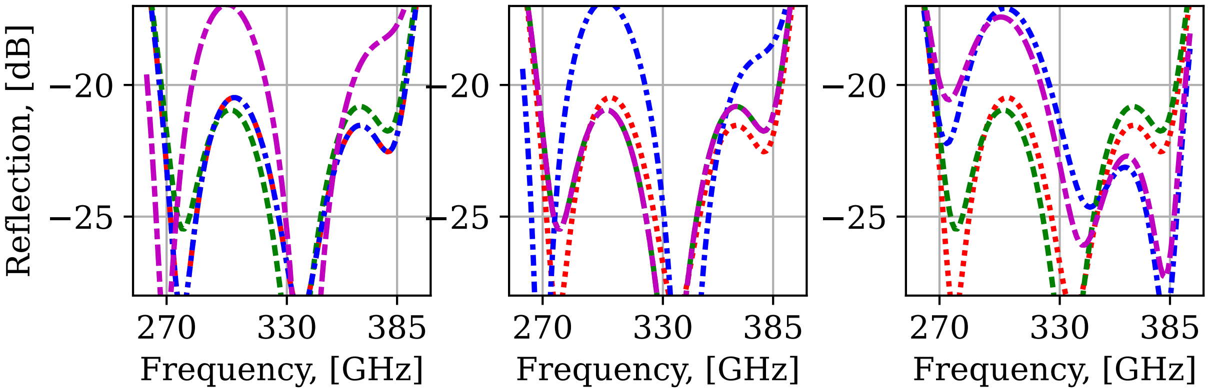

(a) Longitudinal probe length l_{LP} increased 10 µm (3.8%).

(b) Transversal probe length l_{TP} increased 10 µm (3.4%).

(c) OMJ probe length l_{OMJP} increased 10 µm (3.6%).

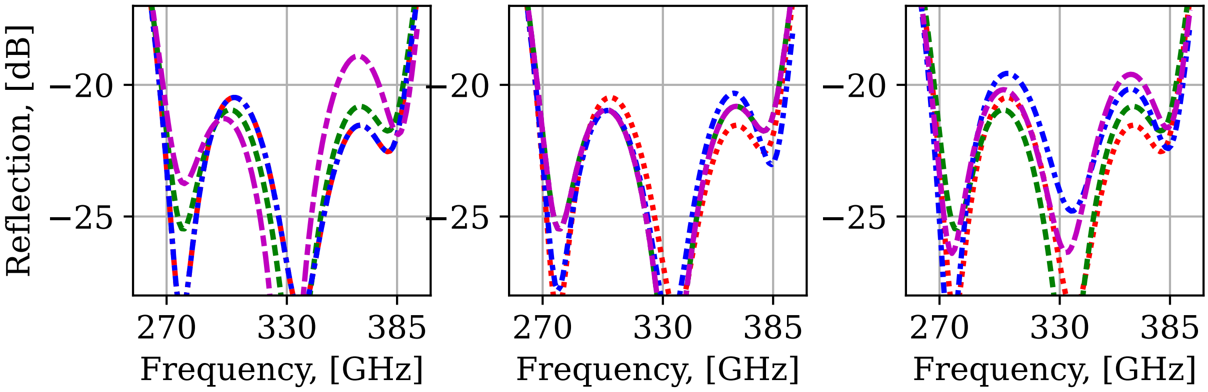

(d) Longitudinal probe width w_{LP} increased 4 µm (9.4%).

(e) Transversal probe width w_{TP} increased 4 µm (8.8%).

(f) OMJ probe width w_{OMJP} increased 4 µm (5.6%).

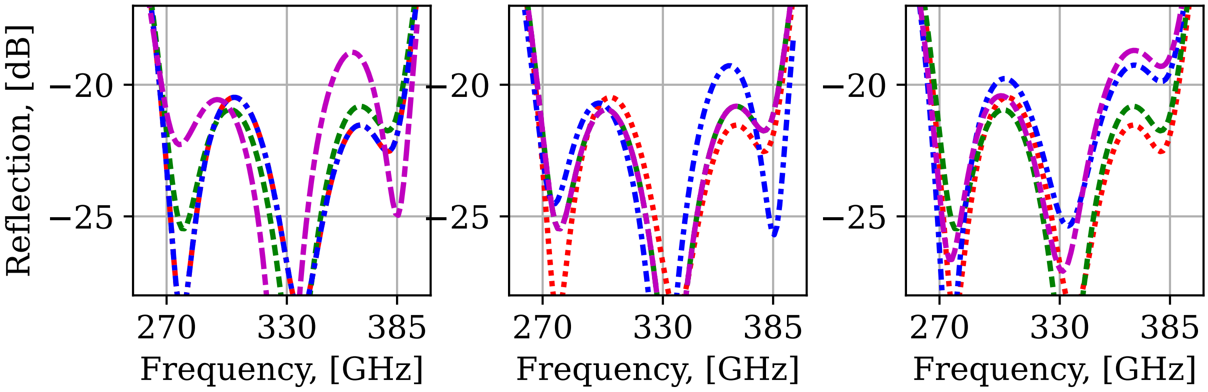

(g) Longitudinal probe backshort distance d_{bsLP} increased 10 µm (3.6%).

(h) Transversal probe backshort distance d_{bsTP} increased 10 µm (3.8%).

(i) OMJ backshort distance d_{bs} increased 10 µm (3.9%).

Figure 3.16: Graphs displaying the extrapolated change of reflection of the OMT with *Tune reports* in HFSS. The nominal curves are dotted lines, pol. 1 with short red dots and pol. 2 with longer green dots. The extrapolated curves are dash-dotted, pol. 1 with short blue dots and pol. 2 with longer purple dots.

Other conclusions drawn from the tuning are that increase in backshort distance and probe length seems to shift the lower frequency resonance to lower frequencies seen in figure 3.16a-3.16c. An increase in probe width however seems to shift the higher frequency resonance to higher frequency as seen in figure 3.16d-3.16f. Both widths and lengths of probes affect the middle resonance in some way.

By combining changes in all the dimensions re-tuning of the design can be done. Re-running the simulation for a set of changed dimensions and comparing to the corresponding extrapolated results showed that in the range of about 10%, the extrapolated results were similar to the simulated results. This proved very useful when some minor change needed to be done for the permittivity of gallium nitride for example.

The optimized OMJ together with RWG probe model results are shown in figure 3.17. Reflection of less than $-20\,\text{dB}$ is achieved over $280 - 390\,\text{GHz}$ and $-25\,\text{dB}$ over $285 - 372\,\text{GHz}$. After usage of *Tune reports* in HFSS the simulation results shown in figure 3.18 were acquired. The simulated return loss is more than $20\,\text{dB}$ over $265 - 388\,\text{GHz}$.

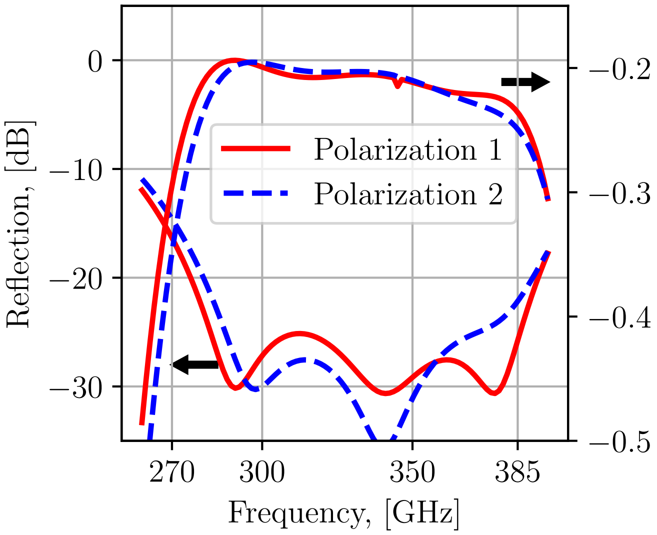

Figure 3.17: Optimized OMJ and RWG probe model (figure 3.15) power reflection and transmission simulation results. The return loss is high but the band is not as wanted.

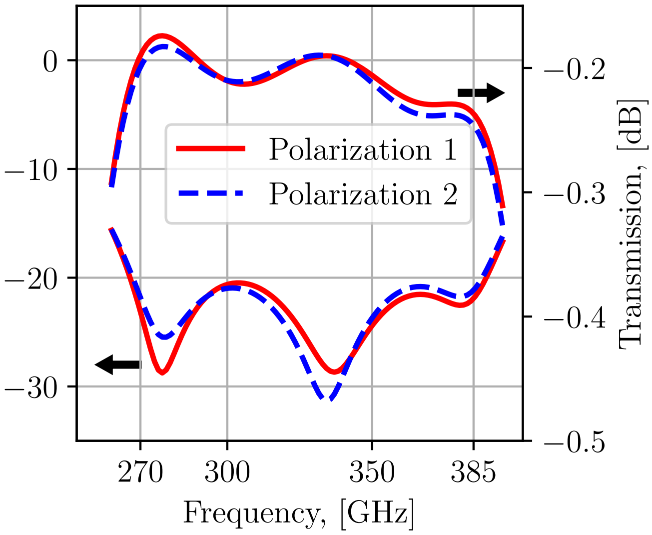

Figure 3.18: Tuned OMJ and RWG probe model (figure 3.15) power reflection and transmission simulation results. The band has been centered over the desired bandwidth.

After OMJ and rectangular waveguide probes simulated together to have return loss lower than -20 dB for both polarizations, the combiner models were added to combine ports 2 and 4, ports 3 and 5. This became the nominal design for GaN permittivity of $\epsilon_r = 7$. To be able to parameterize the block misalignment in simulation the model was split at the points where the actual block splits should be. A simplified and exploded view of the layout is shown in figure 3.19. These splits ensure all waveguides are split in the middle of the longer wall minimizing loss. Observe the small recess in the middle block in figure 3.19. The recess is to allow for easier mounting of the chip.

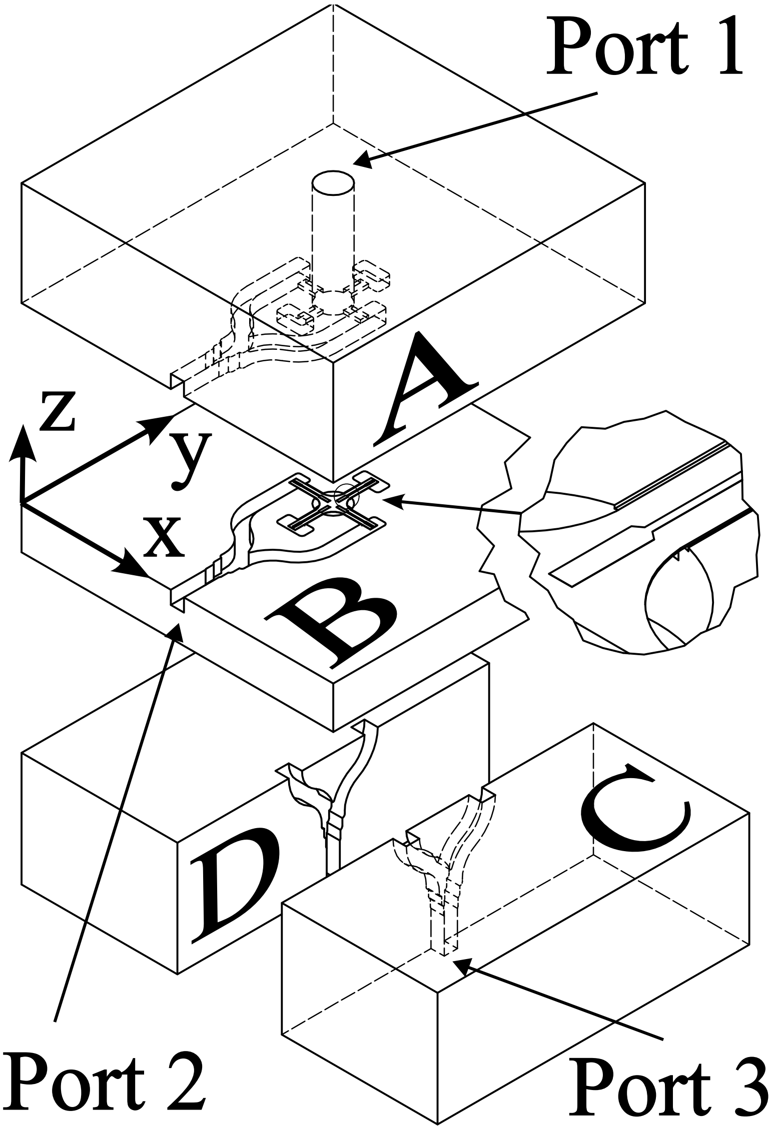

Figure 3.19: Layout of full OMT simulation model used for tolerance analysis and final simulations. Four metal blocks, A, B, C and D are indicated and a coordinate system for reference in tolerance analysis. Polarization 1 couples to port 3 and polarization 2 to port 2. The small cut-out on the right shows the small recess for the chip in block B.

3.2 Tolerance analysis and modifications of design

After creation of the full model, a tolerance analysis was run to see what accuracy of OMT assembly was needed and how the permittivity of GaN would affect performance. For reference the nominal simulation results of the whole OMT model is

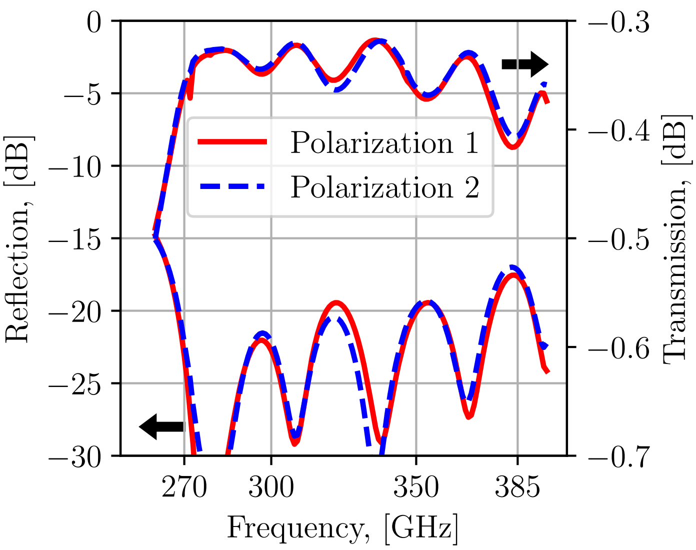

Figure 3.20: Nominal simulation results of the full OMT for $\epsilon_r = 7$ for GaN, other material parameters as default in HFSS [2]. Plotted are the reflected power (left axis) and transmitted power (right axis).

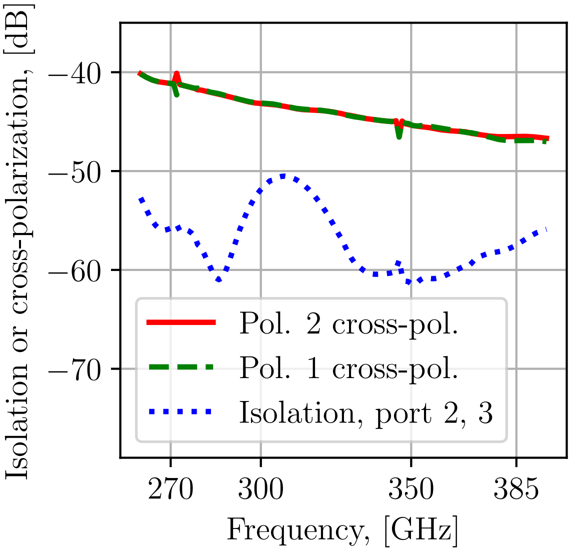

Figure 3.21: Nominal simulation results of the full OMT for $\epsilon_r = 7$ for GaN, material parameters as default in HFSS [2]. Plotted are the cross-polarization and isolation.

shown in figure 3.20.

For the model shown in figure 3.19, designed for GaN permittivity of $\epsilon_r = 7$, also $\epsilon_r = 7 \pm 1$ and $\epsilon_r = 7 \pm 2$ were simulated. The reflection and transmission of the OMT are plotted in figure 3.23 for $\epsilon_r = 7 \pm 1$ and in figure 3.23 for $\epsilon_r = 7 \pm 2$. For visibility, the nominal ($\epsilon_r = 7$) is only plotted in 3.22.

The actual value of GaN permittivity can be in the range of $\epsilon_r = 5 - 9$ for these frequencies. From the results in figure 3.22 and 3.23, the design is not tolerant enough to be finished without knowledge about the value of GaN permittivity. This motivated the measurements of GaN permittivity described in the methods section 3.3 for which results are presented in results section 4.1.

A tolerance analysis was also run on the misalignment of the chip compared to the blocks. The chip was moved ±15 µm in x and y direction in simulations as they are defined in figure 3.19. These results are shown in figure 3.24 where throughout the whole band, resonances have appeared. Observe that when movement is done in the x direction, resonances appear only for polarization 1. When movement in y direction is applied, only polarization 2 has resonances.

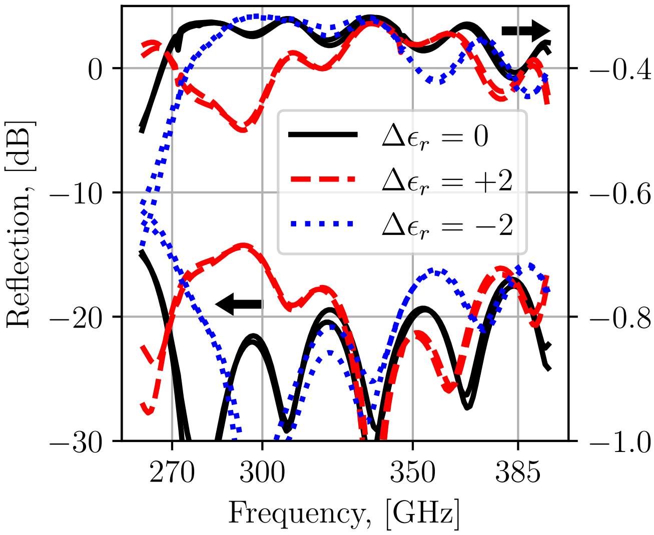

Figure 3.22: Initial tolerance analysis for the design for GaN $\epsilon_r = 7$. Reflection and transmission are plotted for $\epsilon_r = 7 \pm 2$.

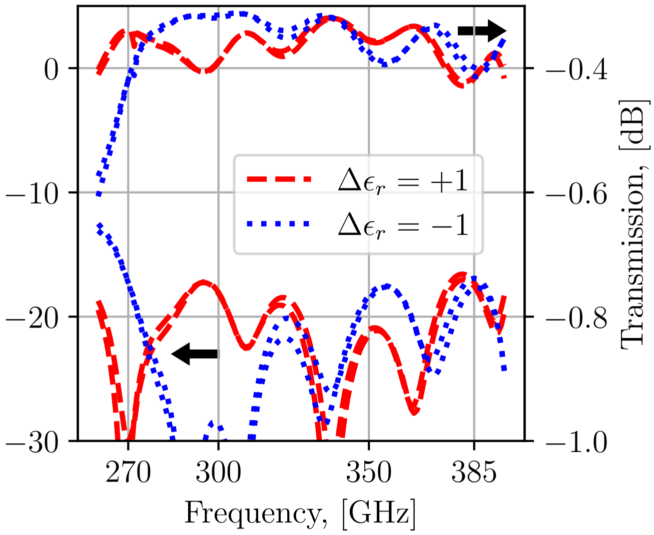

Figure 3.23: Initial tolerance analysis for the design for GaN $\epsilon_r = 7$. Reflection and transmission are plotted for $\epsilon_r = 7 \pm 1$.

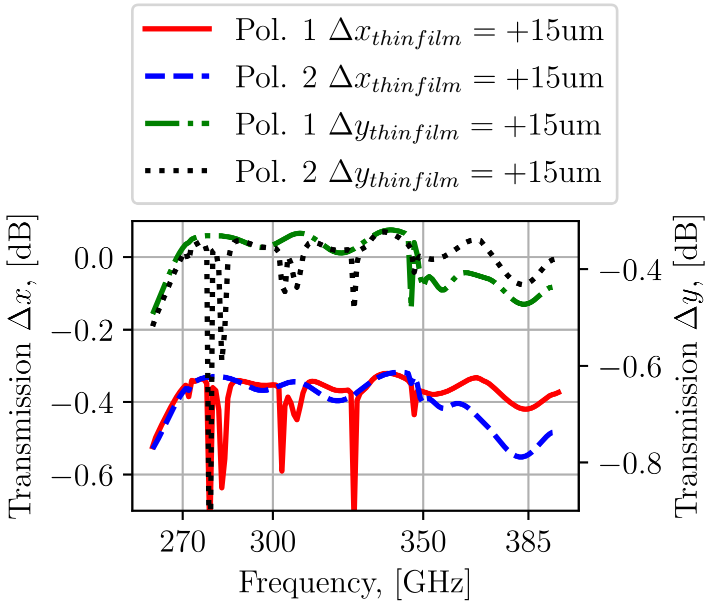

Figure 3.24: Initial tolerance analysis for the design for GaN $\epsilon_r = 7$. Transmission is plotted for thinfilm movement in x (lower graphs) and y (upper graphs) direction by 15 µm.

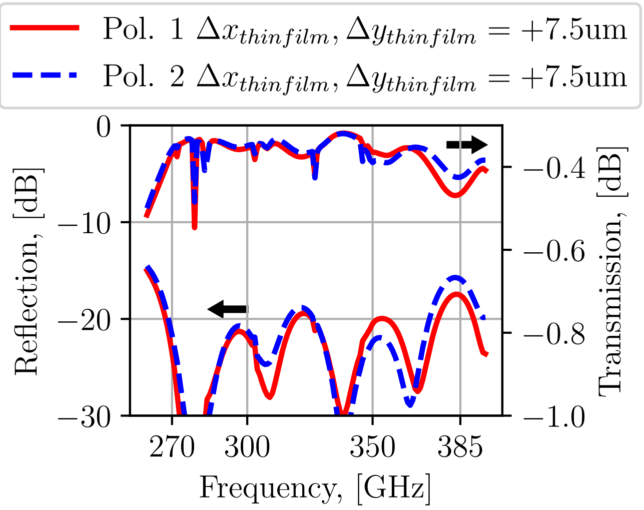

Figure 3.25: Initial tolerance analysis for the design for GaN $\epsilon_r = 7$. Reflection and transmission are plotted for movement in x and y direction by 7.5 µm. The depth of the resonance result in an insertion loss of about maximum 0.5 dB.

3.2.1 Possible solutions to thinfilm misalignment sensitivity

As seen in figure 3.25 alignment of ±7.5 µm could provide results that are good enough. The channel widths (w_{higher} in figure 3.2) had been set to 230 µm and the width of the thinfilm chip to 250 µm, which would permit only 15 µm movement of the chip in the channel. To enable better alignment, marks were added on the chip as shown in figure 3.28.

Another alternative solution was investigated but not implemented because of its complexity. By exporting the scattering parameters of the OMJ with RWG probes (figure 3.15) from HFSS into Keysight ADS [1] (ADS) it was possible to try what effect other combiners would have on the sensitivity to chip movement. Further details are given in appendix A. It was found that an alternative combiner can make the design more tolerant to movement of the chip but will complicate the OMT structure substantially. Therefore, the simple combiner was used as initially done.

3.2.2 Modifications after measurement of gallium nitride permittivity

After the measurements described in section 3.3, it was concluded that some re-designing was needed. The permittivity for GaN was set to $\epsilon_r = 8$ and the feature *Tune reports* was used to re-center the design. This process was the same as previously described in section 3.1.4.

Simulated reflection and transmission are shown in figure 3.26 for simulation with $\tan\delta = 0.18$ and $\tan\delta = 0.005$. With $\tan\delta = 0.18$ the loss of the device is about 3 dB, for $\tan\delta = 0.005$ however the insertion loss is about 0.04 dB. The return loss for $\tan\delta = 0.18$ is lower than for $\tan\delta = 0.005$ which could be an effect of the lossy material absorbing some of the energy otherwise reflected.

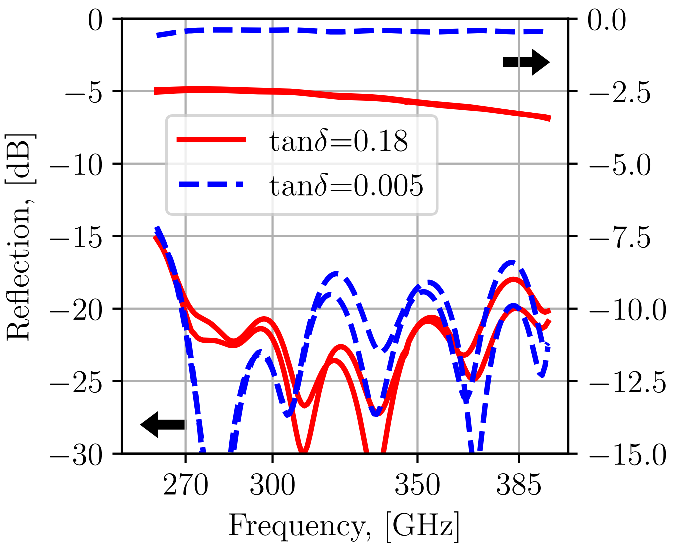

Figure 3.26: Chip alternative 1 nominal simulation results.

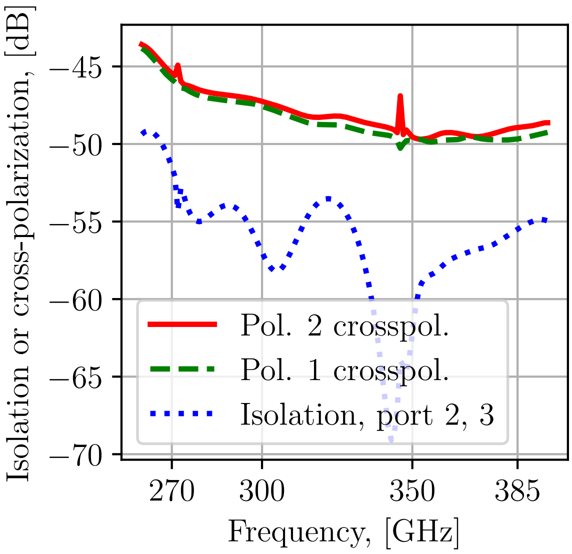

Figure 3.27: Chip alternative 1 nominal simulation results.

3.2.3 Chip manufacturability considerations

The thinfilm production process, described in section 3.4, which was based on photolithography allowed for several designs to be produced simultaneously. To minimize the risk of the thinfilm breaking upon mounting into the block three different designs were made, shown in figure 3.28. Another risk was that of chip deformation during production. To make the total deformation smaller the chip was divided as shown in figure 3.28, where chip alternatives 2 and 3 would have smaller deformation if the chips were bent.

The dimensions of the metal structures needed to be tuned with *Tune reports* in HFSS. Nominal return loss and insertion loss simulations for chip alternative 2 is shown in figure 3.29 and for chip alternative 3 in figure 3.30. The results are similar to that of chip alternative 1 in figure 3.26.

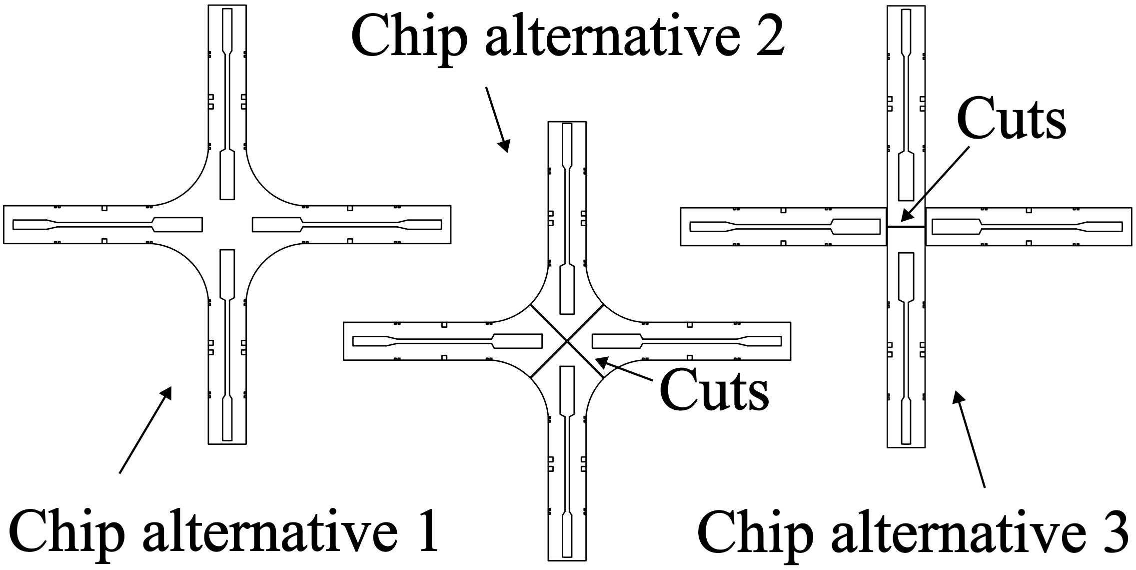

Figure 3.28: The three alternative thinfilm chip designs that were produced. Arms with two square markers go to longitudinal probes and arms with one square marker go to transversal probes.

Chip alternative 1 is the nominal alternative. It should have some self-aligning ability with respect to the block. There is however a risk that it could break because the chip is only 5.5 µm thick and could bend. Chip alternative 2 is similar to 1, however it is cut in four parts to minimize the risk of breaking and bending.

Chip alternative 1 and 2 have curved edges which require chip definition through photo-lithography. Chip alternative 3 is instead cut with straight edges, which means chip definition can be done using dicing (or sawing). When different chips were manufactured marks were added to distinguish between chips for longitudinal probes and chips for transversal probes.

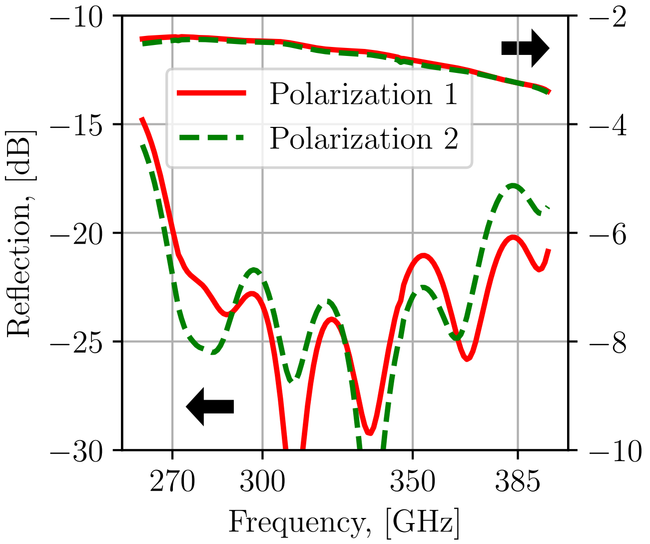

Figure 3.29: Chip alternative 2 nominal simulation results.

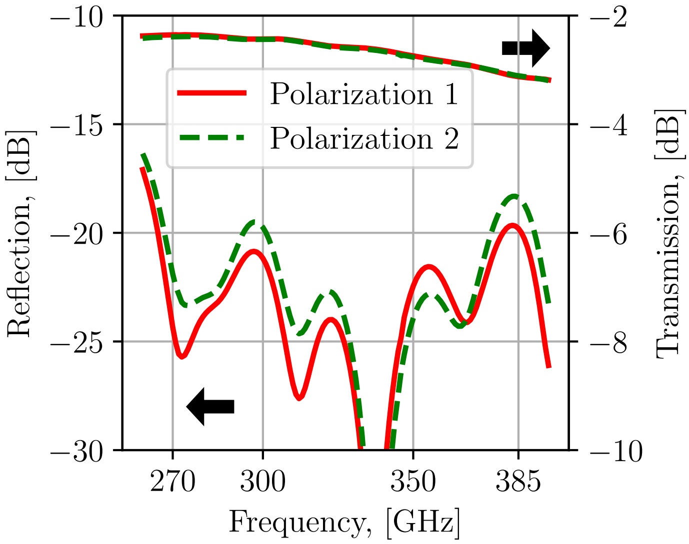

Figure 3.30: Chip alternative 3 nominal simulation results.

3.3 Characterization of gallium nitride

As motivated by section 2.5 and the tolerance analysis of the OMT performance with respect to the permittivity of GaN it was measured. The measurement method made use of a resonator structure described in [63], [68] and previously used for GaN permittivity measurements in [64]. The resonator was simulated in HFSS to ensure that GaN relative permittivity, ϵ_r, ranging from 5 to 9 would produce a measurable resonance in the band $220 - 330\,\text{GHz}$ because that is covered by only one type of VNA extender module [69]. The permittivity of GaN did in simulation shift the resonance in frequency while the loss tangent affected how pronounced the resonance appeared in the reflection measurements.

The resonator structure was constructed on a GaN substrate inserted into a waveguide for measurement, a method also used in [64]. The setup is illustrated in figure 3.31 where two split rings of 300 nm gold have been evaporated onto a 5.5 µm GaN substrate. The substrate in figure 3.31 sits in a 10 µm pocket milled from the lower waveguide block. The waveguide continues through the block so the setup become essentially a 2-port network.

The measurements were carried out by connecting two VDI WR3.4 VNA extender modules [69] to the two ports of the block shown in figure 3.31. There was also waveguide transitions added between extenders and the block. Full scattering parameters measurements were carried out and measured S_{11} and S_{21}. These were then imported into HFSS and simulations of S_{11} and S_{21} were fitted to the measurements. In the simulation model GaN relative permittivity, $\epsilon_r^{(GaN)}$, GaN loss tangent $\tan\delta^{(GaN)}$, gold conductivity σ_{gold}, aluminium conductivity σ_{alu} and waveguide length was changed to fit measurement with simulation.

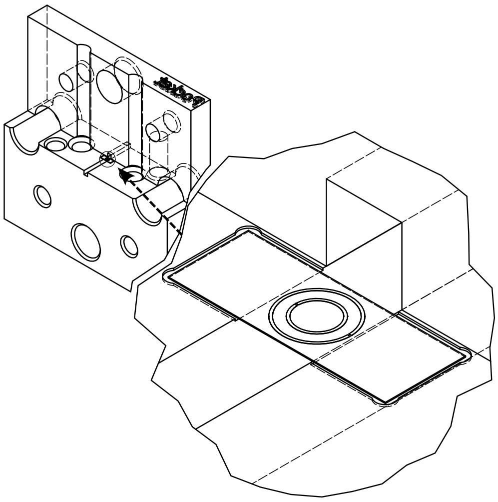

Figure 3.31: Illustration of the two-port waveguide block with the ring resonators on GaN substrate mounted.

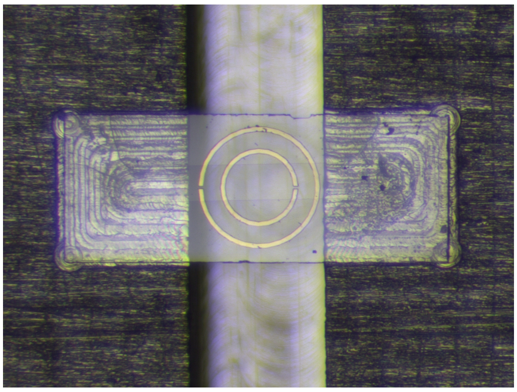

Figure 3.32: Top view of the ring resonator on GaN substrate mounted inside the waveguide.

3.4 Orthomode transducer production

A design of one block and three different chip layouts were produced. The block model was exported into Autodesk Inventor [70], waveguide flanges were added and the block was split in the mid-planes of output waveguides, the same splits as illustrated in figure 3.19. The thinfilm chips shown in figure 3.28 were produced in the clean-room at Chalmers.

3.4.1 Block manufacturing

The block was manufactured at GARD at Chalmers with the use of a CNC milling machine. The smallest mill used was 150 µm in diameter because of the smallest dimension being the lower channel width. Flanges of standard type UG-387/U were added. These are the same flanges as both standard WR3.4 (IEEE WM-864 [71]) and WR2.2 (IEEE WM-570 [71]) use. Guiding pins to align the different parts of the block were added at the furthest possible distances to give the highest alignment accuracy. Furthermore, several screws between all blocks were added and at the split interfaces recesses were introduced to enable better contact between waveguide split blocks. An exploded view is shown in figure 3.33 where some of the pins, screws, recessed surfaces and ports are indicated.

3.4.2 Thin film manufacturing

Thin-film manufacturing of the layouts shown in figure 3.28 was done using a process using two photo-lithographies similar to the process described in [64]. The process was based on a 1000 µm thick Si wafer with a 3 µm AlGaN buffer-layer and a 2.5 µm GaN layer. The wafer of size 1 inch × 1 inch was packed with the three designs from

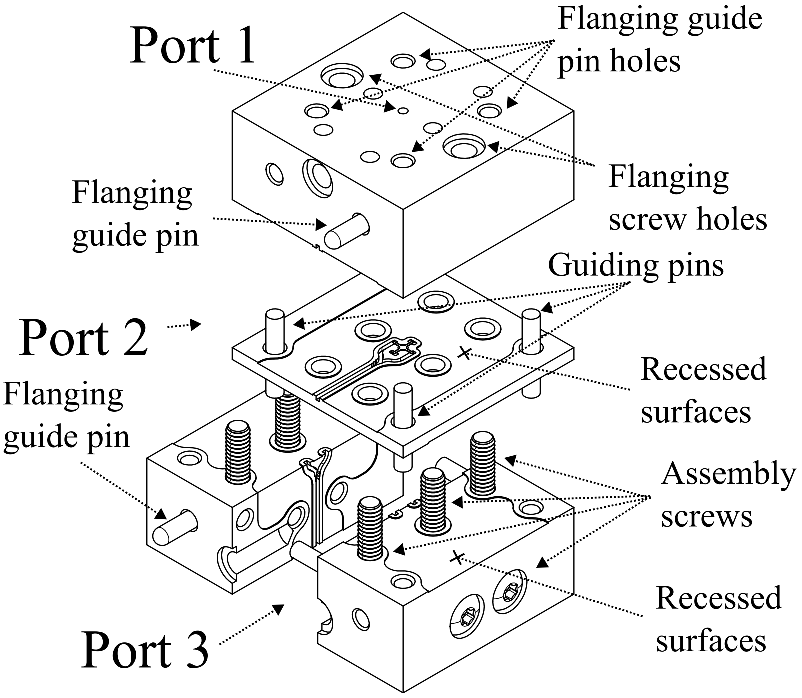

Figure 3.33: Exploded view of the manufactured block with screws, guiding pins for assembly, recesses and waveguide flange layout.

figure 3.28. Chip alternative 1 and chip alternative 2 both required two lithographies, the first for definition of the Au metal structures and the second for definition of chip structures. Chip alternative 3 required one lithography for the metal definition, the chip structure definition was done using dicing instead.

The full process is illustrated in figure 3.34 for chip alternatives 1 and 2. Positive resist of thickness 1.3 µm is used for the first lithography shown in figure 3.34a-3.34c. A 10 nm thick adhesion layer of Ti was deposited after which a 500 nm thick Au layer was deposited, shown in figure 3.34d. After lift-off (figure 3.34e) another layer of positive resist of thickness 9 µm was deposited. Another lithography was carried out to etch away GaN/AlGaN for definition of chips shown in figures 3.34f-3.34h. Reactive-ion etching was used to etch the GaN in figure 3.34i where-after the resist was cleaned away. The piece was now diced in quarters out of which two were shared by chip alternative 1 and 2. The other two quarters contained chip alternative 3 devices. For the separate quarters, the backside etching illustrated in 3.34j-3.34l was done.

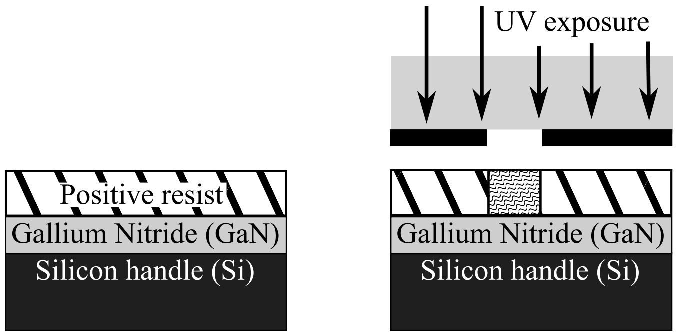

(a) Positive resist of thickness 1.3 µm is deposited on the sample.

(b) Sample exposed by UV to make exposed parts soluble, mask is dark-field.

(c) Resist development remove soluble part of resist.

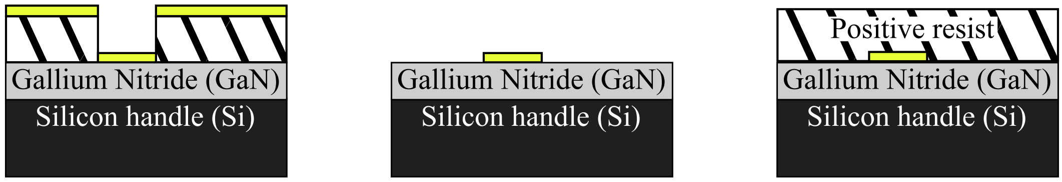

(d) Deposition of titanium and gold metal layers.

(e) Lift-off by dissolving resist layer in acetone with ultra-sonic vibrating.

(f) Positive resist of thickness 9 µm is deposited on the sample.

(g) UV exposure through clear-field mask to make exposed parts soluble.

(h) Resist development.

(i) Reactive-ion etching to etch GaN.

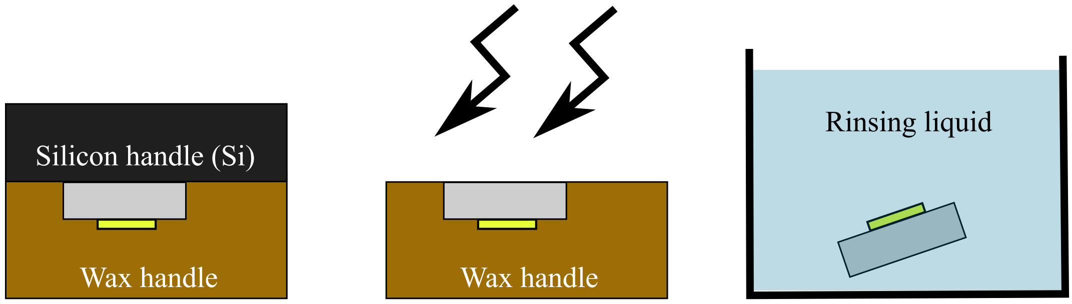

(j) Remounting of sample on wax handle.

(k) Deep silicon etching.

(l) Cleaning and extraction of samples with remover liquid.

Figure 3.34: Description of the thin-film production process. The layer thicknesses are not to scale.

3.5 Orthomode transducer characterization

The characterization sought to measure the full scattering matrix of the orthomode transducer described in section 2.2.1. A VNA [72] was used with millimeter wave extender modules for the frequency ranges 220 – 330 GHz [69] and 330 – 500 GHz [73] corresponding to the waveguide standards WR3.4 (IEEE WM-864 [71]) respective WR2.2 (IEEE WM-570 [71]). The orthomode transducer is designed for the frequency range of 270 – 385 GHz and a waveguide size of 380 × 760 µm (here called WM760) for which no extender module is available. The measurements were therefore done with both WR2.2 and WR3.4 extender modules and transitions to WM760 were used around the OMT. After measurements the data was stitched together. A figure describing the symbols used in this thesis to describe measurement setups is shown in figure 3.35 where the transitions from WR2.2 or WR3.4 (called WRXX) to WM760 is shown.

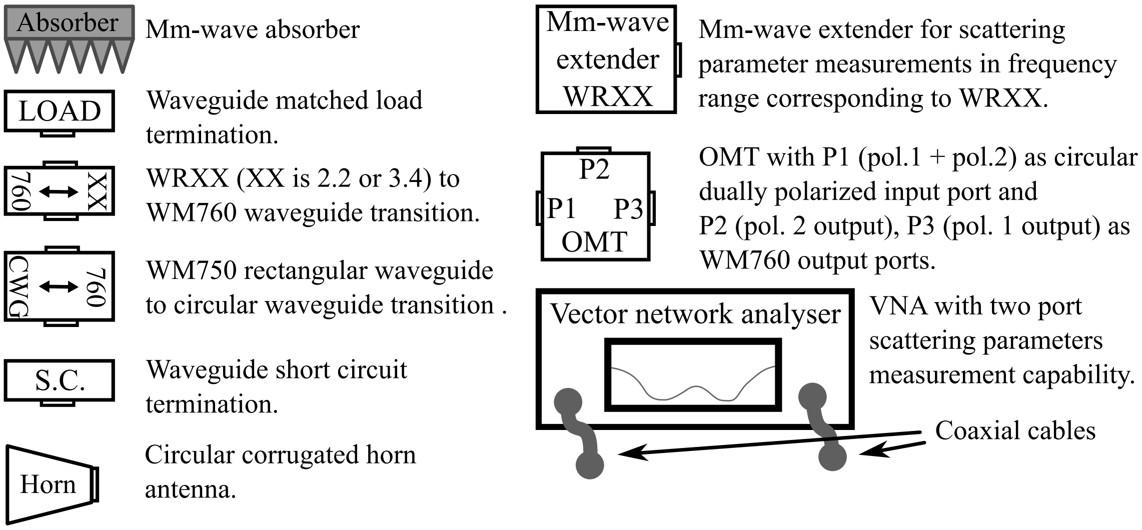

Figure 3.35: Illustration of devices used in the measurements.

The physical port 1 for the OMT in figure 3.35 is input to both polarization 1 and 2. The port is a circular dually polarized waveguide port which means the orientation of the port will define which polarization is excited in P1. A WM760 to circular waveguide (CWG) transition was used to excite either polarization 1 or 2 in P1 of the OMT depending on the rotation of the transition. Polarization 1 is expected to mostly couple to P3 and polarization 2 to P2.

3.5.1 Input return loss and insertion loss

To measure return loss and insertion loss for polarization 1 the setup shown in figure 3.36 was used and for polarization 2 the setup shown in figure 3.37. From the definition of scattering parameters, all other ports should be matched when measurement of return loss is carried out. For insertion loss measurements, the ports not being measured insertion loss between should be matched. As described in detail in [43] the WM760 to CWG adapter will not create a perfect match for the cross-polarization. This gives rise to errors which needs to be taken into account when characterizing the OMT.

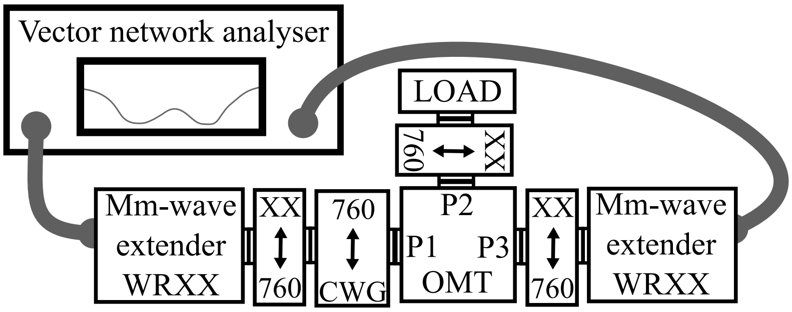

Figure 3.36: Measurement setup for measurement of input return loss and insertion loss for polarization 2. The transition from WM760 to CWG is rotated to that it couples to polarization 2 in the OMTs P1. Polarization 2 in P1 is expected to mostly couple to P2.

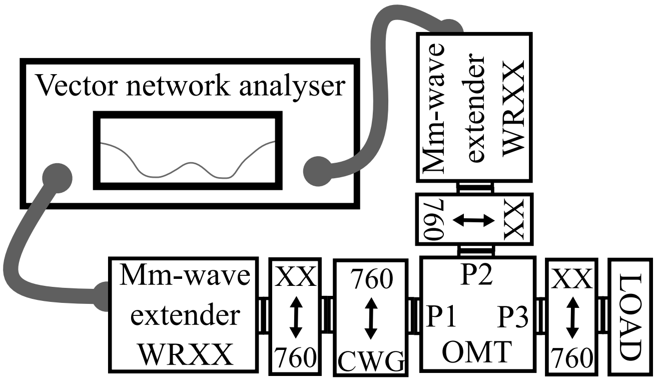

Figure 3.37: Measurement setup for measurement of input return loss and insertion loss for polarization 1. The transition from WM760 to CWG is rotated to that it couples to polarization 1 in the OMTs P1. Polarization 1 in P1 is expected to mostly couple to P3.

The WM760 to CWG adapter cross-polarization coupling which will affect input return loss measurements. If the cross-polarization is assumed to be $-30\,\text{dB}$ and the return loss to be $-20\,\text{dB}$ the largest error will be from the wave first cross-coupling, reflected and then cross-coupled back, having magnitude $-80\,\text{dB}$. The other reflections will be even lower which means an expected input return loss level of $-20\,\text{dB}$ would be accurately measurable.

For the insertion loss measurements, the cross-polarization of the adapter will also affect the measurements. The largest error will come from the wave coupled to the other polarization input because of WM760 to CWG cross-polarization (assumed $-30\,\text{dB}$). This wave will then couple back through the OMTs cross-polarization (assumed $-30\,\text{dB}$). This means the largest error will be $-60\,\text{dB}$ compared to the expected measured transmission of about $-0.5\,\text{dB}$, so the error is negligible.

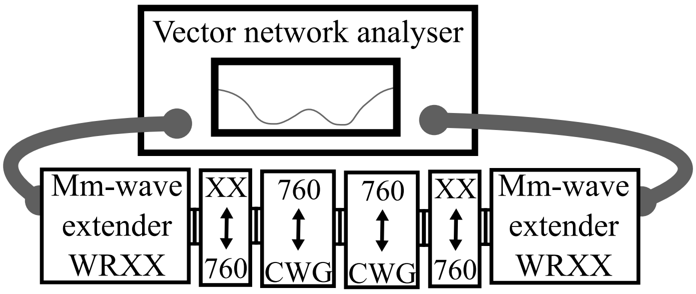

Figure 3.38: Setup of measurements to de-embed the OMT from transitions from WR2.2 or WR3.4 to circular waveguide. The WM760 to CWG transitions were rotated to both measure when the two ports couple via the same polarization and orthogonal polarizations.

3.5.2 Cross-polarization, isolation and output return loss

The setup shown in figure 3.36 and 3.37 could in theory be used for measurements of OMT cross-polarization. This setup would use the WM760 to CWG adapter rotated to couple to the polarization corresponding to the load output. In figure 3.36 the adapter would be connected to excite polarization 2 (polarization mostly coupled to P2) for example. The largest error would be from the wave coupled through the cross-polarization of the adaptor (assumed $-30\,\mathrm{dB}$) and then coupled by the transmission (assumed $-0.5\,\mathrm{dB}$) through the OMT. Because the measured OMT cross-polarization is assumed to be in the order of $-30\,\mathrm{dB}$, then the error has the same magnitude as the measured quantity. Cross-polarization of the OMT is therefore not accurately measurable with this method if not the adapter cross-polarization is lower or only a higher bound of cross-polarization is sought after.

Another method for measurement of OMT cross-polarization is described in [43] and shown in figure 3.39. The extenders are connected to P2 and P3 and P1 is terminated with a short circuit. A schematic view of the setup is shown in figure 3.40 to visualize the contributions. The total transmission from P2 to P3 will consist of large number of reflections, however all except the three signal paths indicated in 3.40 by three different line styles will be negligible. Two paths are coupled through either P3 to P1, pol.2 cross-coupling or P1. pol.1 to P2 cross-coupling. One contribution is the direct through the direct ISO path in figure 3.40. Depending on the value of isolation, cross-polarization for the OMT can be deduced from this measurement. The isolation can be subtracted from the measured transmission from P2 to P3. Half of that quantity should then be cross-polarization.

The setup for measuring isolation is shown in figure 3.41. A horn directed at an absorber is connected to P1 to terminate P1 in a matched load. With a reflection coefficient of about $-20\,\mathrm{dB}$ for the horn and assumed cross-polarization of the OMT of about $-30\,\mathrm{dB}$ the largest error when measuring isolation would be about $-50\,\mathrm{dB}$. Isolation is expected to be as low as $-50\,\mathrm{dB}$ which would make it hard to make accurate measurements of isolation, however an estimate can be obtained.

The setup in figure 3.41 can also be used to measure output return loss of the OMT.

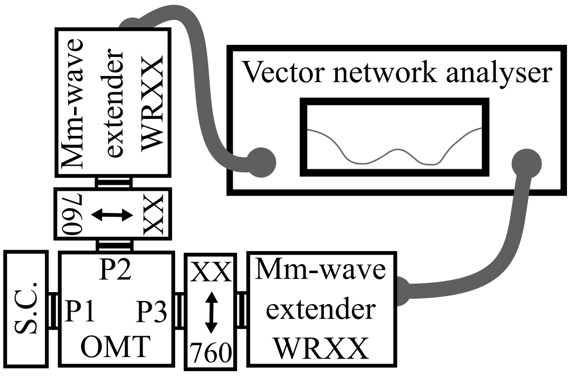

Figure 3.39: Cross polarization measurement setup. A short circuit waveguide termination is connected to P1 of the OMT to short both polarizations.

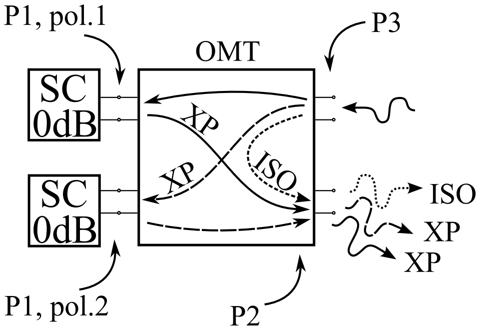

Figure 3.40: Schematic description of contributions to measurement of cross-polarization. A short circuit waveguide termination is connected to P1 of the OMT to short both polarizations.

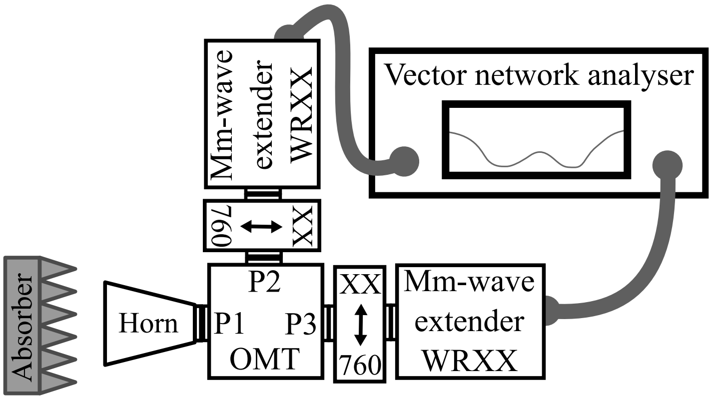

Figure 3.41: Measurement setup for output return loss measurements and output port isolation measurements. A radiating horn is connected to P1 of the OMT to match P1 for both polarizations.

4

Results and discussion

This chapter deals with results for material parameters, produced orthomode transducers and measured performance of these. Some short discussion is held at the respective results. A more thorough discussion is done in section 4.4 to enable discussion of both material parameters, production process and measured OMTs simultaneously.

4.1 Characterization of gallium nitride

Gallium nitride permittivity was measured by fitting simulation with measured data of the resonant rings. The measured and best fitted simulation is shown in figure 4.1. For the best fitting between simulation and measurement the swept parameter values were, $\epsilon_r = 8$, $\tan\delta = 0.18$, $\sigma_{gold} = 4.4 \cdot 10^7$ S/m and waveguide length of about 10 mm. When sweeping the parameter values manually, a rather good fit was attained for $\epsilon_r = 7.8$, $\tan\delta = 0.005$, $\sigma_{gold} = 1 \cdot 10^7$ S/m and waveguide length of about 10 mm shown in figure 4.2. For the fitting results, ϵ_r has a similar value for both fitted simulations, however, the $\tan\delta$ and σ_{gold} are profoundly different.

To accurately predict $\tan\delta$ is not seen as possible from these measurements because of the different possible values of gold conductivity. Relative permittivity of GaN however is found to be close to $\epsilon_r \approx 8$ for this frequency range because the similarity of ϵ_r for the two fitted data.

To investigate the certainty of the fitting of simulation to measurements the fitting parameters ϵ_r, $\tan\delta$ and σ_{gold} were also swept in simulation. Results for $\epsilon_r = 8 \pm 1$ are shown in figure 4.3, for $\tan\delta = 0.18 \pm 0.1$ in figure 4.3 and for $\sigma_{gold} = 4.4 \cdot 10^7$S/m, 10^7S/m in figure 4.5. As seen from figure 4.3, it is probable that ϵ_r is measured with an uncertainty of less than ±1 at most. Variations in ϵ_r also change the depth of the resonance somewhat, another observation that makes the extraction of $\tan\delta$ more difficult. Both variations in $\tan\delta$ and σ_{gold} shift the depth of the resonance from figures 4.4 and 4.5. There is no resonance shift in frequency for σ_{gold} and only a small shift for $\tan\delta$, which further suggest that mostly ϵ_r affect the resonance frequencies. This adds to the conclusion that ϵ_r for GaN is about 8 at these frequencies.

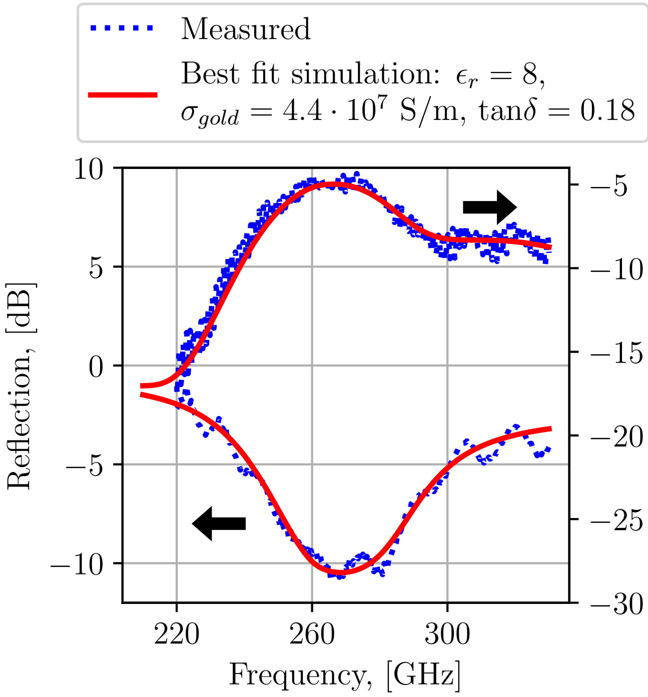

Figure 4.1: Best fitting of simulations to measurement with respect to the fitting parameters, ϵ_r, $\tan\delta$, σ_{gold} and waveguide length.

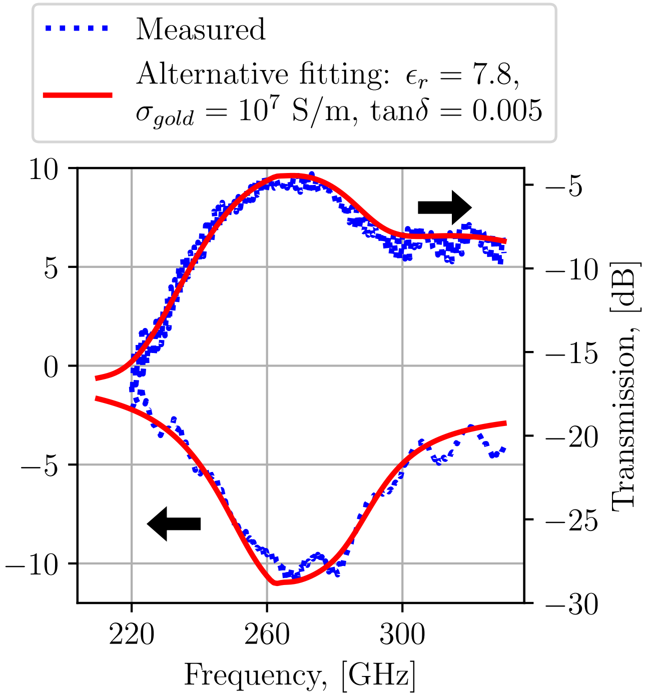

Figure 4.2: Alternative fitting of simulations to measurement with respect to the fitting parameters, ϵ_r, $\tan\delta$, σ_{gold} and waveguide length.

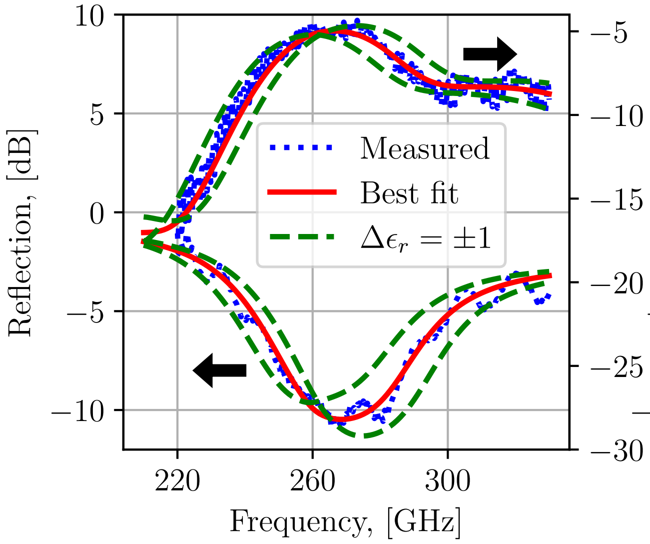

Figure 4.3: Measured results, simulated best fit results and results with ϵ_r changed ±1 for the ring resonator reflection and transmission.

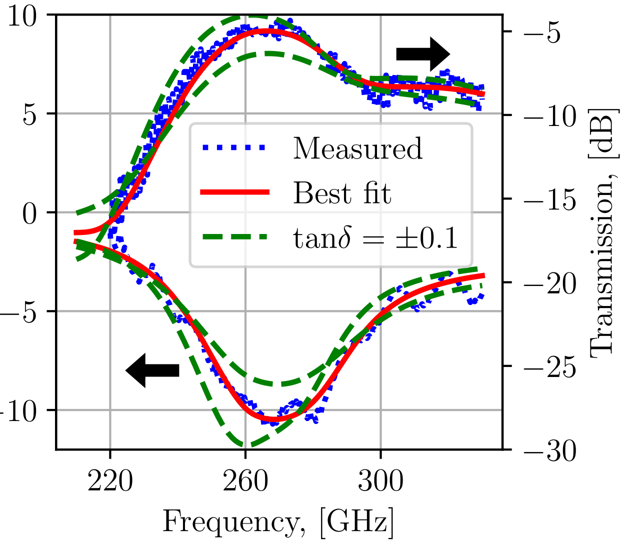

Figure 4.4: Measured results, simulated best fit results and results with $\tan\delta$ changed ±0.1 for the ring resonator reflection and transmission.

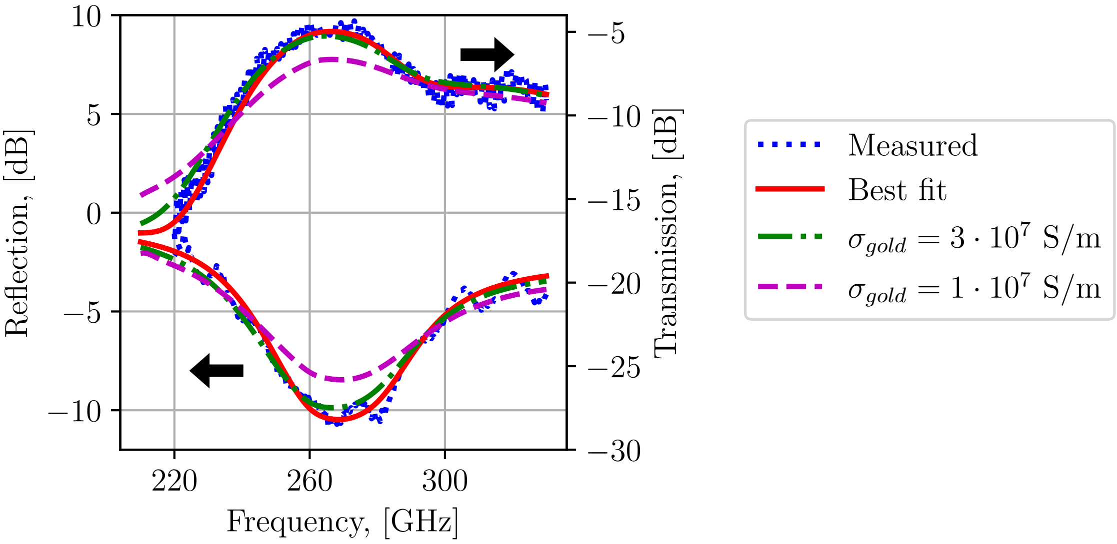

Figure 4.5: Measured results, simulated best fit results and results with σ_{gold} changed to $3 \cdot 10^7$S/m and 10^7S/m for the ring resonator reflection and transmission.

4.2 Produced OMT devices

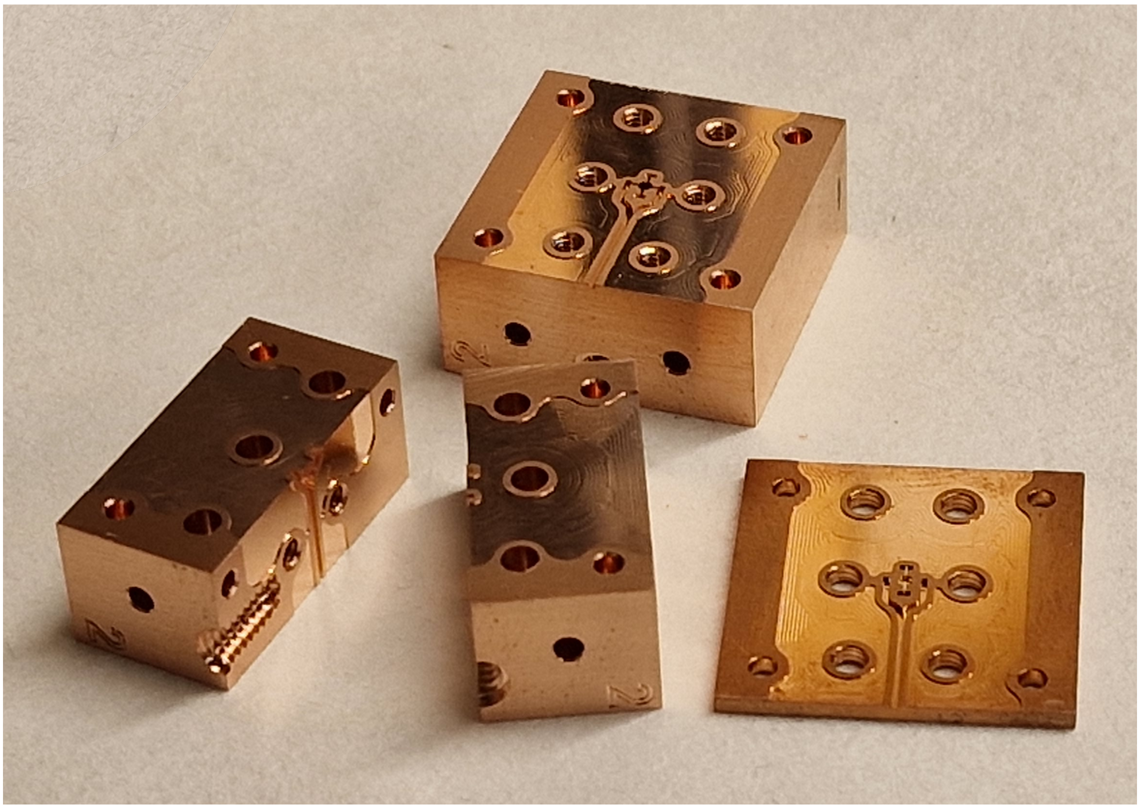

Figure 4.6: Picture of one set of produced block parts. There was also a second, identical block, produced.

A picture of the produced OMT block parts is shown in figure 4.6. As earlier, the block parts are called block A, B, C and D as shown in figure 3.19. Two OMT devices were fabricated and therefore also two sets of the blocks shown in figure 4.6. The dimensions of the parts were measured with *ZeGage* optical profilometer [74]. As a result of fabrication uncertainties, discrepancies from the model were found at the channel widths (w_{upper}) for block part B which were about 15 µm narrower than expected. The margin on each side of the chip was then only about 7.5 µm or less which made chip mounting challenging. On the other hand, the alignment was more accurate because of the smaller channel width.

The recess for the chip was also found to be 5 µm deep instead of 10 µm. When applying glue under the chip, the chip protruded above the surface of block part B. The upper channel width (w_{upper}) in block A was however about 235 µm wide which gave about 17 µm of margin on each side of the chip. This allowed for the chip not to be crushed when block parts A and B were assembled.

Chip alternative 1 was mounted in block part B, which is shown in figure 4.7. As seen from the top, chip alternative 1 aligned well in the channels. During mounting the chip was seen to be almost self-aligning in the channels because of the beams being connected. A scan with the *ZeGage* profilometer showed that the chip was bent and only touched the block at the four RWG probes as seen in figure 4.8. The

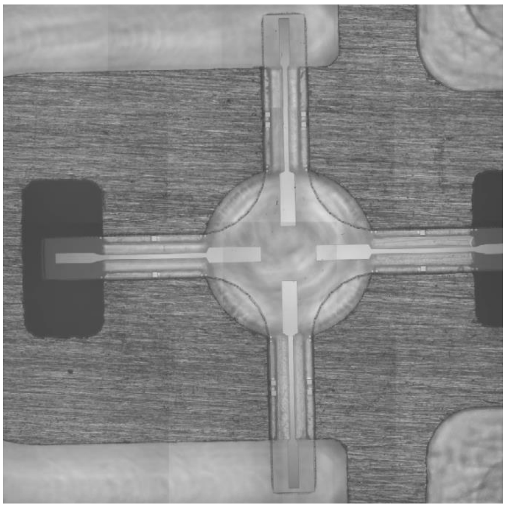

Figure 4.7: Top view of the placed but not glued chip alternative 1 to block part B.

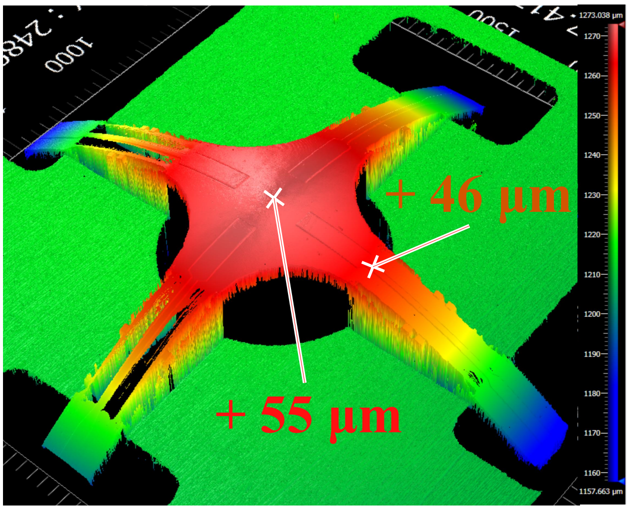

Figure 4.8: Profilometer scan image of chip alternative 1, placed in block part B. The colors indicate height. The height of the chip in the 3D picture is not to scale and somewhat exaggerated for visibility.

height of the chip was 46 µm at the channel opening into the circular waveguide and at most 55 µm over the block. Gluing of this chip to the block was therefore difficult to do without breaking the chip, which is why no device was fully assembled with chip alternative 1. If possible however, either by mitigating chip bending or careful mounting, the self-aligning feature of the chip would be preferred.

Chip alternative 2 was mounted in another block part B as shown in figure 4.9. The chip bending from alternative 1 was also present here, however, because of the chip's smaller size, the chips could rest in the channels better. Magnified pictures of the RWG probes and alignment marks are also shown in figure 4.9, alignment marker size is 10 µm × 10 µm with a distance of 10 µm between the markers. Alignment accuracy of ±5 µm can therefore be observed. The alignment marks at the circular waveguide were all misaligned with about 15 µm. One reason for this misalignment could be the bending of the chips. Another possible reason could be the more limited accuracy of the block manufacturing.

Chip alternative 3 mounted in another block part B is shown in figure 4.10. As seen in the figure, the dicing process made the sides of the chip uneven and not all alignment markers were preserved. With the remaining alignment markers however, good alignment was achievable. The longitudinal RWG probes are misaligned by about $5-10$ µm and the transversal with less than ±5 µm. As for chip alternative 2 the alignment marks in the circular waveguide hole are misaligned by about 15 µm. Similarly, this could be a result of chip bending and block manufacturing inaccuracy.

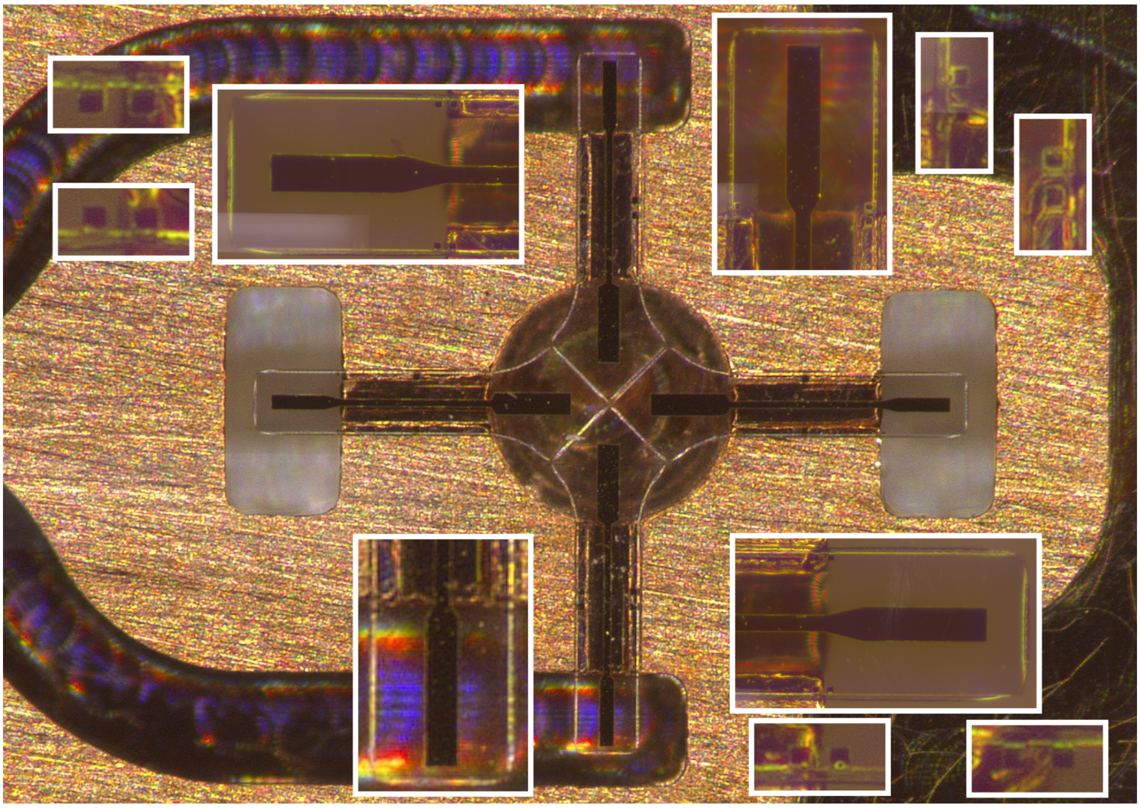

Figure 4.9: Chip alternative 2 mounted in block part B. Alignment marks are shown in magnified views. Alignment marker size is 10 µm × 10 µm with a distance of 10 µm between the markers.

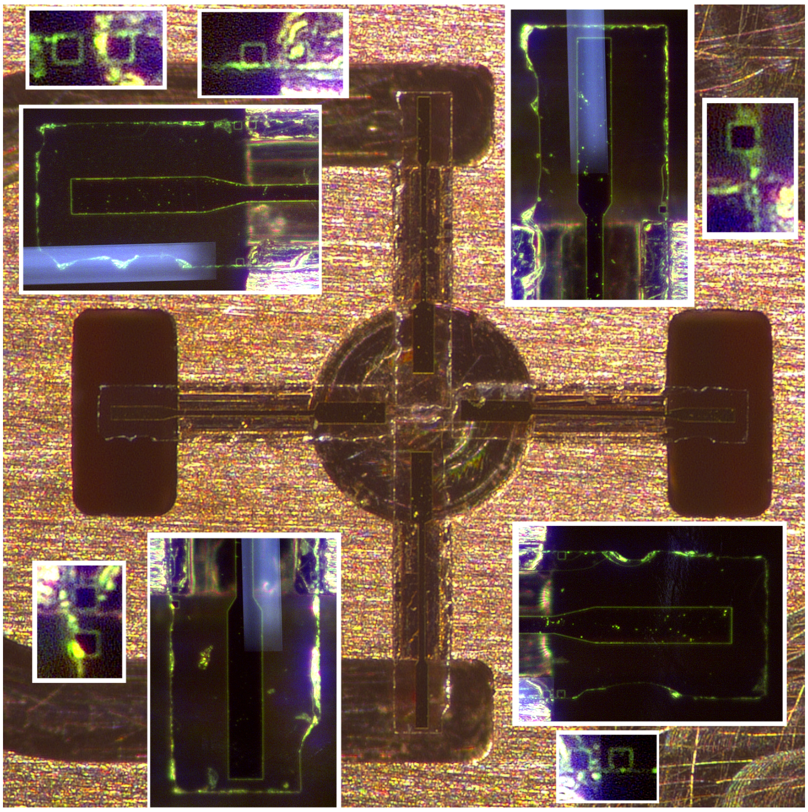

Figure 4.10: Chip alternative 3 mounted into block part B. Several alignment marks were destroyed in the dicing fabrication process, the remaining marks are shown as cut-outs. Alignment marker size is 10 µm × 10 µm with a distance of 10 µm between the markers.

4.3 Measurement results

In this section, measurement results of OMT devices are presented. A deeper discussion of the results is done in section 4.4.

Chip alternatives 2 and 3 were mounted, as shown in figures 4.9 and 4.10, and the blocks were assembled. The misalignments estimated from microscopic measurements were implemented into HFSS and models re-simulated for both chip alternative 2 and 3 and the two fitted sets of material parameters of figures 4.1 and 4.2.

Gold DC conductivity was also measured using test structures on the same batches as chip alternative 2 and 3 using a similar method as [75]. Before the back-side Si etching process described in figure 3.34k, σ_{gold} was measured to $4.8 \cdot 10^7$S/m and $5.25 \cdot 10^7$S/m for two different test structures. After the etching process, measured conductivity was $0.82 \cdot 10^7$S/m and$1.1 \cdot 10^7$S/m. Hence, it is clear that after the back-side etching, gold conductivity has deteriorated significantly. This adds to the uncertainty of $\tan\delta$ estimations from section 4.1 because it shows that as low conductivity values as 10^7S/m are possible.

Furthermore, DC conductivity of GaN was measured after all processing steps using test structures similar to the ones for gold conductivity measurements. Measured conductivity was about $4 \cdot 10^{-3}$ S/m and $1.5 \cdot 10^{-3}$ S/m for two test structures. $\tan\delta$ for a material can be expressed as

$$\tan\delta = \frac{\sigma + 2\pi f \epsilon_d''}{2\pi f \epsilon_d'}, \quad [40] \tag{4.1}$$

where f is the frequency, ϵ_d'' is the imaginary part and ϵ_d' is the real part of the complex permittivity. GaN conductivity would give $\tan\delta = 10^{-5}$ and $\tan\delta = 2.7 \cdot 10^{-5}$ if no dielectric loss was present. For GaN material losses, dielectric loss must therefore be the dominant loss contribution.

To account for additional losses in waveguide transitions used, the transitions from WR2.2 and WR3.4 to circular waveguide and WM760 were measured back-to-back. This is described for the circular waveguide transitions in figure 3.38. The insertion loss of WR2.2 or WR3.4 to circular waveguide transitions measured back-to-back are shown in figure 4.11. The insertion loss of the single transition is then assumed to be about half of that of two transitions back-to-back which is around 0.35 dB. The transition from WR2.2 or WR3.4 to WM760 measured back-to-back is shown in figure 4.12 and for a single transition this equals about 0.2 dB. For the WR2.2 band, insertion loss is somewhat higher in both figure 4.11 and 4.12.

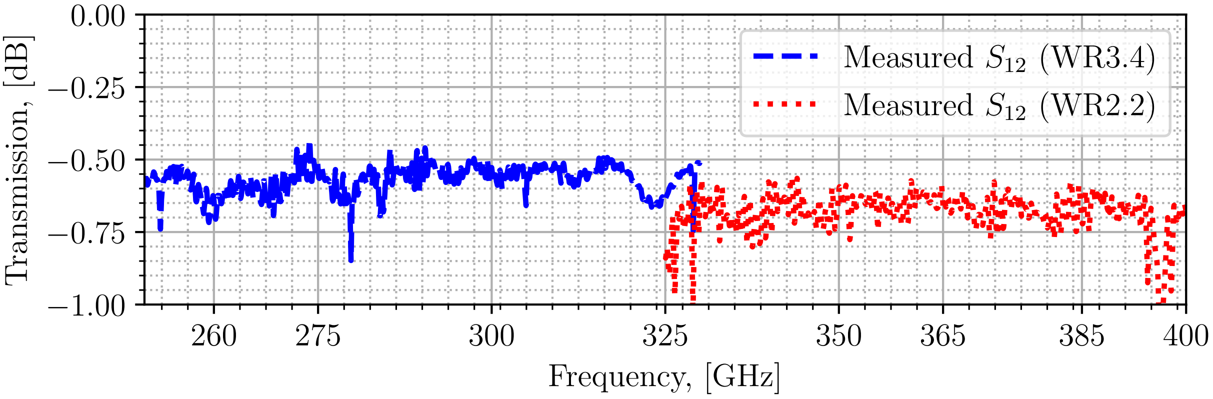

Figure 4.11: Measured insertion loss of back-to-back measurements of the rectangular to circular transition. The transition from WR2.2 or WR3.4 to WM760 is also included as illustrated in figure 3.38. For one transition, approximately half of the insertion loss is expected.

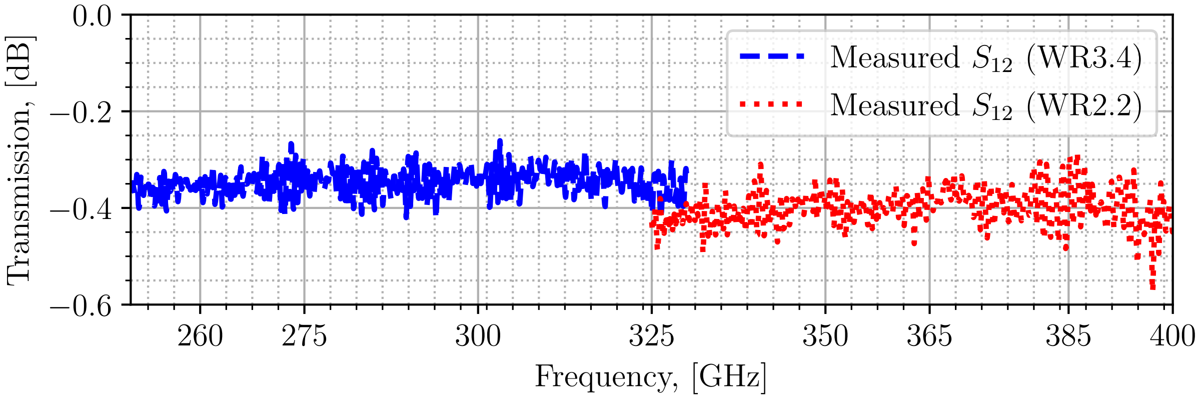

Figure 4.12: Measured insertion loss of back-to-back measurements of the WR2.2 or WR3.4 to WM760 transition. For one transition, approximately half of the insertion loss is expected.

4.3.1 OMT measurement results for chip alternative 2

For the OMT with chip alternative 2 mounted, return loss and insertion loss for polarization 1 are shown in figure 4.16 (measurement setup described in figure 3.36). Estimated insertion losses for the transitions have been subtracted directly from the measured insertion loss.

The measured return loss is higher than 15 dB and insertion loss lower than about 3.5 dB over 270 – 385 GHz in figure 4.13. A more detailed insertion loss plot is shown in figure 4.19. Simulated results with misalignment's are also plotted in figure 4.13 for the best fitted material parameters for GaN and gold presented before in figures 4.1 and 4.2.

The measured return loss and insertion loss for polarization 2 is plotted in figure

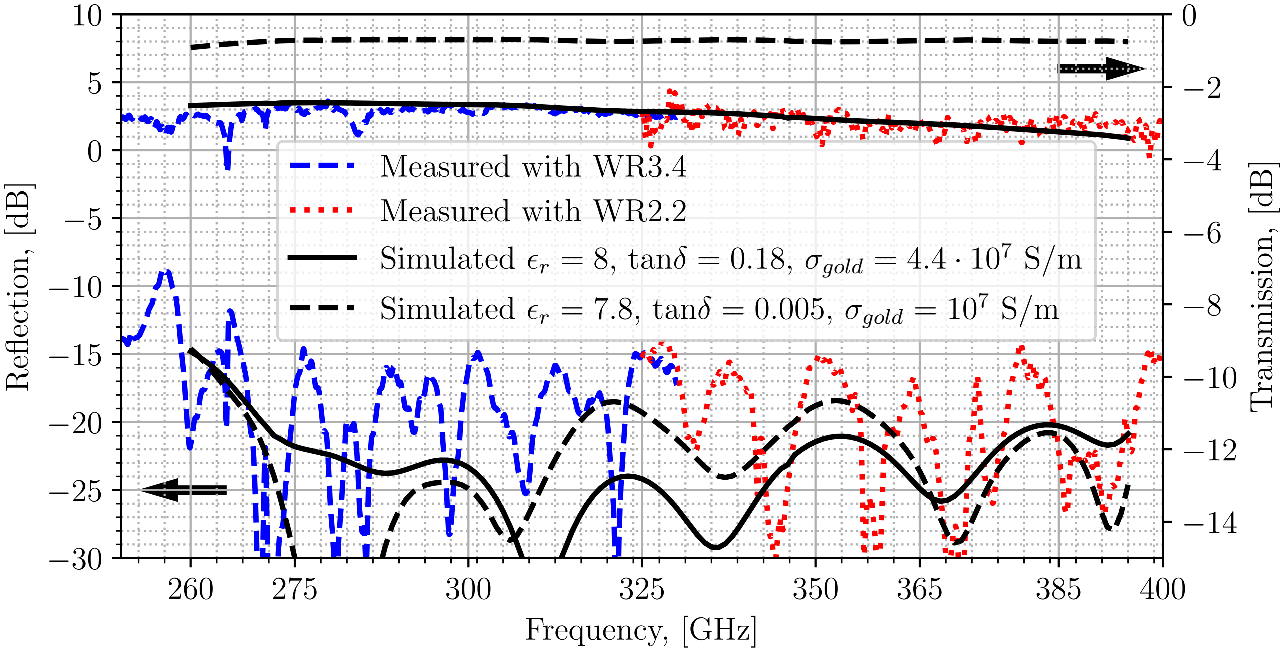

Figure 4.13: Measured S_{11} and S_{12} for polarization 1 in the OMT with chip alternative 2 mounted. In other words, the input return loss (left axis) and insertion loss (right axis) with polarization 1 as co-polarization. The simulated fit is also shown as solid line for comparison.

4.14 and similar to that of polarization 1. The measurement setup was described in figure 3.37 and insertion loss is corrected as for polarization 1. The return loss is above 12 dB and insertion loss below about −3.5 dB over 270 − 385 GHz.

The OMT isolation measured is shown in figure 4.15 using the method described previously in figure 3.41. The isolation is above 30 dB over 270−385 GHz. The cross-polarization, measured and calculated using the method described in section 3.5.2 is also plotted in figure 4.15. For the whole 270 − 385 GHz band, cross-polarization is below −30 dB.

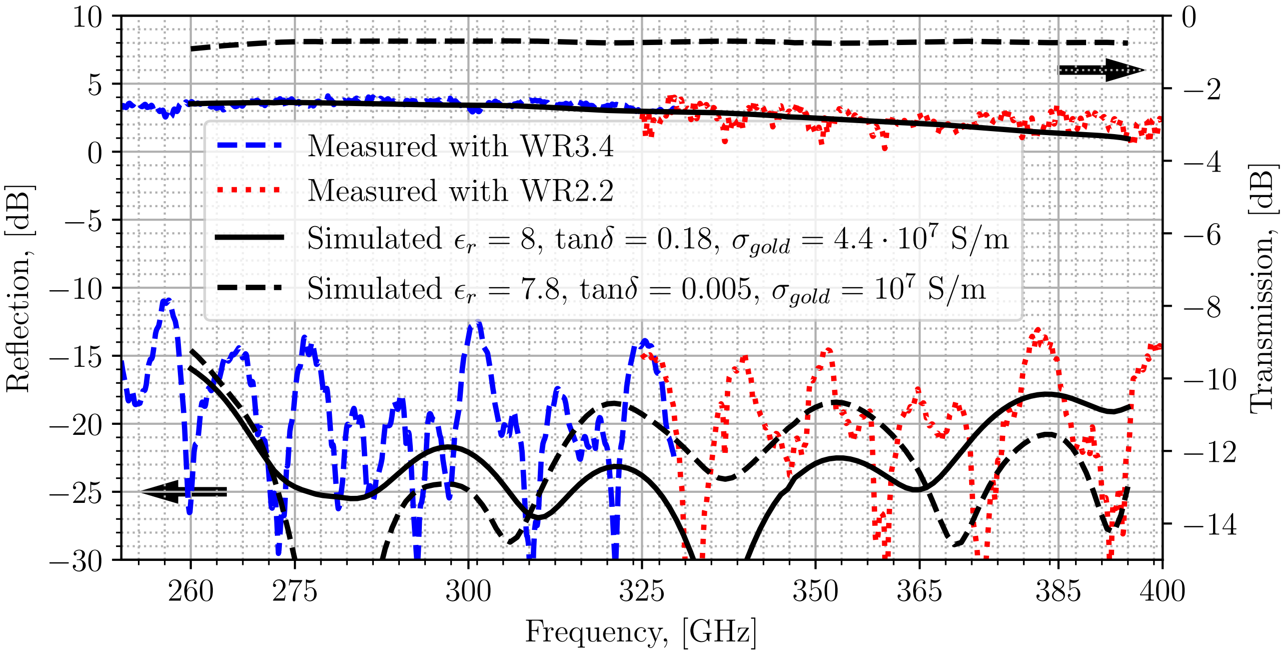

Figure 4.14: Measured S_{11} and S_{12} for polarization 2 in the OMT with chip alternative 2 mounted. In other words, the input return loss (left axis) and insertion loss (right axis) with polarization 2 as co-polarization. The simulated fit is also shown as solid line for comparison.

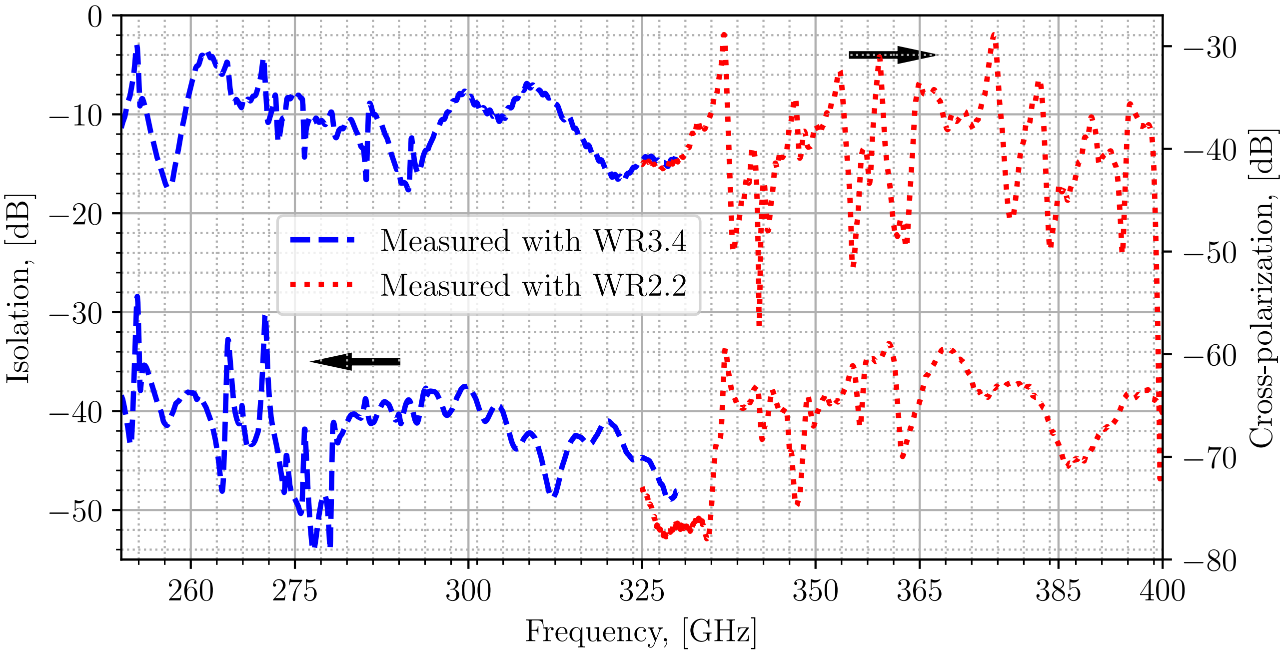

Figure 4.15: Measured isolation (lower curve) and cross-polarization (upper curve) of the OMT with chip alternative 2 mounted. The isolation was measured with the input circular waveguide terminated with a radiating horn. The cross-polarization was calculated using the method described in section 3.5.2.

4.3.2 OMT measurement results for chip alternative 3

For the OMT with chip alternative 3 mounted, return loss and insertion loss for polarization 1 are shown in figure 4.16 (measurement setup described in figure 3.36). The measured insertion losses of the transitions from figures 4.11 and 4.12 are subtracted from measured insertion loss.

The measured return loss is higher than 15 dB and insertion loss lower than about 2.4 dB over 270 − 385 GHz in figure 4.16. A detailed view of the insertion loss is shown in figure 4.20. Simulated results with misalignment's are also plotted in figure 4.16 for the best fitted material parameters for GaN and gold presented before in figures 4.1 and 4.2.

The measured return loss and insertion loss for polarization 2 are plotted in figure 4.17 and similar to that of polarization 1. The measurement setup was described in figure 3.37 and insertion loss is corrected as for polarization 1. The return loss is above 15 dB and insertion loss below about 2.4 dB over 270 − 385 GHz as for polarization 1.

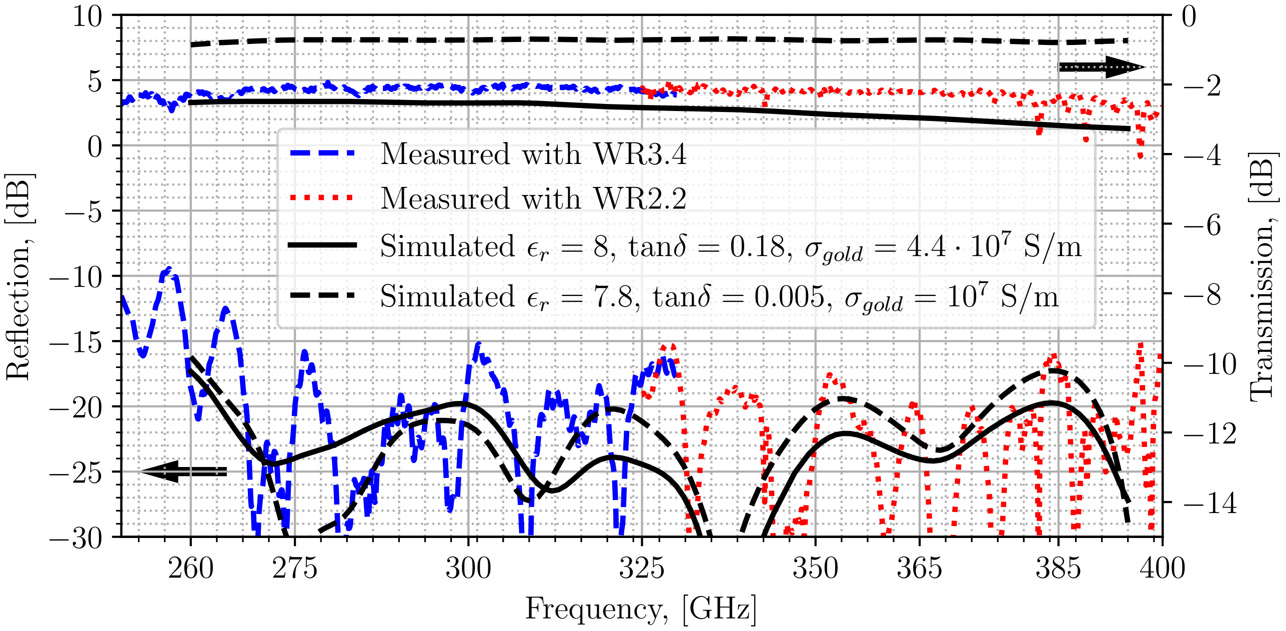

Figure 4.16: Measured S_{11} and S_{12} for polarization 1 in the OMT with chip alternative 3 mounted. In other words, the input return loss (left axis) and insertion loss (right axis) with polarization 1 as co-polarization. The simulated fit is also shown as solid line for comparison.

The OMT isolation measured is shown in figure 4.18 using the method described previously in figure 3.41. The isolation is above 31 dB over 270 − 385 GHz and often above 40 dB. The cross-polarization, measured and calculated using the method described in section 3.5.2 is also plotted in figure 4.18. For the whole 270 − 385 GHz band, cross-polarization is below −26 dB and often below −30 dB. Observe that from 290 GHz to 365 GHz there are standing waves present, which could be effects of trapped modes in the shorted input waveguide.

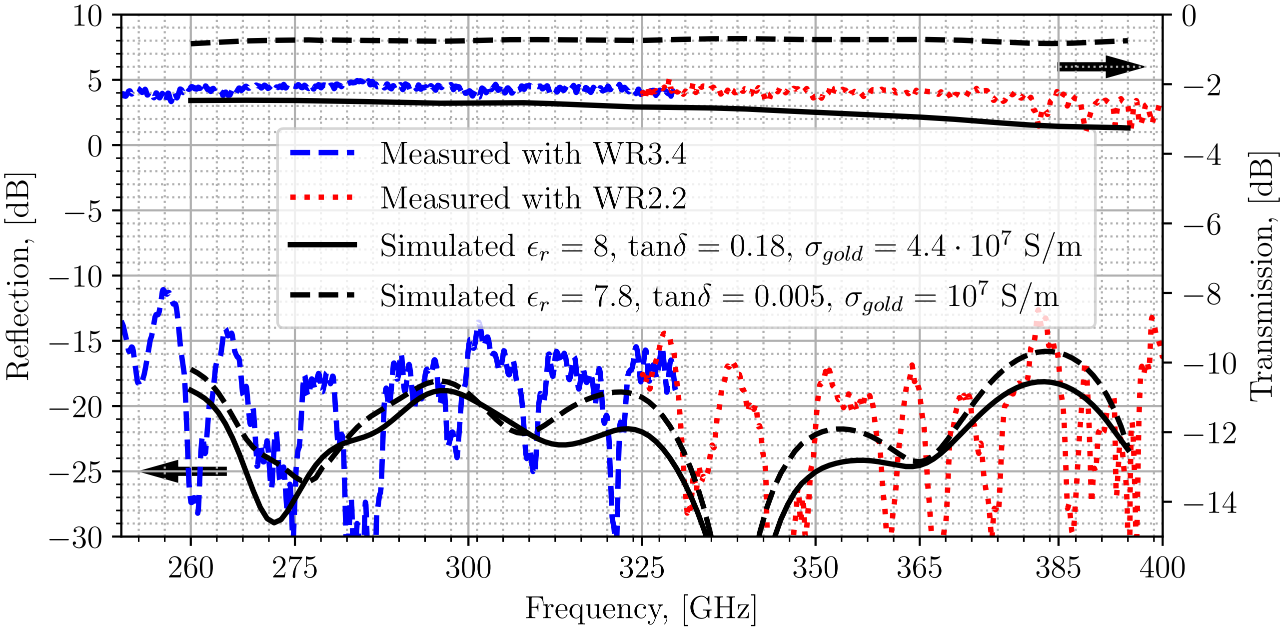

Figure 4.17: Measured S_{11} and S_{12} for polarization 2 in the OMT with chip alternative 3 mounted. In other words, the input return loss (left axis) and insertion loss (right axis) with polarization 2 as co-polarization. The simulated fit is also shown as solid line for comparison.

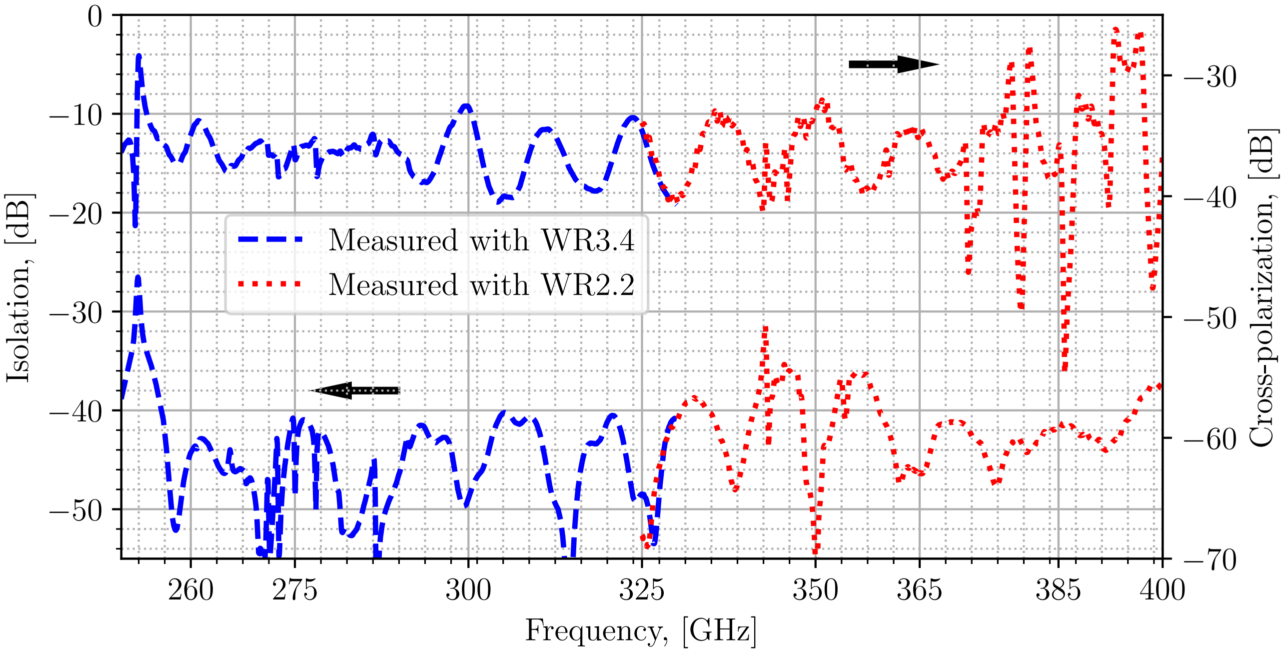

Figure 4.18: Measured isolation (lower curve) and cross-polarization (upper curve) of the OMT with chip alternative 3 mounted. The isolation was measured with the input circular waveguide terminated with a radiating horn. The cross-polarization was calculated using the method described in section 3.5.2.

4.4 Discussion of measured results

4.4.1 Return loss

The two fabricated devices have measured return loss better than 15 dB over the desired band of $270 - 385$ GHz except for a few frequencies for the chip alternative 2 device. The goal was to produce return loss better than 20 dB which is not achieved. For both devices and polarizations, the measured curves have more frequent bumps than the simulated curves. These could be explained by the adaptors on input and output which create additional reflections. If it was possible to measure the devices without adaptors, the measured return loss could be higher. Quite large parts of the band actually present return losses higher than 20 dB which is positive. This is especially the case for the chip alternative 3 device in figure 4.16 and 4.17.

For both polarizations and devices, the return loss behavior is somewhat similar. From the results, the stitching between WR2.2 and WR3.4 is also smooth for both devices and polarizations.

4.4.2 Isolation and cross-polarization

Isolation is more than 30 dB for both devices and cross-polarization below -30 dB. This is good performance compared to the aim of 25 dB and -25 dB. The simulated isolation is below -50 dB and cross-polarization below -45 dB, which is quite different from measured values. This can be explained by the difficulty with estimating these metrics in simulation. As discussed in [43], in theory a fully symmetrical OMT in theory has both isolation and cross-polarization that is zero. Non-symmetrical geometry created by meshing in HFSS is what introduce isolation and cross-polarization to simulations at all. The simulated values are therefore not accurate. It is possible to predict cross-polarization and isolation by introducing some non-symmetrical misalignment into the simulation [43]. This has not been done however, because cross-polarization and isolation already achieve such good values.

Another observation from the device using chip alternative 3 in figure 4.18 are the bumps in cross-polarization 290 GHz to 365 GHz. These could be standing waves in the input circular waveguide because the input is shorted. This would mean that the real cross-polarization level is approximately the mean of the curve in figure 4.18 for that frequency range. In turn this indicate a cross-polarization level of below -36 dB.

4.4.3 Insertion loss

In figure 4.19 a detailed plot of the insertion loss is shown for the device using chip alternative 2. The insertion loss is below about 3 dB over the band of $270 - 330$ GHz and 3.5 dB over the band of $330 - 385$ GHz except for a resonance at 284 GHz. The two bands stitch well at 325 GHz.

Another discrepancy from the desired insertion loss is the difference between polarizations. As seen in figure 4.19, over most of the band the insertion loss for

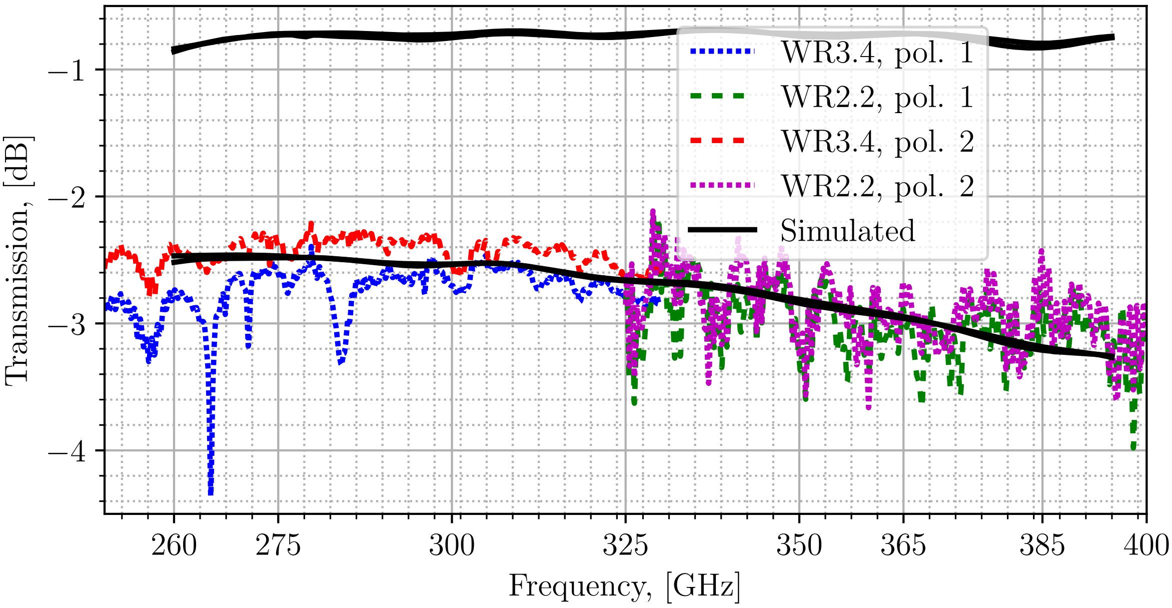

Figure 4.19: Detailed figure of the measured insertion loss for the OMT using chip alternative 2. The upper simulated insertion loss uses GaN material parameters of $\tan\delta = 0.005$, $\sigma_{gold} = 10^7$S/m and $\epsilon_r = 7.8$ as fitted in figure 4.2. The lower simulated insertion loss uses $\tan\delta = 0.18$, $\sigma_{gold} = 4.4 \cdot 10^7$S/m and $\epsilon_r = 8$.

polarization 1 is 0.2 dB higher and have two resonances at 265 GHz and 284 GHz. In the tolerance analysis of chip displacement, resonances were observed. However, the simulations presented in figure 4.19 include the observed misalignment's of the chips which would make this explanation less likely. Another possible explanation could be the adapter from WM750 to circular waveguide. During measurements of the transition in back-to-back configuration, a resonance was observed at the same frequency visible in figure 4.11. By keeping the same alignment pins, unscrewing the device and re-fastening the screws again the resonance could be removed from the back-to-back measurements of the transition. In the case of measurement of the orthomode transducer, a small rotational misalignment at the flange could possibly create such a resonance as observed.

A third observation from the measured device with chip alternative 2 is the higher insertion loss compared to simulations. In figure 4.19 the measured insertion loss is similar to the simulated insertion loss with $\tan\delta = 0.18$. As described earlier however, the ring resonator measurements could not provide an accurate value for $\tan\delta$ and σ_{gold}. The gold conductivity was also measured for the OMT GaN sample to be around 10^7S/m, which suggests that the losses presented in the measured OMT are caused by $\tan\delta$. The other simulated result in figure 4.19 is for material parameters fitted to the ring measurements but with $\sigma_{gold} = 10^7$S/m which fits the measured conductivity for the OMT. The simulated insertion loss for these material parameters however is substantially lower than the measured in figure 4.19. Other possible reasons to the higher insertion loss could be waveguide losses not accounted for in simulations, imperfect contact between blocks and the glue material which

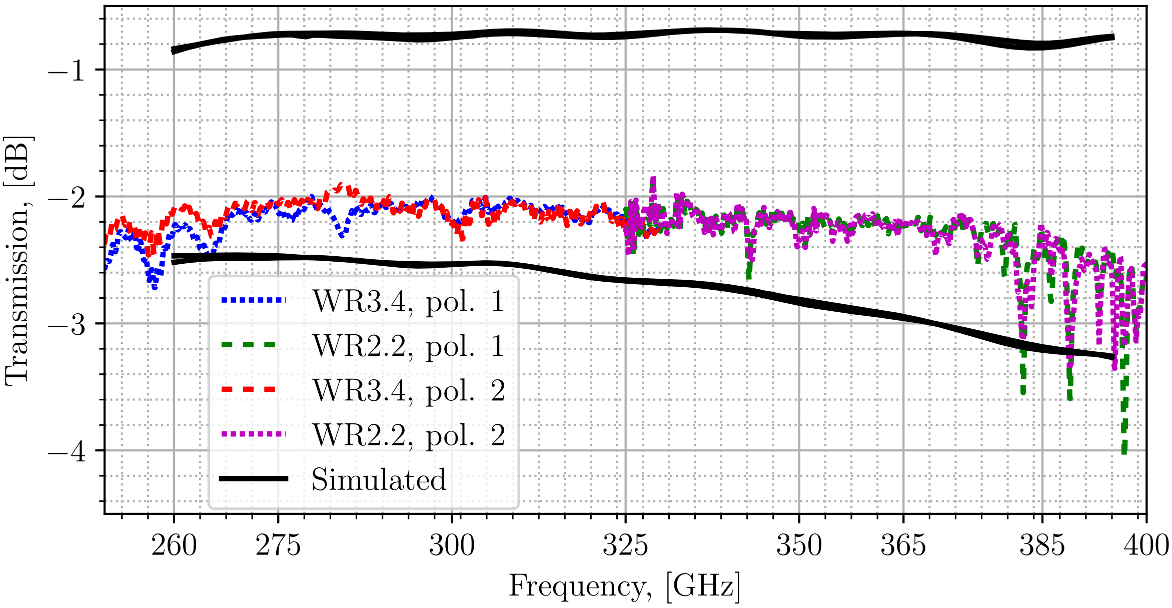

Figure 4.20: Detailed figure of the measured insertion loss for the OMT using chip alternative 3. The upper simulated insertion loss uses GaN material parameters of $\tan\delta = 0.005$, $\sigma_{gold} = 10^7$S/m and $\epsilon_r = 7.8$ as fitted in figure 4.2. The lower simulated insertion loss uses $\tan\delta = 0.18$, $\sigma_{gold} = 4.4 \cdot 10^7$S/m and $\epsilon_r = 8$.

has not been characterized for example.

To further investigate the difference between simulations and measurements the insertion loss for the device using chip alternative 3 is plotted in figure 4.20. In contrast to the other OMT, this device has a very similar behavior for both polarizations. An exception is the resonance at 284 GHz, similar to the one present in figure 4.19 and previously discussed as a possible effect of misalignment of the chip or the adaptor.

The insertion loss of the device using chip alternative 3 is less than about 2.2 dB over 270 − 325 GHz and 2.5 dB over 325 − 380 GHz. This is between the two simulated insertion losses for the two alternative fits to ring resonator measurements. Waveguide losses of adaptors have been taken into account as described earlier. The OMT block waveguide losses have only been simulated in HFSS without any surface roughness model and with bulk copper conductivity of 5.8 S/m. Simulated waveguide loss for both the WM760 and circular waveguide in the model simulated were about 0.1 dB/cm. The waveguide losses in similar waveguides have previously been measured to be about 0.5 dB/cm for 385−500 GHz [76] and 0.15 dB for 150−220 GHz [58]. For each polarization there is about 1.5 cm of additional waveguide (both circular and rectangular) inside the block apart from the OMT itself. This would equate to somewhere between 0.1 − 0.6 dB of additional loss. For the chip alternative 3 device this would make the measured insertion loss between the two alternative material parameter value simulations.

In conclusion of the measured insertion losses, they are higher than what was the goal initially. From the analysis follows however that the most probable cause of the additional losses compared to simulation are material losses in the GaN substrate, which by measurement of GaN conductivity, can be attributed to dielectric loss. As the device would, in a radio astronomy receiver, be cooled to about 4 K, dielectric losses could be lower during usage. For other similar materials such as silicon, this is the case [77]. Also waveguide losses could be lower according to [78].

5

Conclusion

In this thesis different design alternatives were investigated, a novel orthomode transducer designed, manufactured and characterized. The design is compact, wideband and scale-able to higher frequencies. The fabricated devices prove that good performance is possible. In simulation the design proved to achieve return loss of 20 dB or higher and insertion loss of 1 dB or less depending on assumptions of material parameters.

The two working orthomode transducers with acceptable performance has been produced as proof of concept in the frequency band of $270-385$ GHz. Isolation between outputs have been shown to be at least 40 dB for most of the band and cross-polarization below -35 dB for most of the band. These are values well below the desired isolation and cross-polarization of 25 dB and -25 dB. The return loss results prove that it is probably possible to reach a return loss of 20 dB over the desired band. The measured return loss is above 15 dB for the whole band and above 20 dB for large parts of the band which is acceptable as proof of concept.

Insertion loss was concluded to be 2.4 dB or less for one produced device, significantly more than the aim of 0.5 dB. The unexpected additional losses were seen to largely depend on material losses of the substrate used and deterioration of metal conductivity during micro-fabrication processes. The substrate material of gallium nitride has proven to be lossy at room temperature measurements which is also a new finding. To achieve lower insertion loss, other substrate materials could be considered, such as Si, initially investigated in this work. Furthermore, in other literature, losses have for similar materials been seen to decrease considerably when cooled to cryogenic temperatures [77]. Together with the effect of lower waveguide losses at cryogenic temperature [78], the device could prove to have considerably lower insertion loss at these temperatures.

The symmetrical layout of the novel orthomode transducer has been shown to provide similar performance for both polarizations. This is important for polarization sensitive radio astronomy observations where the correlation and relationship between polarization components need to be accurately observed.

Lastly, the design utilizes the higher accuracy of micro-fabrication compared to CNC milling as was one of the goals of this thesis. Scale-ability of the design could be evaluated through the fact that the smallest mill diameter used was 150 µm. By using mill size of 60 µm this could in theory enable scaling to about 1 THz.

Bibliography

[1] *Keysight ads*, `https://www.keysight.com/us/en/products/software/pathwave-design-software/pathwave-advanced-design-system.html`, Accessed: 2023-04-25.

[2] *Ansys hfss*, `https://www.ansys.com/products/electronics/ansys-hfss`, Accessed: 2023-04-17.

[3] ALMA (ESO/NAOJ/NRAO). “Origins.” (), [Online]. Available: `https://almaobservatory.org/en/about-alma/origins/` (visited on 05/18/2023).

[4] R. Güsten, L. Nyman, P. Schilke, K. Menten, C. Cesarsky, and R. Booth, “The atacama pathfinder experiment (apex)–a new submillimeter facility for southern skies–,” *Astronomy & Astrophysics*, vol. 454, no. 2, pp. L13–L16, 2006.

[5] P. T. Ho, J. M. Moran, and K. Y. Lo, “The submillimeter array,” *The Astrophysical Journal*, vol. 616, no. 1, p. L1, 2004.

[6] T. Hashimoto, N. Laporte, K. Mawatari, *et al.*, “The onset of star formation 250 million years after the big bang,” *Nature*, vol. 557, no. 7705, pp. 392–395, 2018.

[7] A. Hacar, M. Tafalla, J. Forbrich, *et al.*, “An alma study of the orion integral filament-i. evidence for narrow fibers in a massive cloud,” *Astronomy & Astrophysics*, vol. 610, A77, 2018.

[8] C. Brogan, L. Pérez, T. Hunter, *et al.*, “The 2014 alma long baseline campaign: First results from high angular resolution observations toward the hl tau region,” *The Astrophysical journal letters*, vol. 808, no. 1, p. L3, 2015.

[9] ALMA (ESO/NAOJ/NRAO). “Discoveries.” (), [Online]. Available: `https://almaobservatory.org/en/about-alma/how-alma-works/early-discoveries/` (visited on 05/18/2023).

[10] K. Akiyama, A. Alberdi, W. Alef, *et al.*, “First sagittarius a* event horizon telescope results. i. the shadow of the supermassive black hole in the center of the milky way,” *The Astrophysical Journal Letters*, vol. 930, no. 2, p. L12, 2022.

[11] T. G. Pannuti, “Introduction: Why make astronomical observations at radio frequencies?” *The Physical Processes and Observing Techniques of Radio Astronomy: An Introduction*, pp. 1–16, 2020.

[12] B. M. Gaensler, M. Haverkorn, L. Staveley-Smith, *et al.*, “The magnetic field of the large magellanic cloud revealed through faraday rotation,” *Science*, vol. 307, no. 5715, pp. 1610–1612, 2005.

[13] W. Vlemmings, T. Khouri, I. Marti-Vidal, *et al.*, "Magnetically aligned dust and sio maser polarisation in the envelope of the red supergiant vy canis majoris," *Astronomy & Astrophysics*, vol. 603, A92, 2017.

[14] T. L. Wilson, K. Rohlfs, and S. Hüttemeister, *Tools of radio astronomy.* Springer, 2009, vol. 5, pp. 82–83.

[15] S. Mahieu, D. Maier, B. Lazareff, *et al.*, "The alma band-7 cartridge," *IEEE Transactions on Terahertz Science and Technology*, vol. 2, no. 1, pp. 29–39, 2011.

[16] A. Baryshev, F. Mena, J. Adema, *et al.*, "Alma band 9 cartridge," *Proc. 19th. ISSTT*, pp. 258–262, 2008.

[17] A. Gonzalez, Y. Uzawa, Y. Fujii, and K. Kaneko, "Alma band 10 tertiary optics," *Infrared Physics & Technology*, vol. 54, no. 6, pp. 488–496, 2011.

[18] Y. Sekimoto, Y. Iizuka, N. Satou, *et al.*, "Development of alma band 8 (385-500 ghz) cartridge," in *Proc. 19th Int. Symp. Space Terahertz Technol.*, 2008, pp. 253–257.

[19] G. Ediss, M. Carter, J. Cheng, *et al.*, "Alma band 6 prototype cartridge: Design and performance," in *Proc. 15th Intl. Symp. Space Terahertz Tech*, 2004, pp. 181–188.

[20] B. Billade, O. Nystrom, D. Meledin, *et al.*, "Performance of the first alma band 5 production cartridge," *IEEE Transactions on Terahertz Science and Technology*, vol. 2, no. 2, pp. 208–214, 2012.

[21] S. Asayama, S. Kawashima, H. Iwashita, *et al.*, "Design and development of alma band 4 cartridge receiver," in *Proc. 19th Intl. Symp. Space Terahertz Tech*, 2008, pp. 244–249.

[22] S. Claude, P. Dindo, D. Erickson, *et al.*, "The band 3 receiver (84-116 ghz) for alma," in *2005 Joint 30th International Conference on Infrared and Millimeter Waves and 13th International Conference on Terahertz Electronics*, IEEE, vol. 2, 2005, pp. 407–408.

[23] S. Asayama, G. H. Tan, K. Sini, *et al.*, "Report of the alma front-end & digitizer requirements upgrade working group," ALMA Report, 2020, ALMA-05.00.00.00-0048-A-REP.

[24] G. Narayanan and N. R. Erickson, "Design and performance of a novel full-waveguide band orthomode transducer," in *13th Symposium On Space THz Technology, Cambridge, MA*, 2002.

[25] A. Gonzalez and S. Asayama, "Double-ridged waveguide orthomode transducer (omt) for the 67–116-ghz band," *Journal of Infrared, Millimeter, and Terahertz Waves*, vol. 39, pp. 723–737, 2018.

[26] A. Gonzalez and K. Kaneko, "High-performance wideband double-ridged waveguide omt for the 275–500 ghz band," *IEEE Transactions on Terahertz Science and Technology*, vol. 11, no. 3, pp. 345–350, 2021.

[27] M. Kamikura, M. Naruse, S. Asayama, N. Satou, W. Shan, and Y. Sekimoto, "Development of a submillimeter double-ridged waveguide ortho-mode transducer (omt) for the 385–500 ghz band," *Journal of Infrared, Millimeter, and Terahertz Waves*, vol. 31, pp. 697–707, 2010.

[28] D. Henke and S. Claude, "Design of a 70–116 ghz w-band turnstile omt," in *2014 44th European Microwave Conference*, IEEE, 2014, pp. 456–459.

[29] A. Navarrini, R. L. Plambeck, and D. Chow, “A turnstile junction waveguide orthomode transducer for the 1 mm band,” in *Proceedings of the 16th International Symposium on Space Terahertz Technology*, 2005, pp. 02–04.

[30] A. Gomez-Torrent, U. Shah, and J. Oberhammer, “Wideband 220–330 ghz turnstile omt enabled by silicon micromachining,” in *2018 IEEE/MTT-S International Microwave Symposium-IMS*, IEEE, 2018, pp. 1511–1514.

[31] A. Navarrini and R. Nesti, “Symmetric reverse-coupling waveguide orthomode transducer for the 3-mm band,” *IEEE Transactions on microwave theory and techniques*, vol. 57, no. 1, pp. 80–88, 2008.

[32] C. Groppi, A. Navarrini, and G. Chattopadhyay, “A waveguide orthomode transducer for 385-500 ghz,” in *Millimeter, Submillimeter, and Far-Infrared Detectors and Instrumentation for Astronomy V*, SPIE, vol. 7741, 2010, pp. 699–709.

[33] S. Sirsi, *A Novel Ortho-Mode Transducer for the 750-1150 GHz Band.* Arizona State University, 2014.

[34] C. Groppi, C. D. d’Aubigny, A. W. Lichtenberger, C. M. Lyons, and C. K. Walker, “Broadband finline ortho-mode transducer for the 750-1150 ghz band,” in *Proceedings of the 16th. International Symposium on Space Terahertz Technology*, 2005, pp. 513–518.

[35] W. Shan, S. Ezaki, J. Liu, S. Asayama, T. Noguchi, and S. Iguchi, “Planar superconductor-insulator-superconductor mixer array receivers for wide field of view astronomical observation,” in *Millimeter, Submillimeter, and Far-Infrared Detectors and Instrumentation for Astronomy IX*, SPIE, vol. 10708, 2018, pp. 125–139.

[36] J. McMahon, J. Appel, J. Austermann, *et al.*, “Planar orthomode transducers for feedhorn-coupled tes polarimeters,” in *AIP Conference Proceedings*, American Institute of Physics, vol. 1185, 2009, pp. 490–493.

[37] P. Mauskopf, J. Zhang, P. Ade, S. Withington, and P. Grime, “Clover polarimetric detector-a novel design of an ortho-mode transducer at 150 and 225 ghz,” in *2008 33rd International Conference on Infrared, Millimeter and Terahertz Waves*, IEEE, 2008, pp. 1–2.

[38] C.-T. Li, K.-Y. Liu, W.-C. Lu, *et al.*, “Development of 460 ghz and dual polarization sis mixers for the submillimeter array,” *IEEE transactions on applied superconductivity*, vol. 21, no. 3, pp. 654–658, 2011.

[39] D. M. Pozar, *Microwave engineering.* John wiley & sons, 2011.

[40] S. Orfanidis, “Electromagnetic waves and antennas (sophocles j. orfanidis, 2016),” *URL https://books. google. com. au/books*,

[41] D. Cheng, *Field and Wave Electromagnetics* (Addison-Wesley series in electrical engineering). Addison-Wesley, 1989, ISBN: 9780201528206. [Online]. Available: `https://books.google.se/books?id=6xmoMgEACAAJ`.

[42] T. L. Wilson, K. Rohlfs, and S. Hüttemeister, *Tools of radio astronomy.* Springer, 2009, vol. 5.

[43] A. Navarrini and R. Nesti, “Characterization techniques of millimeter-wave orthomode transducers (omts),” *Electronics*, vol. 10, no. 15, p. 1844, 2021.

[44] A. M. Bøifot, “Classification of ortho-mode transducers,” *European Transactions on Telecommunications*, vol. 2, no. 5, pp. 503–510, 1991.

[45] G. Chattopadhyay and J. E. Carlstrom, "Finline ortho-mode transducer for millimeter waves," *IEEE microwave and guided wave letters*, vol. 9, no. 9, pp. 339–341, 1999.

[46] G. Engargiola and A. Navarrini, "Orthomode transducer with waveguide ports and balanced coaxial probes," in *Proc. 16th. International Symposium on Space Terahertz Technology*, 2005, pp. 334–337.

[47] A. Hammar, P. Sobis, V. Drakinskiy, H. Z. Ternehäll, J. Stake, and A. Emrich, "A 600 ghz orthomode transducer based on a waveguide integrated wire grid polarizer," in *TWENTY-THIRD INTERNATIONAL SYMPOSIUM ON SPACE TERAHERTZ TECHNOLOGY (ISSTT2012)*, 2012.

[48] A. Dunning, S. Srikanth, and A. Kerr, "A simple orthomode transducer for centimeter to submillimeter wavelengths," in *Proc. 20th Int. Symp. Space Terahertz Technol.*, 2009, pp. 191–193.

[49] C. A. Leal-Sevillano, K. B. Cooper, E. Decrossas, *et al.*, "Compact duplexing for a 680-ghz radar using a waveguide orthomode transducer," *IEEE Transactions on Microwave Theory and Techniques*, vol. 62, no. 11, pp. 2833–2842, 2014.

[50] G. Chattopadhyay, B. Philhour, J. E. Carlstrom, S. Church, A. Lange, and J. Zmuidzinas, "A 96-ghz ortho-mode transducer for the polatron," *IEEE microwave and guided wave letters*, vol. 8, no. 12, pp. 421–423, 1998.

[51] W. Steffe, "A novel compact omj for ku band intelsat applications," in *IEEE Antennas and Propagation Society International Symposium. 1995 Digest*, IEEE, vol. 1, 1995, pp. 152–155.

[52] R. E. Collin, *Foundations for microwave engineering.* John Wiley & Sons, 2007.

[53] C. López, V. Desmaris, D. Meledin, A. Pavolotsky, and V. Belitsky, "Waveguide-to-substrate transition based on unilateral substrateless finline structure: Design, fabrication, and characterization," *IEEE Transactions on Terahertz Science and Technology*, vol. 10, no. 6, pp. 668–676, 2020.

[54] B.-K. Tan and G. Yassin, "A slotline dc block for microwave, millimeter, and submillimeter circuits," *IEEE Microwave and Wireless Components Letters*, vol. 29, no. 9, pp. 583–585, 2019.

[55] J. Kooi, G. Chattopadhyay, S. Withington, *et al.*, "A full-height waveguide to thin-film microstrip transition with exceptional rf bandwidth and coupling efficiency," *International Journal of Infrared and Millimeter Waves*, vol. 24, pp. 261–284, 2003.

[56] A. Kerr, "Elements for e-plane split-block waveguide circuits," *National Radio Astronomy Observatory, ALMA Memo*, vol. 381, p. 5, 2001.

[57] A. Kerr and N. Horner, "A broadband in-phase waveguide power divider/combiner," *ALMA Memo*, vol. 10, 2000.

[58] A. Gouda, C. D. López, V. Desmaris, D. Meledin, A. B. Pavolotsky, and V. Belitsky, "Millimeter-wave wideband waveguide power divider with improved isolation between output ports," *IEEE Transactions on Terahertz Science and Technology*, vol. 11, no. 4, pp. 408–416, 2021.

[59] J. W. Kooi, *Advanced receivers for submillimeter and far infrared astronomy.* Rijkuniversiteit Groningen, 2008.

[60] V. Vassilev and V. Belitsky, “Design of sideband separation sis mixer for 3 mm band,” in *Proceedings of the 12th International Symposium on Space Terahertz Technology*, 2001.

[61] J. Tsao, S. Chowdhury, M. Hollis, *et al.*, “Ultrawide-bandgap semiconductors: Research opportunities and challenges,” *Advanced Electronic Materials*, vol. 4, no. 1, p. 1 600 501, 2018.

[62] F. Roccaforte, P. Fiorenza, G. Greco, *et al.*, “Challenges for energy efficient wide band gap semiconductor power devices,” *physica status solidi (a)*, vol. 211, no. 9, pp. 2063–2071, 2014.

[63] S. V. Koshevaya, V. V. Grimalsky, A. Garcia-B, and F. Diaz-A, “Amplification and nonlinear interaction of space charge waves of microwave band in heterogeneous gallium nitride films,” *Radioelectronics and Communications Systems*, vol. 55, no. 7, pp. 289–298, 2012.

[64] S. Krause, V. Desmaris, A. Pavolotsky, D. Meledin, and V. Belitsky, “Suspended gan beams and membranes on si as a platform for waveguide-based thz applications,” *Journal of Micromechanics and Microengineering*, vol. 28, no. 10, p. 105 007, 2018.

[65] V. C. Agulto, T. Iwamoto, K. Toya, *et al.*, “Terahertz time-domain spectroscopy of wide-bandgap semiconductors gan and β-ga2o3,” in *Twelfth International Conference on Information Optics and Photonics*, SPIE, vol. 12057, 2021, pp. 1066–1073.

[66] A. Barker Jr and M. Ilegems, “Infrared lattice vibrations and free-electron dispersion in gan,” *Physical Review B*, vol. 7, no. 2, p. 743, 1973.

[67] A. Note, “1217–1. basics of measuring the dielectric properties of materials,” *Hewlett-Packard Company: Palo Alto, CA*, 1992.

[68] J. Bonache, I. Gil, J. Garcia-Garcia, and F. Martin, “Complementary split rings resonators (csrrs): Towards the miniaturization of microwave device design,” *Journal of computational electronics*, vol. 5, pp. 193–197, 2006.

[69] *Vna extender - vdi model: Wr3.4-vnax*, `https://vadiodes.com/en/wr3-4vnax`, Accessed: 2023-04-28.

[70] *Autodesk inventor*, `https://www.autodesk.com/products/inventor`, Accessed: 2023-05-17.

[71] “Ieee standard for rectangular metallic waveguides and their interfaces for frequencies of 110 ghz and above - part 1: Frequency bands and waveguide dimensions,” IEEE, 3 Park Avenue, New York, NY 10016-5997, USA, Standard, 2012.

[72] *N5242b pna-x microwave network analyzer*, `https://www.keysight.com/us/en/product/N5242B/pna-x-microwave-network-analyzer-900-hz-10-mhz-26-5-ghz.html`, Accessed: 2023-05-17.

[73] *Vna extender - vdi model: Wm-570 (wr2.2) vnax*, `https://vadiodes.com/en/wr2-2vnax`, Accessed: 2023-05-24.

[74] Zygo, *Zegage™ pro*, Webpage, 2023. [Online]. Available: `https://www.zygo.com/products/metrology-systems/3d-optical-profilers/zegage-pro`.

[75] G. Reeves and H. Harrison, “Obtaining the specific contact resistance from transmission line model measurements,” *IEEE Electron Device Letters*, vol. 3, no. 5, pp. 111–113, 1982. DOI: `10.1109/EDL.1982.25502`.

[76] V. Desmaris, D. Meledin, D. Dochev, A. Pavolotsky, and V. Belitsky, "Terahertz components packaging using integrated waveguide technology," in *2011 IEEE MTT-S International Microwave Workshop Series on Millimeter Wave Integration Technologies*, 2011, pp. 81–84. DOI: `10.1109/IMWS3.2011.6061893`.

[77] J. Krupka, J. Breeze, A. Centeno, N. Alford, T. Claussen, and L. Jensen, "Measurements of permittivity, dielectric loss tangent, and resistivity of float-zone silicon at microwave frequencies," *IEEE Transactions on microwave theory and techniques*, vol. 54, no. 11, pp. 3995–4001, 2006.

[78] R. Finger and A. Kerr, "Microwave loss reduction in cryogenically cooled conductors," *International Journal of Infrared and Millimeter Waves*, vol. 29, pp. 924–932, 2008.

A

Alternative combiner

During design, and alternative combiner was tested. These results and motivation for its use is presented here.

A.1 Investigation of alternative combiner

During initial tolerance analysis it was found that movement of the chip in x and y direction affected return loss and insertion loss largely. This was further investigated by simulating 15 µm misalignment of the chip in only x direction without the combiners as shown in figure 3.15. The scattering parameters extracted from this simulation were imported into *Keysight ADS* which is a program that can simulate the interaction between different components if their scattering parameters are known. An illustration of this is shown in figure A.1 where the OMJ scattering parameters are denoted $\mathbf{S}_{OMT}$ and combiner scattering parameters $\mathbf{S}_{comb}$.

Two different theoretical combiners were then tested in *Keysight ADS* [1] with scattering parameters $\mathbf{S}_{comb} = \mathbf{S}_{-15}$ and $\mathbf{S}_{comb} = \mathbf{S}_{-6}$ being,

$$\mathbf{S}_{-6} = \begin{bmatrix} 0.01 & \sqrt{0.5} & -\sqrt{0.5} \\ \sqrt{0.5} & \sqrt{0.25} & \sqrt{0.25} \\ -\sqrt{0.5} & \sqrt{0.25} & \sqrt{0.25} \end{bmatrix}, \quad \mathbf{S}_{-15} = \begin{bmatrix} 0.01 & \sqrt{0.5} & -\sqrt{0.5} \\ \sqrt{0.5} & \sqrt{0.03} & \sqrt{0.03} \\ -\sqrt{0.5} & \sqrt{0.03} & \sqrt{0.03} \end{bmatrix}. \tag{A.1}$$

This was done to test what a combiner with better isolation between the input ports could affect the overall OMT tolerance to movement of the chip. $\mathbf{S}_{-6}$ has a port isolation and return loss between port 2 and 3 of -6 dB which is approximately what the waveguide Y-junction combiner in figure 3.12 has. This is in accordance with the simulation results presented in figure 3.14. $\mathbf{S}_{-15}$ has port isolation of -15 dB between port 2 and 3 which is close to what the designed combiner in [58] achieve.

The insertion loss simulation results done in ADS is shown in figure A.2. Movement of the chip was only done in y direction by 15 µm which means the expected resonances should be present in polarization 2. For the combiner with isolation of -6 dB the resonances are visible around 300 GHz but for the combiner with isolation of -15 dB no resonances are visible.

Based on the simulations of an alternative combiners with *Keysight ADS* the design from [58] was testes. This particular combiner uses a lossy chip with a probe inserted into the waveguide to improve isolation between port 2 and 3 as shown in figure A.3.

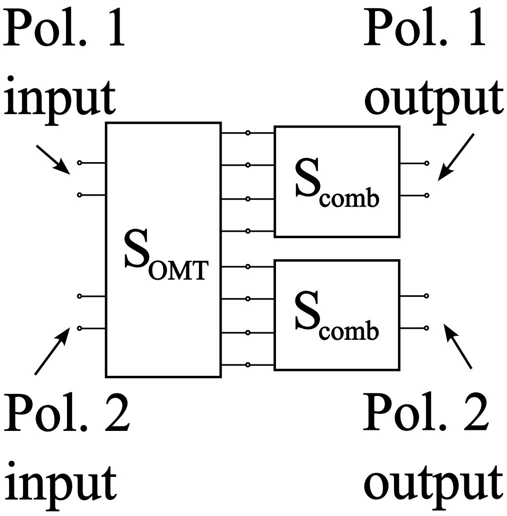

Figure A.1: Illustration of the simulation done in ADS. $\mathbf{S}_{OMT}$ is a 6-port microwave network and $\mathbf{S}_{comb}$ 3-port networks.

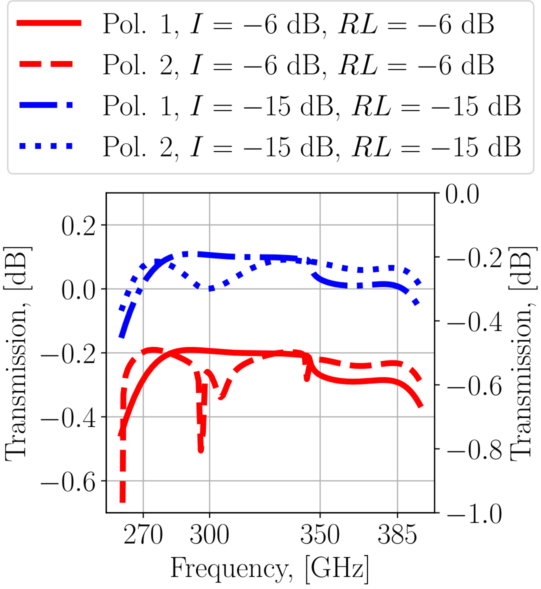

Figure A.2: Simulated transmission in ADS. I is isolation of the combiner simulated and RL input return loss for the two input ports of the combiners. Note the resonances for polarization 2 and $I = -6$ dB around 300 GHz.

A model of the combiner in [58] was made and scaled from 185 GHz to 330 GHz. The waveguide steps at the two branches to port 2 and 3 and the two steps in the waveguide leading to port 1 as shown in figure A.3 were parameterized. The waveguides leading to port 2 and 3 in figure A.3 are different from [58] because they are angled in a Y-shape instead of T-shape. An optimization was run for maximum return loss at port 1 and minimum insertion loss from port 1 to port 2 and 3. The chip was scaled uniformly compared to [58] while the waveguide step dimensions were re-optimized in HFSS [2]. After optimization the combiner was assembled with the OMJ similarly as shown for the other combiner in figure 3.19 and simulated.

The HFSS reflection and transmission simulation results for the alternative combiner are shown in figure A.4. A 15 µm misalignment of the GaN thinfilm was implemented to evaluate if this model was as sensitive. As seen in figure A.4 the return loss was only about 10 dB which means more development would be required to make it fulfill the design specifications. Because of non-sufficient return loss and the simplicity of the firstly designed combiner (figure 3.12) that simpler alternative was used for production.

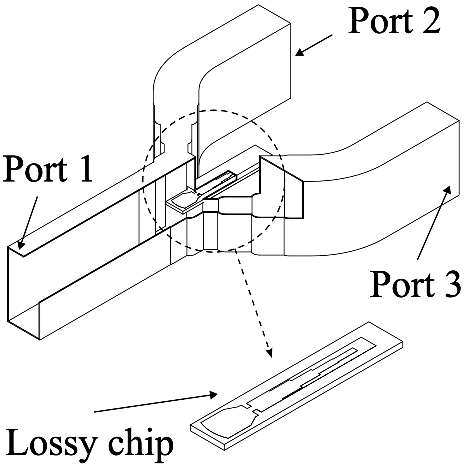

Figure A.3: The optimized Y-shaped combiner with a lossy chip.

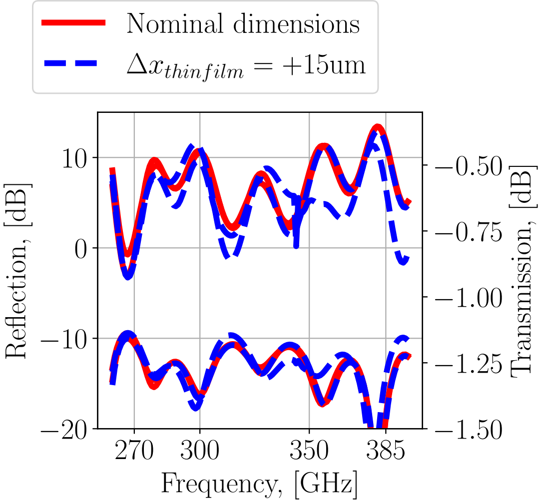

Figure A.4: Tolerance analysis of thin-film chip movement in x direction for a full OMT utilizing the alternative Y-shaped combiner shown in figure A.3.

A.2 Full-wave simulation of alternative combiner

For the other lossy combiner based on [58] simulated reflection coefficients and insertion loss is shown in figure A.5. The reflection coefficient for port 1 worse than for the simple combiner in figure 3.13, however the reflection coefficient for port 2 and 3 is substantially better. The insertion loss is actually similar between the two combiners in the way that maximum insertion loss is below 0.1 dB in the band. Port isolation and transmission from port 1 to 2 and 3 is shown in figure A.6. The port isolation between port 2 and 3 is considerably higher than for the simple combiner and transmission is close to −3 dB similarly to the simple combiner.

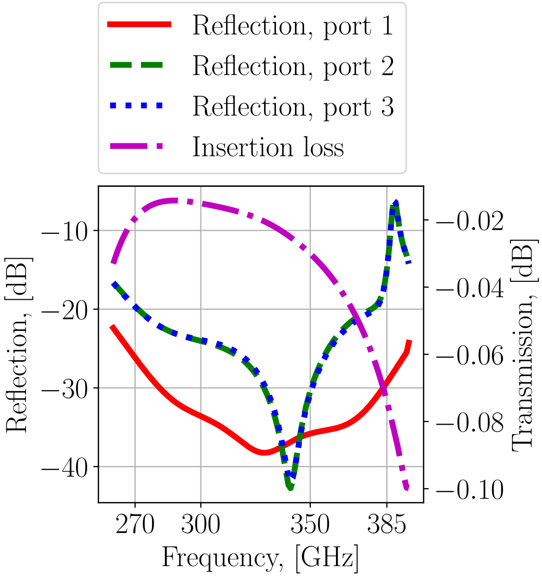

Figure A.5: first figure

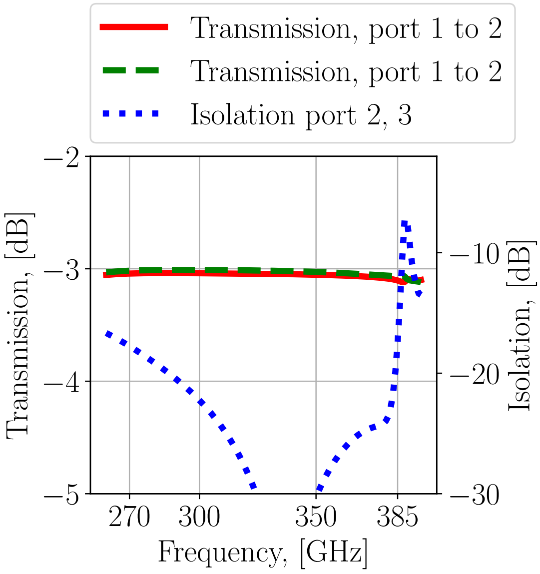

Figure A.6: second figure

B

Dielectric theory

In a simple case permittivity relate the electric field intensity ($\vec{E}$) to the electric flux density ($\vec{D}$) in a material by,

$$\vec{D} = \epsilon\vec{E} \tag{B.1}$$

where ϵ is the permittivity. This equation is one of the constitutive relations used when applying Maxwell's equations to analyse materials. In this relation it is also assumed that the material behaves in a homogeneous and isotropic way.

To model the interaction between material and electromagnetic fields some modelling of the material is necessary. A commonly used model for dielectric materials considers bound electrons with a presence of an electric field. The electric field $E(t)$ will displace the electron in the direction of the electric field and Newtons second law is used to describe this by,

$$m_e\frac{d^2x(t)}{dt^2} = e \cdot E(t) \tag{B.2}$$

where e is the electric charge, m_e is the electric mass and $x(t)$ is the position of the electron in the direction of applied electric field. If a first order restoring force proportional to the electron displacement x with spring constant k is used to model the binding of the electron equation B.2 changes to,

$$m_e\frac{d^2x(t)}{dt^2} = e \cdot E(t) - k \cdot x. \tag{B.3}$$

If also some damping effect is modelled by some friction force proportional to the speed of the electron, equation B.3 can be modified to,

$$m_e\frac{\mathrm{d}^2x(t)}{\mathrm{d}t^2} = e \cdot E(t) - k \cdot x(t) - m_e\gamma\frac{\mathrm{d}x(t)}{\mathrm{d}t}. \tag{B.4}$$

For an applied sinusoidal electric field, described by $E(t) = \Re(E_0e^{j\omega t})$, the differential equation of B.4 can be solved by,

$$x(t) = \Re\left(\frac{eE/m_e}{\omega_0^2 - \omega^2 + j\omega\gamma} \cdot e^{j\omega t}\right). \tag{B.5}$$

Now, remember that the electric flux density D can be written as

$$D = \epsilon_0E + P \tag{B.6}$$

where P is the polarization per unit volume. The individual electrons give rise to a dipole moment of $p = ex$ so by multiplying with the number of dipoles per unit volume N its possible to rewrite B.6 as,

$$\bar{D} = \left(\epsilon_0 + \frac{eE/m_e}{\omega_0^2 - \omega^2 + j\omega\gamma}\right)\bar{E}. \tag{B.7}$$

By comparing equation B.7 to B.1 we can see that ϵ is now complex. This is usually indicated as,

$$\hat{\epsilon}(\omega) = \epsilon'(\omega) - j\epsilon''(\omega) \tag{B.8}$$

where $\epsilon'(\omega)$ is the real permittivity and $\epsilon''(\omega)$ is the imaginary permittivity [40].

Equation B.7 provide a simple model of a material where an electron is displaced in its bound state. Real dielectrics can however be more accurately modelled by several of these harmonic oscillators with different constants for N, e, m_e, ω_0 and γ. This could be expressed by some modification of equation B.7 to have,

$$\hat{\epsilon}(\omega) = \epsilon_0 + \epsilon_0 \sum_i \frac{N_i e_i^2/m_i\epsilon_0}{\omega_i^2 - \omega^2 + j\omega\gamma_i}. \tag{B.9}$$

If $\epsilon' = \Re(\hat{\epsilon}(\omega))$ and $\epsilon'' = \Im(\hat{\epsilon}(\omega))$ were plotted against frequency ω, then resonant structures schematically shown in figure B.1 for atomic effects and electronic effects could be observed.

In figure B.1 two other effects are also shown. In some dielectric materials, for example water, molecules can rotate to form different dipole moments [67]. This effect is called orientation polarization. Figure B.1 highlight the decrease in ϵ' and peak in ϵ'' that these effects could create [67]. At lower frequencies, also ionic interaction affects losses by conduction in some materials [67]. Orientation and ionic polarization are not very important for GaN at these high frequencies and the frequency dependence can mostly be modelled as in equation B.9 [66].

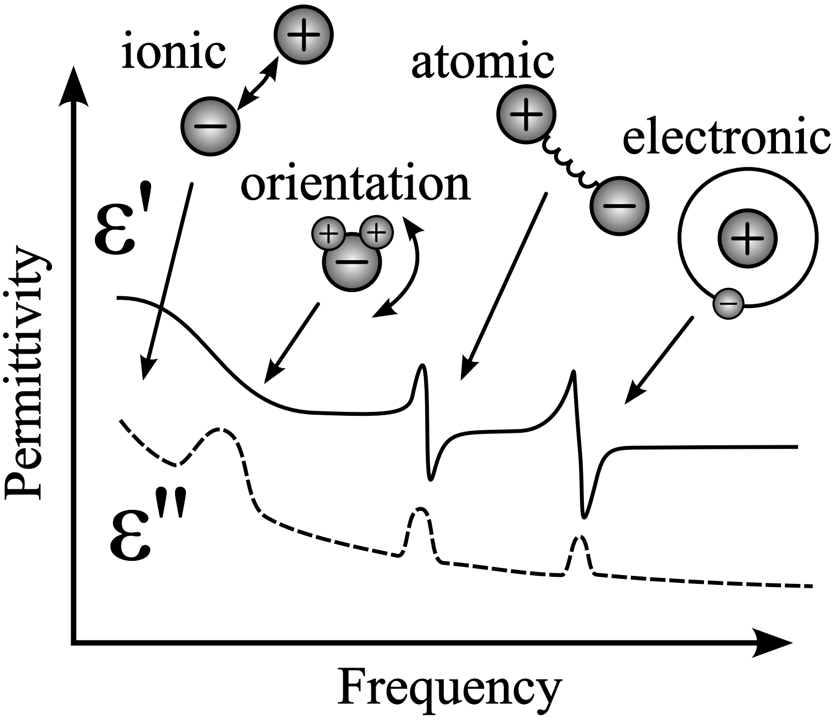

Figure B.1: Illustration of how the real part ($\epsilon' = \Re(\epsilon)$) and imaginary part ($\epsilon'' = -\Im(\epsilon)$) of the complex permittivity are dependent on frequency. The different phenomena are indicated.

DEPARTMENT OF SPACE, EARTH AND ENVIRONMENT
CHALMERS UNIVERSITY OF TECHNOLOGY
Gothenburg, Sweden
www.chalmers.se

CHALMERS
UNIVERSITY OF TECHNOLOGY